Development of a Mode I test rig for quantitative measurements of ice adhesion using tensile stress

María José Grasso

A Thesis
In the Department
of
Mechanical, Industrial and Aerospace Engineering

Presented in Partial Fulfillment of the Requirements
For the Degree of

Master of Applied Science (Mechanical Engineering) at
Concordia University
Montreal, Quebec, Canada

December 2019

CONCORDIA UNIVERSITY

School of Graduate Studies

This is to certify that the thesis prepared

By: María José Grasso

Entitled: Development of a Mode I test rig for quantitative measurements of ice adhesion using tensile stress

and submitted in partial fulfillment of the requirements for the degree of

Master of Applied Science (Mechanical Engineering)

complies with the regulations of the University and meets the accepted standards with respect to originality and quality.

Signed by the final Examining Committee:

_____ Chair
Dr. Hany Gomaa

_____ Examiner
Dr. Lyes Kadem

_____ Examiner
Dr. Fariborz Haghighat

_____ Co-Supervisor
Dr. Ali Dolatabadi

_____ Co-Supervisor
Dr. Elmar Bonaccurso

Approved by _____
Chair of Department or Graduate Program Director

December 17th, 2019 _____
Dr. Amir Asif, Dean, Gina Cody School of Engineering and Computer Science

Abstract

Development of a Mode I test rig for quantitative measurements of ice adhesion using tensile stress

María José Grasso

Every winter in Canada, ice formation affects airplanes, power lines, telecommunications equipment, windmills, ships and rail transport. Icing in aeronautics augment significant human and monetary costs. From the National Transportation Safety Board (NTSB) Accident Database, during a 19-year period 583 accidents and more than 800 fatalities were caused by airframe icing accidents. Ice accumulation on aerostructures causes a variety of issues — loss of lift, increase in drag, jamming of control surfaces or of mechanical parts, damage of engine blades. Thus, aircraft icing affects the safety of flight and increases fuel consumption. Engineers have developed various techniques for anti-\ and de-icing areas for components of an aircraft that are affected. In laboratory settings, these technologies show promising results. However, they are designed and tested under ‘‘ideal’’ conditions and consequently they often underperform in practical applications. Not all of the technologies make it beyond the conceptual phase, which is also due to the fact that the processes of ice accretion and ice adhesion are not fully understood yet.

The purpose of this thesis is to study the available ice adhesion tests in order to select and develop an easy to use and reproducible testing tool for measuring ice adhesion. The Mode I or tensile was chosen because the analysis of the results is well understood, the test is fully controlled and it can be easily reproduced. Test results will simulate real, in-flight icing conditions. Mode I applies tensile loading at the ice-substrate interface. The CRT icing wind tunnel has the capability of investigating the ice adhesion with a bending cantilever test that measures the ice-substrate interfacial strength based on harmonic excitation with a permanent magnet shaker. This proposed study will help researchers and engineers to develop reliable systems by correlating the complementary ice adhesion results obtained from the Mode I and the bending cantilever tests. The intention is to minimize the risk of failures when conducting full-scale or flight testing. The prevention of

ice build-up on aircraft structures or its easy removal will reduce safety hazards, in addition to leading to considerable savings, both financial and environmental. Further advancement in the technology of ice protection systems will contribute to retaining Canada’s position as the leading authority of aerospace, green energy production, and consumer products.

Acknowledgements

I would like to express my sincere gratitude to both of my thesis advisors. Dr. Ali Dolatabadi for his enormous help and for always having his office's door open for when I needed support and help, his optimistic energy, his encouragement and his flexibility. Dr. Elmar Bonaccurso for his enthusiasm, wise guidance and his endless patience. I am extremely grateful to have worked with two of the best professionals in the research and aeronautics field and I am forever grateful to both of them for providing me with great opportunities, from this research project, through an international internship in Munich and to a collaboration with Airbus.

This thesis study would not have been possible without the help and support of various individuals over the last two years. Alexandre Laroche for his much needed support during the experimental phase and during the writing of the thesis. Guy Fortin for sharing his technical experience and knowledge; his suggestions were greatly valuable to my research. I also would like to thank my Airbus colleagues from whom I had the chance to learn so much and that without their dedicated contribution, many research ideas would not have been fully implemented: Vittorio Vercillo, Frank Palm, Christian Helles, Javier Alejandro Mayen Guillen, Tommy Brunzel, Cem Guido Dedeoglu, Bodo Haffner, Remi Blayac and Birgit Vetter. A special thanks to Damir Cheremisov for his endless encouragement and support. Finally, I would also like to acknowledge Dr. David Hammond, Hugo Pervier and Marie Laure Pervier from Cranfield University for sharing their expertise in the icing field.

Foremost, a special mention for Dr. Elisa Campazzi who has been a tremendous mentor for me and from whom I have learnt about critical thinking to overcome challenges. Her advice and encouragement on my start of professional career have been invaluable.

Table of Contents

List of Figures

List of Tables

Abbreviations

ARP	Aerospace Recommended Practice
CA	Contact Angle [°]
CAH	Contact Angle Hysteresis [°]
CAT	Centrifuge Adhesion Test
CRT	Central Research & Technology
ETFE	Ethylene tetrafluoroethylene
FAA	Federal Aviation Administration
FAR	Federal Aviation Regulation
FEP	Fluorinated ethylene propylene
FS BSL	Full Scale, Best Fit Straight Line
HB	Hydrophobic
HL	Hydrophilic
iCORE	icing and Contamination Research facility
ID	Inner Diameter [mm]
IPS	Ice Protection Systems
ISO	International Organization for Standardization
IWT	Icing Wind Tunnel

LIS	Ultra-smooth lubricant-infused porous surfaces
LWC	Liquid Water Content [g/m^3 or cm^3/min]
Ma	Mach number
Mbps	Megabits per seconds
MVD	Median Volumetric Diameter [μm]
N.A.	Neutral axis
NTSB	National Transportation Safety Board
OD	Outer Diameter [mm]
PIV	Particle Image Velocimetry
PMMA	Polymethylmethacrylate
PTFE	Polytetrafluoroethylene
Ref	Reference
ROA	Roll-Off Angle [°]
RTD	Resistance Temperature Detector
SEM	Scanning Electron Microscopy
SH	Superhydrophobic
SLIPS	Slippery liquid-infused porous surfaces
TPE-U	Thermoplastic elastomers
TSA	Tartaric Sulphuric Acid

Greek Letters

γ_i	Surface tension of ice	[J/m^2]
γ_{is}	Ice-solid interfacial energy	[J/m^2]
γ_l	Surface tension of liquid	[J/m^2]
γ_{lv}	Liquid-vapor interfacial energy	[J/m^2]
γ_s	Surface tension of solid	[J/m^2]
γ_{sl}	Solid-liquid interfacial energy	[J/m^2]
γ_{sv}	Solid-vapor interfacial energy	[J/m^2]
γ_v	Surface tension of vapor	[J/m^2]
γ_w	Surface tension of water	[J/m^2]
γ_{ws}	Water-solid interfacial energy	[J/m^2]
$\varepsilon_{EF_{Al}}$	Experimental measurement measured by strain gauges	-
θ	Contact angle	[°]
θ_A	Advancing contact angle	[°]
θ_R	Receding contact angle	[°]
θ^*	Apparent contact angle	[°]
ρ	Density	[kg/m^3]
σ	Normal stress	[MPa]
σ_c	Critical pressure required to break the ice	[MPa]

σ_t	Tensile strength	[MPa]
τ	Shear stress	[MPa]
τ_{int}	Interfacial shear stress	[MPa]
ν	Poison's modulus of ice	-
ϕ_s	Solid area fraction of substrate in contact with liquid droplet	-
ω	Angular velocity	[1/s]

Latin Symbols

A	Cross sectional area	[mm^2]
a_g	Average grain size	[mm]
b	Width of the cantilever beam	[mm]
c	Radis of flaw	[mm]
c/h	Defect size of ice thickness ratio	-
E	Young Modulus	[GPa]
E_{al}	Young Modulus of aluminum beam	[GPa]
E_{ice}	Young Modulus of ice layer	[GPa]
EI	Bending moment of cantilever beam	[Nm^2]
e	Excentricity of ice-metal composite beam	-
F	External load	[N]
f	F-factor	-
f_1	First resonance frequency	[Hz]
FE	Fracture energy	[J/m^2]
h_{al}	Thickness of aluminum beam	[mm]
h, h_{ice}	Ice thickness	[mm]
I_y	Second moment of area of the cross section about the y-axis	[mm^4]

K	Derived function depending on spray configuration	-
K_{IC}	Mode I Fracture toughness	[kPa √m]
k	Isentropic exponent of air	-
l	Length of cantilever beam	[mm]
l_{osc}	Free oscillating length of cantilever beam	[mm]
n	Fracture mode	-
m	Mass	[kg]
P_A	Air pressure of spray system	[bar]
P_w	Water pressure of spray system	[bar]
p_{st}	Static pressure	[bar]
p_t	Total (stagnation) pressure	[bar]
Q	Transverse shear force	[kg m/s^2]
q	Distributed load	[N/mm]
R	Gas constant	[J/(kg·K)]
R_a	Arithmetical mean deviation of assessed profile	[µm]
R_z	Maximum height of profile	[µm]
r	Roughness	[µm]
r_R	Radius of rotation	[cm]
S_y	First moment area	[mm^2]

T_{st}	Static temperature	[°C]
T_t	Total temperature	[°C]
t	Time	[s]
V	Speed of airflow at test section	[m/s]
W_a	Work of adhesion	[J/m^2]
$W_{a\gamma w}$	Water surface tension	[N/mm]
$w(x)$	Deflection of the beam at a position x	[mm]
$w(x,t)$	Bending displacement at a position x and time t	[mm]
x	Distance of center of strain gauge to end of the beam	[mm]

Subscripts

i	Ice
int	Interface
is	Ice-Solid
l	Liquid
lv	Liquid-Vapor
R	Rotation
sv	Solid-Vapor
v	Vapor
w	Water

Chapter 1 - Introduction

1.1 Motivation

In 1998, an ice storm became among the worst natural disaster in the history of Canada due to an amount of heavy freezing rain accumulated that was never experienced before [1, 2]. As it can be seen in Figure 1-1, this substantial icing event collapsed electricity transmission lines impeding more than two million people to go on with their daily routines and even halted many social and economic activities since they were deprived from electricity for weeks [2, 3]. This catastrophe resulted in a shocking reality, at that moment few understood the severity extent. This event gave a perspective about the consequences that are possible from icing. This costly occurrence demonstrates the need of research to foresee and try to prevent icing events. The icing problem continues to exist and we are all exposed to the consequences.

Figure 1-1: Woman walking by a collapsed transmission pylon causing massive power outage in Quebec (Robert Galbraith/Canadian Press).

Ice buildup is a recurring concern for many industrial applications [4, 5, 6, 1]. In the field of aerospace, icing can lead to an increased fuel consumption in addition to a wide spectrum of issues related to the safety and integrity of aircraft [7, 8, 9]. Aircraft statistics conclude that 12% of weather accidents are due to icing [10]. The formation of ice can occur on ground and in-flight conditions since icing events can happen in cold climate regions but also in high altitude since temperature decreases in the vertical. On ground, icing can be caused by freezing drizzle, freezing rain, frost or snow accumulation that usually grows on the upper surface of the wings, the horizontal tail plane, or the fuselage. This can hinder the plane from taking off due to insufficient lift, an increase of drag, take off stall and maneuverability [11, 12, 13]. While flying, ice builds on the front surfaces, or leading edges, of the wings, the rudder, or the engine intake. This results in an increase of drag and decrease of lift due to aerodynamic reshaping of the surface. In addition, ice formation can interfere with instrument (e.g., airspeed probes) readings and cause destructive vibrations of the measuring devices [14]. In 2009, the Air France flight 447 scheduled from Rio de Janeiro to Paris and did not make it to its final destination. Instead it crashed over the Atlantic, costing the lives of all 228 passengers and crew on board. It was reported that the pitot tubes were obstructed by ice crystal which led to a disconnection of the autopilot in addition to an incorrect reaction of the crew caused the aircraft to stall and did not recover [15]. This tragic event illustrate once again of the icing problematic.

Aerospace companies have developed ice protection technologies since the first day of aviation with the aim to mitigate the consequences of aircraft icing and to be able to fly in all weather conditions [16, 17, 18]. Since then, anti-\ and de-icing systems are in constant development, to keep flying safe, but also to reduce the costs associated with the high fuel consumption and with ice protection systems for better environmental sustainability. Ongoing research attempts to develop functional passive ice shedding coatings to implement along with active ice protection systems; the aim of combining passive de-icing coatings to active de-icing systems is to reduce ice adhesion and ease ice removal [5, 19, 20, 21]. One of the major challenges engineers are currently facing is to ensure the durability of the coatings [22, 23]. Additionally to reduce considerably the adhesion of ice,

such coatings must withstand sand and rain erosion, resist aggressive chemicals and endure extreme atmospheric conditions [24]. To address the current demand of designing reliable icephobic coatings, it is highly important to investigate the process of ice formation and the physical properties of ice formed under simulated flight conditions.

Literature and experimental data suggest that there is still a gap in understanding the mechanical behavior and the adhesion of ice in real applications [25, 26]. Additionally, it is not possible to date to compare data obtained across different laboratories, since there is no established standard testing procedure and no cross-calibration methods employed among all researchers in this field who are all using home built apparatus that on top make use of different physical principles for determining the ice adhesion strength to a surface.

1.2 Thesis Objectives

The aim of this study is to develop ice adhesion testing methodologies to ensure that the data obtained with the same or similar test rigs from different facilities could be cross-validated. Consequently, it opens the possibility to create a database of sample characterizations. Figure 1-2 demonstrates the project scopes.

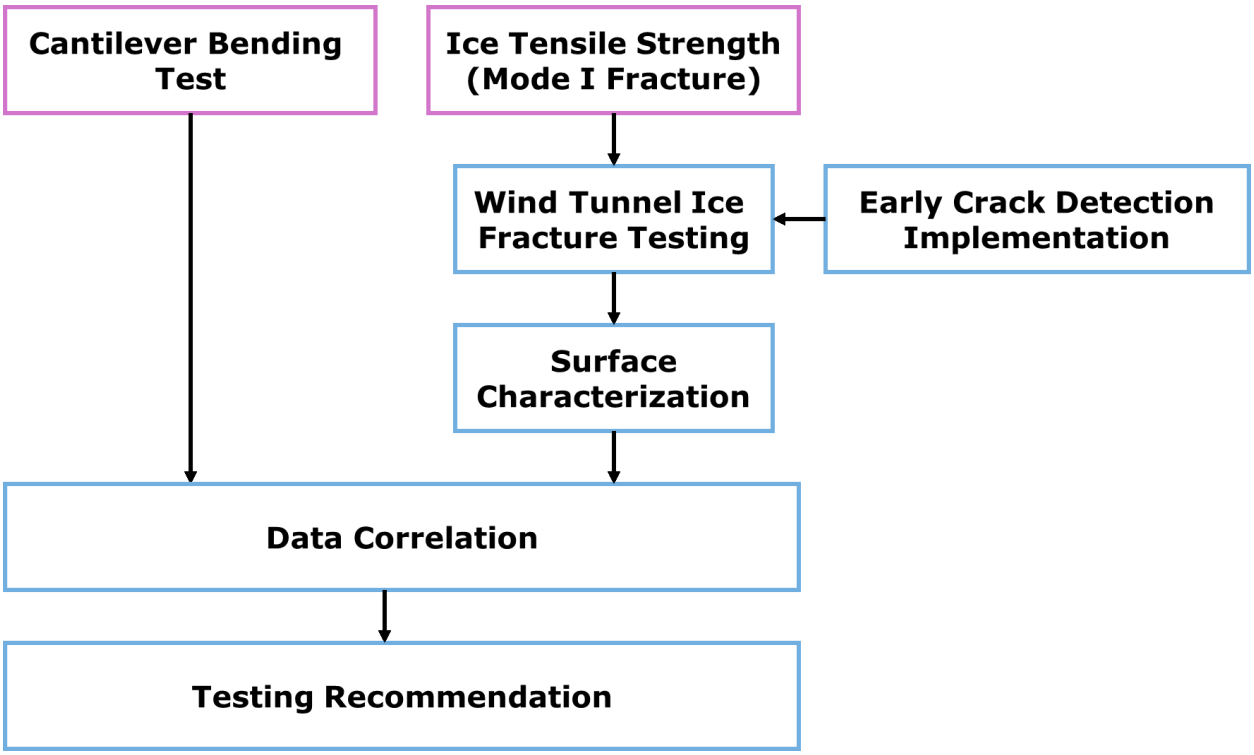

Figure 1-2: Project scope.

Thesis goals (Figure 1-2):

1. Design and implement a versatile Mode I ice adhesion test
2. Validation of the new Mode I test rig by testing reference surfaces
3. Correlate data of the new Mode I test with results from the cantilever bending test
4. Optimize testing recommendations

1.3 Thesis Organization

The thesis is organized into five chapters. A brief description of each chapter is presented below.

Chapter 1 - Introduction

To begin, a literature review of the icing problematic is presented, with a focus on the topics related to aerospace industry. The reason of performing this research is justified and the objectives are listed.

Chapter 2 - Literature Review

Theoretical background is presented in this chapter about ice accretion on aircraft, the risks associated with icing, conventional techniques used to prevent ice formation and to remove ice once it is accreted on the surface of an aircraft. Moreover, information on the topics of icephobic engineered surfaces are presented, and the procedure of testing surfaces according to their surface characteristics are used to select the potential candidates for icing wind tunnel tests. A review from the research done from previous authors about the Mode I test and other methods to measure the ice adhesion is also presented after introducing the mechanics of failure. A summary of the influences of the adhesion strength of ice to a surface is discussed. The framework of this project is clarified at the end of the chapter.

Chapter 3 - Materials & Methods

In this chapter, the iCORE (icing and Contamination Research facility) is presented along detailed specifications about the icing wind tunnel used to perform the tests in this project, and the experimental procedure of the Mode I test. A main part of the study is to implement a new testing rig, therefore, the design of the new setup is explained by presenting each subsystem. The manufacturing and preparation of the samples to be studied and the approach to characterise them are summarized.

Chapter 4 - Results & Discussion

The Mode I test rig developed in the framework of this thesis was tested to verify its functionality. This was done by repeating icing test with samples that were previously studied with the bending cantilever test. This chapter covers the testing procedure and the results obtained from the sample characterisation and the icing wind tunnel tests for the Mode I test and for the bending cantilever test. After each result, a paragraph is dedicated to the observations deriving from the obtained data and to the scientific theory. The hypothesis of possible measuring errors are given for the performed experiments.

Chapter 5 - Overview and Future Work

The final chapter summarizes the work done designing and testing a new test rig with an emphasis of the obtained results. An outlook of possible upgrades of the Mode I test and future studies are suggested.

Chapter 2 - Literature Review

Icing is a complex phenomenon and ice characteristics on a surface is affected by many factors. The atmospheric conditions (e.g., formation of clouds), wind speeds, and precipitation have an impact on the icing severity, ice type and accretion rate [12, 27]. The complexity of icing on surfaces depends on many factors including the surface chemistry, surface topography, wetting behavior, ice type, temperature, and liquid water content (LWC) [17, 28]. However, the data associated with ice adhesion strength in many cases are contradictory due to the fact that the mechanism of ice formation and adhesion is not fully understood yet [26, 29]. This chapter intends to compile the results from diverse investigations about ice adhesion strength by describing methodologies and properties of the studied surfaces.

2.1 Aircraft Icing and Frost Formation

Ice formation on surfaces of aircraft are sometimes inevitable and can be the source of catastrophic failures or events [30, 10]. In order to develop new anti-\ and de-icing technologies, one must understand how icing is initiated and all the variables that come into play — thermodynamics, heat transfer, fluid dynamics, surface chemistry and topology [21]. In the following paragraphs, the source of ice formation, type of clouds, type of ice and ice protection systems (IPS) will be explained.

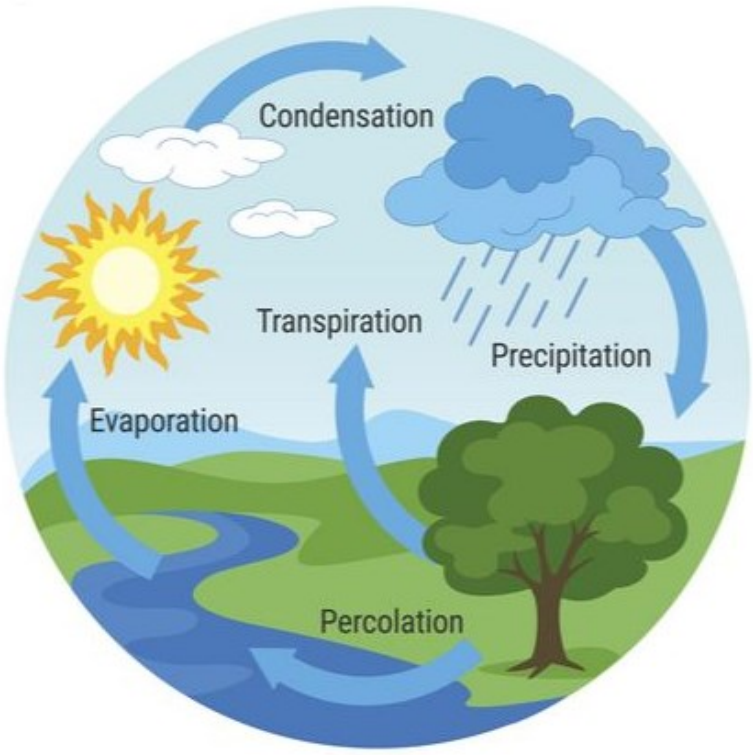

Figure 2-1: Circulation of water within the Earth's hydropshere. Rain, snow, dew and fog are forms of precipitation [31].

As shown in Figure 2-1, atmospheric icing, as a part of the hydrological cycle, is a form of precipitation encountered in cold climates and high altitudes. Water vapor condenses in the atmosphere and forms clouds as it cools. Ice or snow is formed in cold climates when the droplets of condensed water droplets are too heavy to remain in the atmosphere and fall to Earth as precipitation. Icing events are also influenced by elevated regions and hills and mountains, since the ambient temperature decreases when the altitude increases. In addition, the type of clouds will influence the severity of icing that affects aircraft flying. Dry clouds have a low potential for aircraft icing since the humidity level is low. On the contrary, wet clouds are characterize by a significant amount of moisture which in cold temperatures are filled with ice [10].

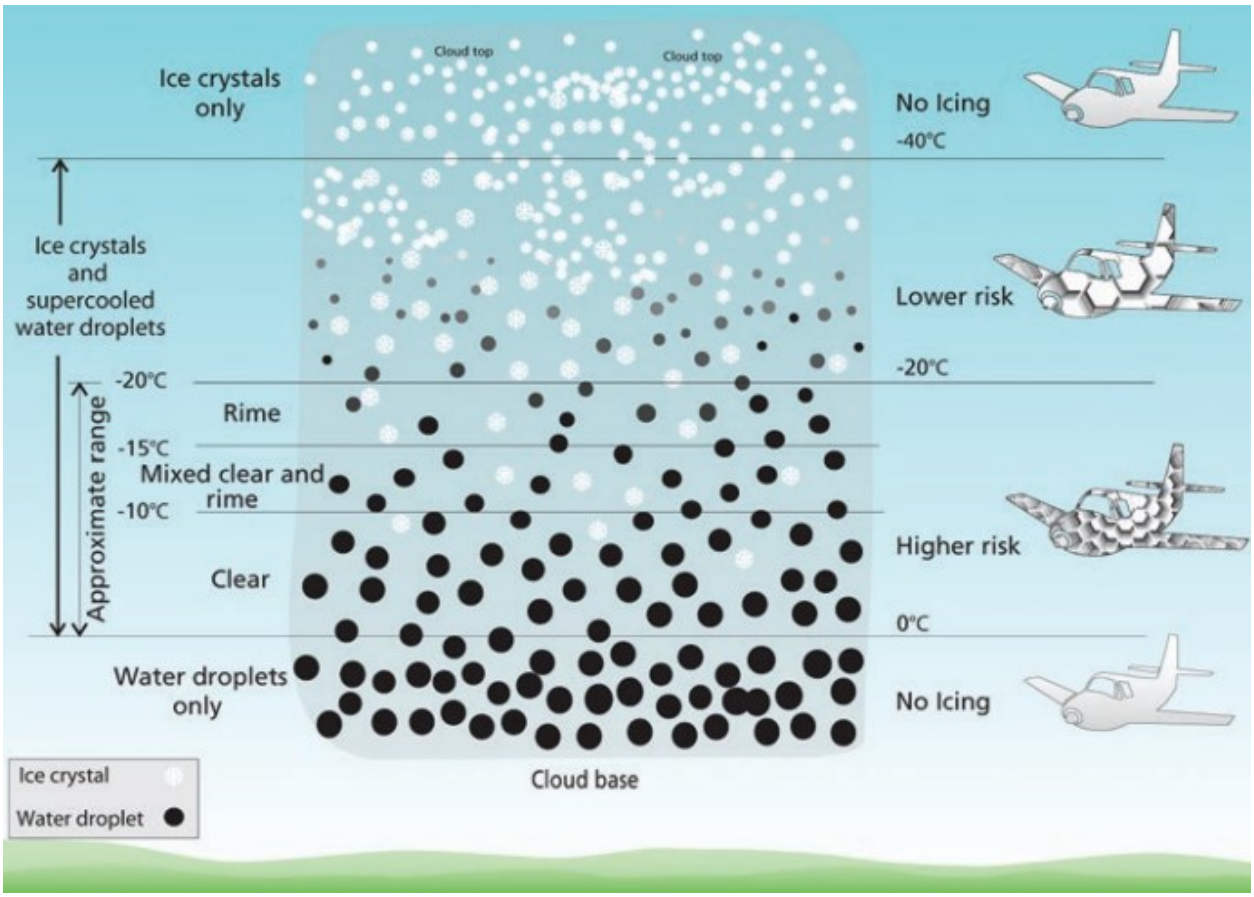

Figure 2-2: Aviation icing hazard environment [32].

Ice accretion adversely affects the control and overall performance of the aircraft and can occur on ground or in-flight. Environmental conditions directly alter the type of ice formed; depending on the meteorological conditions the size of the droplets changes, affecting the growth rate of ice and the collision with airframes (Figure 2-2). When the temperature of the water droplets in the cloud or air is below 0 °C, the water droplets supercool [21, 1, 33]. When a droplet is in the supercooled state (i.e., droplet that remains in the liquid phase below freezing point), it is in a metastable state; thereby, since the droplet is thermodynamically unstable, it can easily and quickly change phases from liquid to solid [21, 26]. Above 8 000 ft, icing is not common due to the fact that the droplets in the clouds are already frozen and ice crystals do not accrete on the cold airframe [34, 35, 36].

Depending on the weather conditions, atmospheric icing can be divided into precipitation and in-cloud icing. Rime, glaze and mixed ice are the types of in-cloud ice that adheres to the airframe skin [34, 37]. Snow and frost formation are precipitation icing that also lead to problems in the aviation industry and can adhere to all surfaces of the aircraft.

Figure 2-3: Rime (left) and glaze (right) ice [38].

Rime ice (left of Figure 2-3) is characterized by its milky white color [10]. It occurs when supercooled liquid water droplets freeze when impacting a surface having a sub-zero temperature [1, 33, 34]. This type of ice is usually brittle and is typically formed with a slow accumulation rate and the water droplets freeze almost instantaneously after impacting the surface. Air is captured between the small ice particles creating a roughness and opaque appearance. The air pockets trapping induces a low density of the ice which enhances its removal by de-icing systems. Thereby, rime ice has a rough appearance and tends to follow the silhouettes of the surface [10]. As shown in Figure 2-4, rime ice tends to accrete in low temperatures of -20 ºC to -10 ºC [34].

Glaze ice (right of Figure 2-3) tends to form from freezing rain which occurs when liquid water droplets freeze on contact with a surface with temperatures below 0 ºC [34]. This results in smooth, transparent, solid ice with little to no air pockets – thus a higher ice density – due to gradual freezing when a water droplet impacts the freezing surface [10]. Due to its high density and high accretion rate, glaze can lead to severe problems [27, 33]. In contrast to rime ice, glaze ice does not follow the contours of the surface but rather

tends to form upper and lower ‘horns’ [10].

Mixed ice is a combination of rime and glaze ice and it is commonly encountered in a temperature range from -15 ºC to -10 ºC [27].

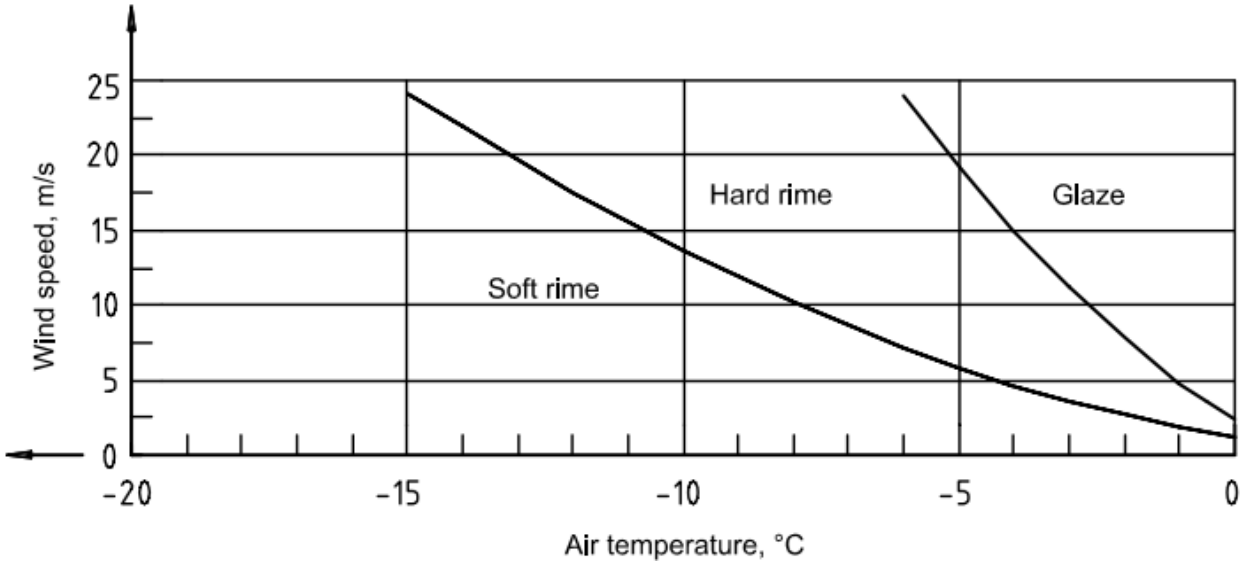

Figure 2-4: Type of ice as a function of wind speed vs air temperature [33].

The different types of clouds according to their relative heights are presented in Figure 2-5. In the aerospace field, the atmospheric clouds are categorized as continuous and intermittent maximum icing [37]. Continuous icing allows MVD values of 15-40 μm while intermittent maximum icing allows MVD up to 50 μm. LWC values are from 0.05 to 2.8 g/m^3.

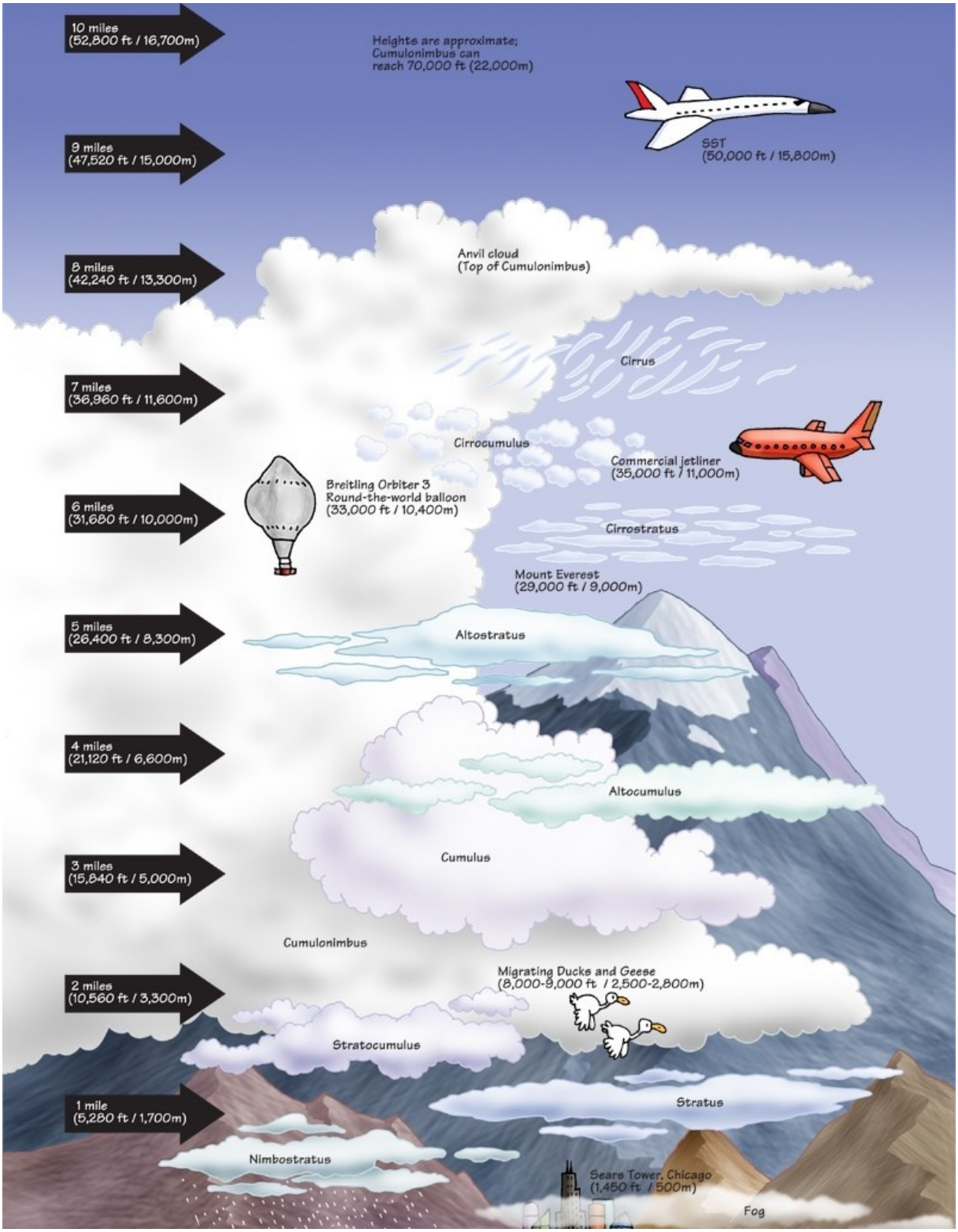

Figure 2-5: Type of clouds and their relative heights [39].

Artificial aircraft icing environments are used for certifications and are characterized by the Federal Aviation Administration (FAA) Regulation 25 Appendix C [40] by defining envelops providing maximum probable (99%) icing condition that could be encounter when flying [34]. As seen in Figure 2-6, the icing envelopes define the environmental conditions as function of temperature, median volumetric diameter (MVD) of droplets and liquid water content (LWC) of clouds that an aircraft must penetrate for continuous maximum (stratiform) and intermittent maximum (cumuliform) clouds.

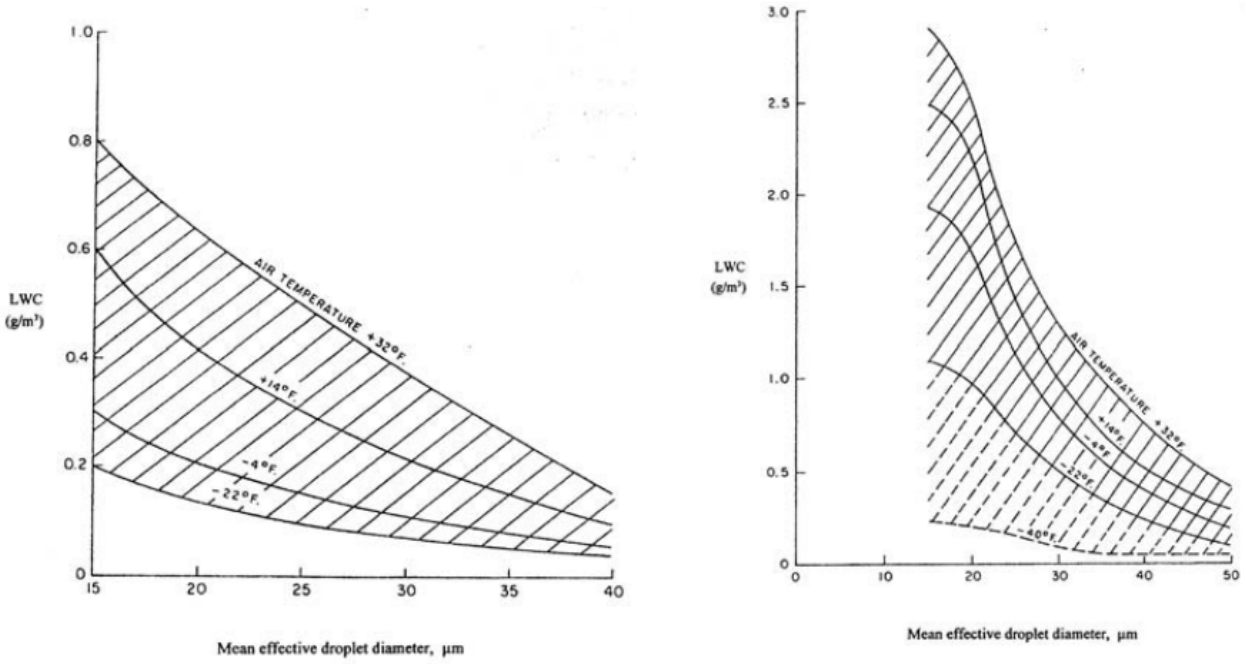

Figure 2-6: FAR 25-C curves of LWC vs MVD values for continuous icing representing stratiform clouds (left) and intermittent maximum icing representing cumuliform clouds (right) [40].

An environmental weather condition which can also contribute to ice formation is frost. This phenomenon becomes not only a problem on-ground, but also during in-flight conditions [41]. Its formation can be due to a desublimation mechanism, or due to condensation followed by freezing [30]. Once the supersaturated conditions needed for frost to form are reached, the entire surface is affected since frost has no spatial preference [30]. Consequently, the effective contact area between ice and the substrate

is greater when compared to other processes of ice formation [21]. In fact, even if experimental results demonstrated that hydrophobicity and icephobicity are proportional in some icing conditions [30], since frost nucleation is not related to surface wettability, frost can form on all surfaces of the airframe skin, even on superhydrophobic ones. The concern of frost formation in the aviation field illustrates the complexity of the ice adhesion behavior phenomena and the reason of pursuing further studies in order to develop new engineered surfaces that can prevent and inhibiting the grow of ice in all weather conditions.

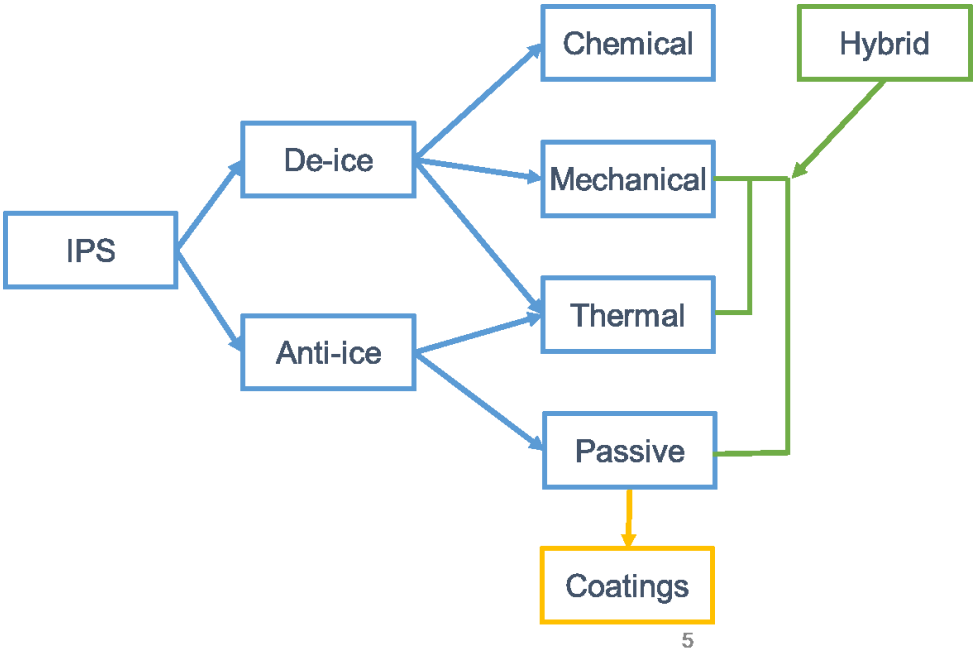

Figure 2-7: Ice protection systems (IPS).

The aviation industry is continuously striving to increase safety through the advance of cutting-edge ice protection systems (IPS) and other related technologies. As shown in Figure 2-7, IPS were developed for aircraft icing mitigation and protection by using pneumatic, chemical (coatings), thermal and mechanical methods and are classified as passive and active methods [42, 43, 44]. Passive de-icing systems prevent ice formation without any external power input or reduce ice adhesion; while active de-icing systems do employ electrical, thermal or mechanical energy to remove ice once it is accreted on

the aircraft surface (de-icing) [45] or to prevent ice from forming at all (anti-icing). An active anti-icing system used in-flight is to use the bleed air from the engine compressor to warm up the leading edges surfaces to prevent ice formation. Another example of an active de-icing system that is commonly used on small aircrafts are pneumatic de-icing boots; by inflating the pneumatic bladders, the accreted ice can be shed in critical locations as the leading edges of the airfoil [43]. Active IPS systems require the installation of systems (e.g., wires for electrical systems, tubes for the pneumatic system) that increases the overall weight and when the systems is turned on the efficiency of other components is reduced [46]. Passive systems do not involve power consumption and thus are preferred to reduce the costs associated with the energy requirements and with the environmental impact [47, 42]. De-icing systems are efficient when there is an ice layer with a certain thickness to be removed; since the presence of ice on the aircraft is undesirable at all times, passive anti-icing systems have a big advantage for reducing the potential icing hazards [45].

Significant efforts have been dedicated in the past decade to develop icephobic surfaces which will repel ice or result in very low ice adhesion strength [48, 24, 49, 23]. Importantly, these surfaces should maintain their icephobicity properties for a reasonable lifetime under practical icing conditions. This thesis will cover the testing of engineered surfaces in an environment that mimics ground and in-flight conditions.

2.2 Development of Engineered Surfaces

For some people, the lotus leaf is a symbol of purity due to its self-cleaning properties; for many scientists its topology and chemistry is the source of inspiration for developing new engineered materials to repel water.

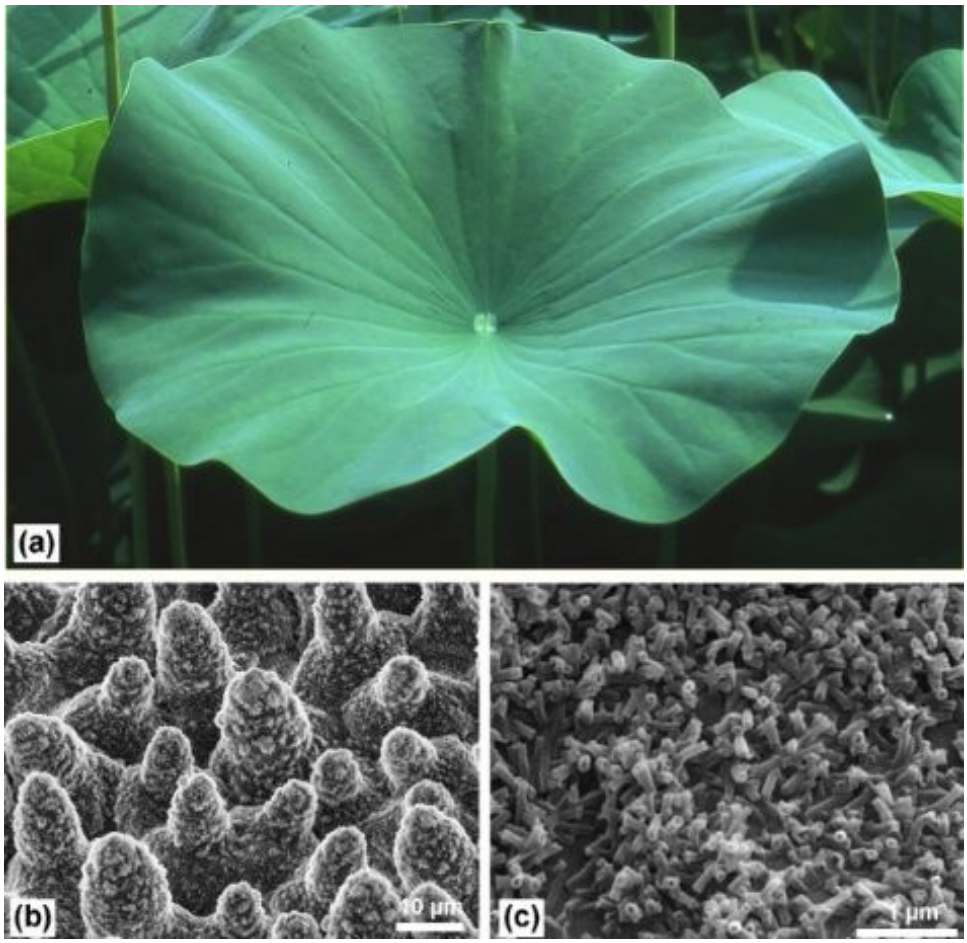

Figure 2-8: (a) Lotus leaves known by its water repellence and self-cleaning properties; (b) Scanning electron microscopy (SEM) shows the dual-hierarchy structure of micro-scale pillars covered by nano-scale bumps, and (c)nano-patterns structures [50].

The lotus effect is known in the scientific field due to two main characteristics. First, by its capability of rolling off water droplets and allowing to remove dirt, if any, without wetting its surface. Second, by its hierarchical micro-nano structure (Figure 2-8) [47]. The rough

structure of the surface allows to suspend a droplet in contact with the leaf on a trapped layer of air in between the surface of the leaf and the droplet. Consequently, the contact area and adhesion forces between the water droplet and the surface of the lotus leaf are minimized. In addition, the hierarchical structure is naturally coated with a natural wax material that allows the water droplet to roll-off easily. The contact angle of pure water on the leaf can be higher than 150° [51]. This example from nature inspired the development of superhydrophobic materials to be also used in icephobic applications. The current challenge of novel surface technologies is the assessment of the durability and protection against: rain and sand erosion; thermal exposure; UV light; corrosion and abrasion.

The meaning of vocabulary related to the topic of surface engineering can vary between different reports. Therefore, the basic vocabulary employed in this research will be defined as follows:

- → *Surface*: topmost layer of a physical object (can refer to the uppermost layer of a treated material or of the bulk material)
- → *Texture*: smoothness or roughness of an object's surface (e.g., polished, flamed (after plasma cleaning); sand blasted, etc.)
- → *Coating*: covering applied to an object's surface (also known as substrate) which can change the properties of substrate (e.g., adhesion of surface, wettability), protect surface (e.g., corrosion resistance, sealing), prevent deterioration of substrate (e.g., wear resistance) and can have decorative purposes. A wide range of different coatings is possible by controlling its composition and the application process

Efforts to mimic the lotus leaf characteristics are still a research topic to develop superhydrophobic coatings for many industrial applications. Aerospace surface technologists have been using similar natural phenomena to develop new coating technologies, but durability of the surface is limiting further progress. Another surface coating technology that also aims to diminish the surface adhesion strength is the implementation of a lubricating fluid in the coating matrix. Coatings that show noticeable anti-freezing characteristics are ultra-smooth lubricant-infused porous surfaces (LIS) and

slippery liquid-infused porous surfaces (SLIPS) [21].

The liquid layer that is imprisoned in the porosity of the matrix do not allow condensed or deposited water to penetrate into the coating, keeping a small ice-substrate contact area. While the lubricant liquid layer has significant anti-icing properties, it also limits the life of these surfaces. The liquid layer by its nature can also flow out of the porous structure and thus cannot resist multiple icing and de-icing cycles [21].

2.3 Droplet Repellency and Mobility

Ice adhesion characteristics are estimated based on their wetting behavior. When a droplet is deposited on a solid surface (metallic or polymer substrate), the interaction is known as a wetting. Measuring the liquid-solid interaction helps to experimentally characterize the surface properties. The wetting characteristics of a surface can be quantified by the static contact angle, *CA*, the roll-off angle, *ROA*, and the hysteresis contact angle, *CAH*, [21] of a (mostly water) droplet. The angle θ is measured from the contact line formed at the junction of the three phases: solid, liquid and vapor.

The wetting behavior is idealized into three different models, as shown in Figure 2-9. A droplet that impacts a solid surface and remains in its spherical shape, or easily rolls off when the surface is tilted, tends to determine if the surface has hydrophobic characteristics.

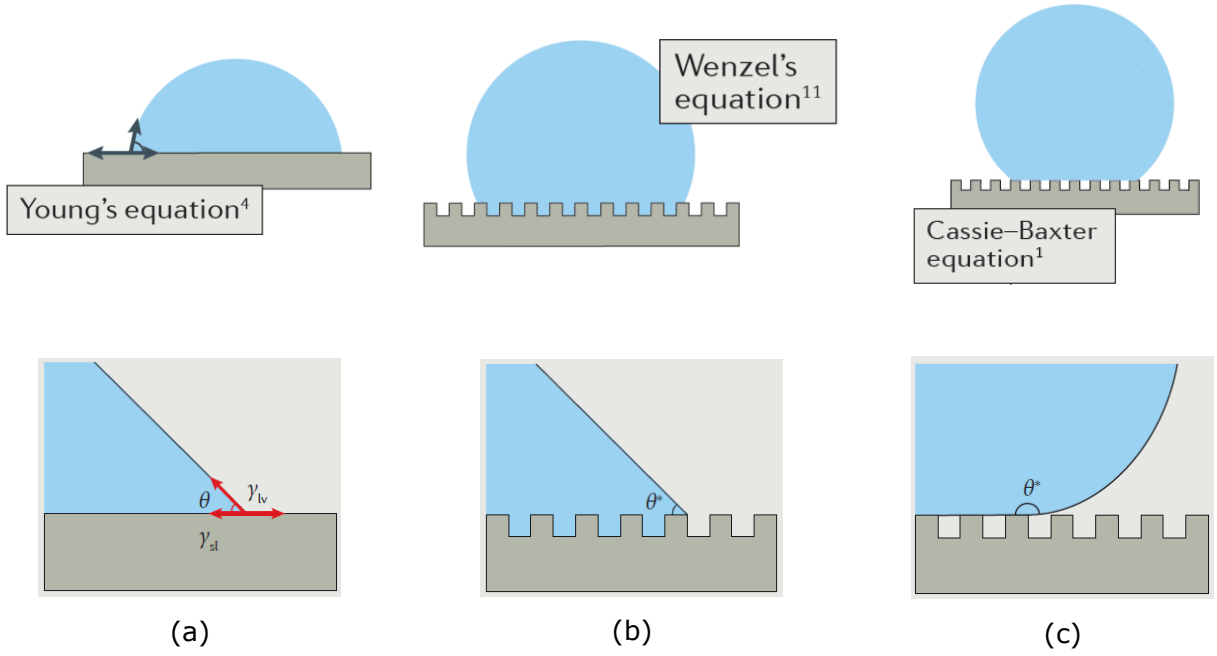

Figure 2-9: Wetting states of a liquid: (a) Young's or equilibrium state; (b) Wenzel state; (c) Cassie-Baxter state [21].

In the Wenzel state (Figure 2-9b), the liquid penetrates the voids and as a consequence the wetting surface area is larger than it would be for a drop of the same volume and apparent angle on an ideal flat solid surface. The apparent CA θ* is defined by the Wenzel formula where r represents the roughness [29]:

$$cos\theta^* = r\ cos\theta \qquad \text{Equation 2.1}$$

In a Cassie-Baxter state, the wetted surface area is smaller since the droplet sits on the vapor that has been captured in the voids, as shown in Figure 2-9c. The Cassie-Baxter equation includes the solid area fraction of the substrate in contact with the liquid droplet, $\emptyset_s$ [29]:

$$cos\theta^* = -1 + \emptyset_s\ [cos\theta + 1] \qquad \text{Equation 2.2}$$

Thus, the desired wettability features for a superhydrophobic surface are a high CA (>160°) and a small CAH (best if < 10°). A hydrophobic surface is defined by a CA $> 90°$ and an angle $< 90°$ defines a hydrophilic surface. The wettability of a substrate can be used as a guide to predict its behavior in icing conditions, but does not always guarantee that a superhydrophobic surface is icephobic, too [45]. Superhydrophobic surfaces have the further capability of repelling water droplets before they freeze and adhere on the surface [21]. Decreasing the contact time of the droplet on the surface therefore decreases the probability of a nucleation event to occur [21]. With regard to ice phobic coating, it refers to a coating that can prevent or reduce the ice accretion on the surface and also decrease the amount of force needed to remove the ice from the surface [24].

The three-phase equilibrium condition for a water droplet resting on a flat surface is given by Young's equation (Figure 2-9a), which relates the surfaces tensions of the solid/vapor (γ_{sv}), solid/liquid (γ_{sl}), and liquid/vapor (γ_{lv}) interfaces to obtain the CA [45]:

$$cos\theta = \frac{\gamma_{sv} - \gamma_{sl}}{\gamma_{lv}} \qquad \text{Equation 2.3}$$

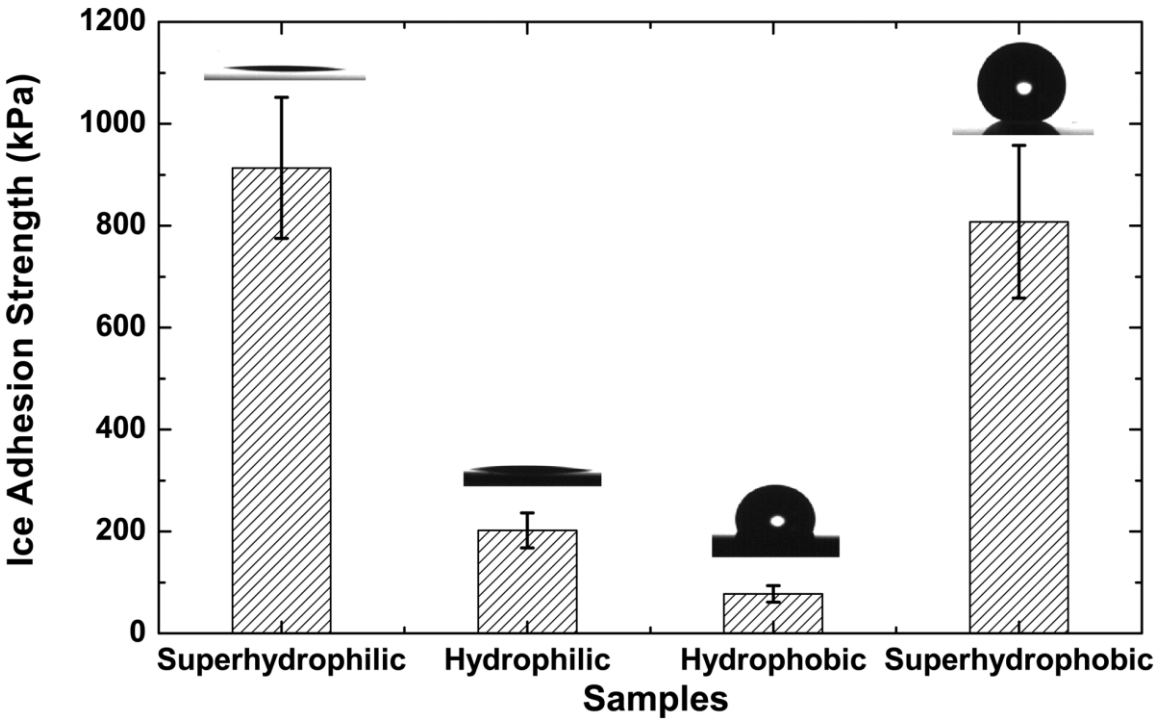

Figure 2-10: Average ice adhesion strength on four different silicon wafer surfaces (surperhydrophilic to superhydrophobic) — temperature of -15 °C and the speed of the probe of the force trasnducer was 0.5 mm/s [49].

Will a higher water CA decrease the ice adhesion? This common misconception has been proved wrong by studying the frost formation and the mechanical interlocking effects on the surfaces [30, 17, 23, 49, 52, 50]. Figure 2-10 demonstrates the ice adhesion strength results obtained for different wettabilities and it can be noted that a higher CA (superhydrophobicity) does not guarantee icephobic behavior [49]. The CA is related to the self-cleaning effect and it is a measure of the hydrophobicity of a surface but does not, by its own, characterize the icephobic properties of a surface [53]. To completely characterise wetting, the drop is studied under the influence of an external force (e.g., gravity) (e.g., a sessile drop on a tilting table) by measuring the contact angle of the droplet when tilting the surface [44, 23, 45]. As the surface is tilted, the shape of the drop starts to become asymmetric until the weight of the drop is higher than the liquid-solid adhesive strength and sliding or rolling begins. At that moment, just before the droplet moves, the ROA is observed.

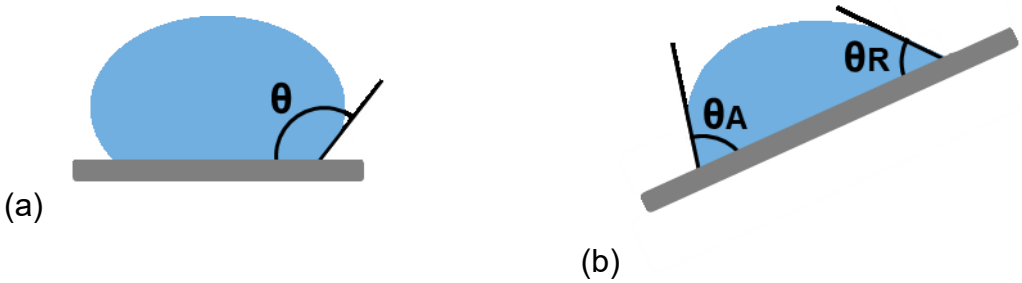

Figure 2-11: Liquid droplet on a plate tilting from an zero (a) to an angle that causes the droplet to slide (b) (ROA).

The CAH gives an indication on how mobile the drop is on the surface; thus, it is greatly dependent on the surface roughness and heterogeneity [50]. In the case of the presence of a defect or impurity on the surface, a pinning point can be observed to the droplet. As the contact line moves, due to the pinning point the CAH will an increase and perhaps the droplet will stay interlocked to the surface even at 90°. As show in Figure 2-11, the CAH, defined as the difference between the advancing, θ_A, and receding, θ_R, contact angles [54]:

$$CAH = \theta_A - \theta_R \qquad \text{Equation 2.4}$$

Ice adhesion greatly depends on the interface characteristics of the droplet with the surface, but also on environmental factors such as the humidity and gas flow [21, 45]. The environmental conditions can have an effect on the mode of nucleation [21]. Another surface characteristic that has an effect on ice adhesion is surface roughness. A rougher surface will result in higher ice adhesion strength [55, 56]. Figure 2-12 summarizes the results obtained by Koivuluoto et al. of centrifugal adhesion test for polished aluminum and polytetrafluoroethylene (PTFE). Except for the case of the smooth aluminum plate, surfaces with low roughness induces lower ice adhesion [57]. This demonstrate that ice adhesion does not solely depend on one wettability characteristics but rather on the CAH, surface roughness and surface chemistry all together [45, 57].

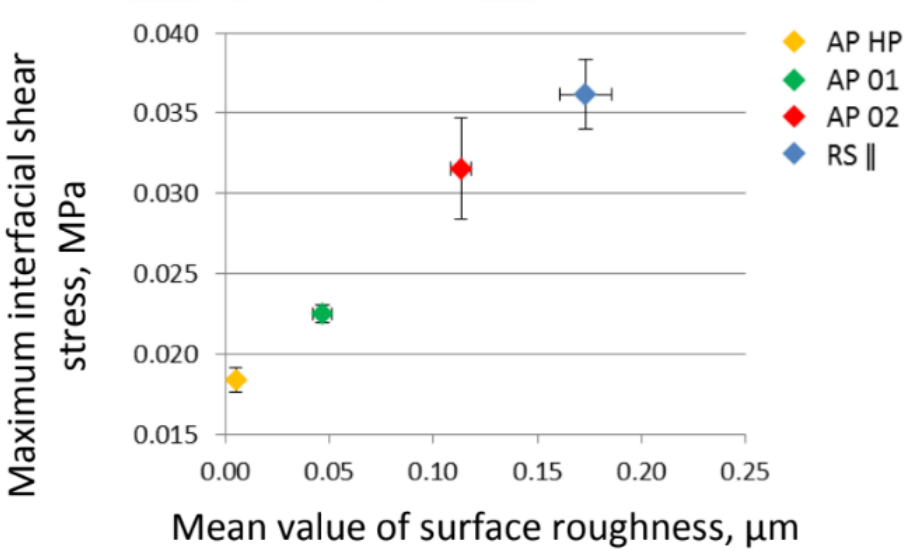

Figure 2-12: Ice adhesion vs surface roughness — bending cantilever tests performed at a temperature of -3 °C and an airflow of 90 m/s (AP HP: Aluminum samples hand polished, AP; AP 01: Aluminum samples with 30 min polishing; AP 02: Aluminum samples with 5 min polishing; RS ||: Aluminum reference sample) [55].

The wettability of a substrate can also be observed from the work, W_a, required to break the ice-solid bonds (remove the ice) and is obtained by the thermodynamic work of adhesion [45]:

$$W_a = \gamma_s + \gamma_i - \gamma_{is} \qquad \text{Equation 2.5}$$

The work of adhesion equation can be further simplified by inserting the Young's equation and assuming that the surface energies of water and ice with the solid are approximately the same ($\gamma_{is} \approx \gamma_{ws}$) [45]:

$$W_a \approx \gamma_w(1 + cos\theta) \qquad \text{Equation 2.6}$$

As observed from the simplified equation (Equation 2.6), the thermodynamic work of adhesion of ice can be approximated using the surface tension of liquid water, which is similar to the surface energy of solid ice [45]. It can be noted that in the case of a water droplet on superhydrophobic surface which will freely roll, the CA will approach 180° and

$\cos(180°) = -1$ which results in $W_a = 0$. In other words, as the liquid-solid CA decreases (the more hydrophobic the surface is), the smaller the work of adhesion becomes.

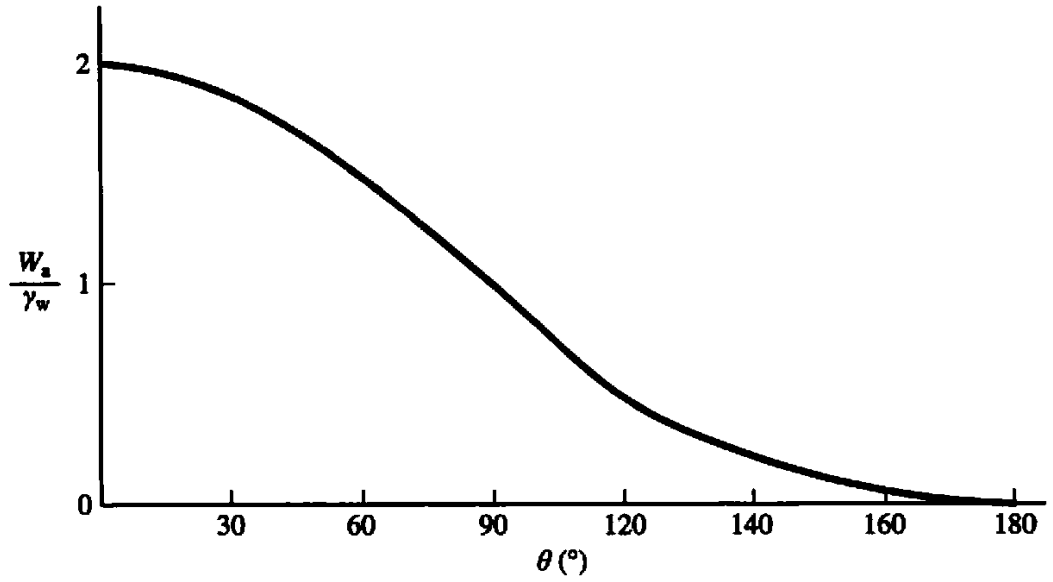

Figure 2-13: Thermodynamic work adhesion scaled by water surface tension ($^{W_a}/_{\gamma_w}$) vs water contact angle (θ) [45].

As previously assumed for Equation 2.6, if comparable interfacial energies of water and ice on the solid surface than, the work of ice adhesion (Figure 2-13) is expected to be related to the work of water adhesion and thus to wettability properties of water (γ_w, θ) [45].

2.4 Ice Adhesion Strength

To study mechanical interaction of ice and solid surfaces, following topics are investigated in the scope of the present project: fracture mechanics, fracture modes, principles of stresses and planes, ice adhesion mechanism and a review on existing ice adhesion testing techniques. The basics of fracture mechanics will explain the behavior observed during experiments. Fracture modes are useful for categorizing different failures and

understanding the mathematics employed to analyse the results. Once the mathematical analysis is completed, the ice adhesion mechanisms theory will help to validate the results. Understanding the operation of the apparatus is fundamental to characterise the testing procedure and limits.

2.4.1 Ice Adhesion Mechanisms

Fundamental understanding of ice adhesion mechanisms is required to have critical opinion on icing tests and its results. Ice adheres by physical and chemical processes onto the surface. The attachment mechanisms can be divided into three main categories [47]:

- → Mechanical clamping: when supercooled water droplets flows around the surface features and penetrates into the small cavities before freezing, and gets trapped by the expansion of water freezing into ice [58, 59]. A rougher surface tends to have more surface features and thus more anchoring points which will increase the ice adhesion strength
- → Chemical adhesion: is defined by the covalent and electrostatic interactions between electrical charge at the ice surface and the charge induced on a solid substrate
- → Thermodynamic: The cohesion of solid ice with liquid water is due to the hydrogen bonding between water molecules (hydrogen) and substrate atoms (more electronegative atom, e.g., nitrogen, oxygen or fluorine) [60]. The Lifshitz-Van de Waals are the most frequent interactions and are a consequence of dipole-dipole interactions [47]

2.4.2 Fracture Modes Principles

The manner in which the force is applied to the body will influence the crack growth. The three possible modes of deformation at the crack tip shown in Figure 2-14 are the opening mode (Mode I), where the tensile stress is normal to the crack plane; sliding mode (Mode II), where the shear stress is parallel to the crack plane; and tearing mode (Mode III), where the shear stress is not only parallel to the crack plane, but also parallel to the crack front. Thereby, in Mode I test the adhesive tensile strength of ice is studied.

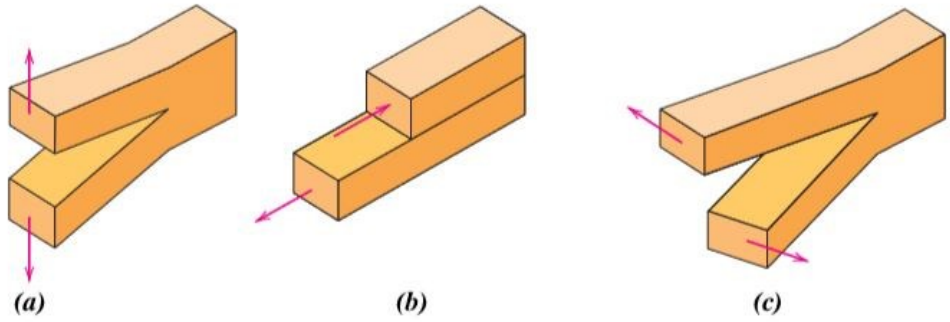

Figure 2-14: Modes of crack displacement: (a)Mode I, (b)Mode II, (c)Mode III [61].

The way an external force is applied determines how a crack will grow. However, a failure between two surfaces (ice and substrate) can result in adhesive, cohesive or mixed failure, as shown in Figure 2-15.

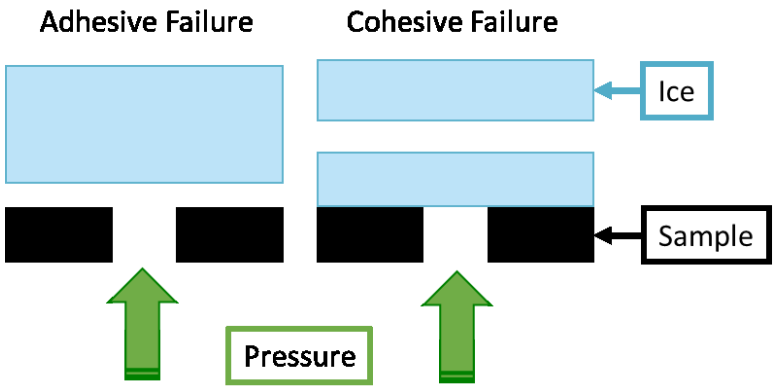

Figure 2-15: Adhesive and cohesive failure.

An adhesive bonding failure occurs when there is delamination of the ice from the substrate. The attraction of ice and substrate and the interface is the weakest and therefore when an external force is applied the two parties come apart.

Cohesive bonding failure happens when the bonding strength between the ice and the substrate is significantly stronger then the bonding attractions within the ice molecules and therefore the failure happens within the ice layer.

When the failure is partially adhesive and partially cohesive, it is said to be called mixed failure. This is observed when a region of the substrate still has some ice attached (cohesive failure) while other regions are clear of ice (adhesive failure).

2.4.1 Mechanics of Ice Fracture

The results from the ice-adhesion tests are better interpreted by understanding some simple concept of fracture mechanics. Failures that lead to fracture can happen due to distinct causes: the presence of defects in the material, poor design or construction, overloading or uncertainties in the loading, or insufficient maintenance.

A fracture is defined by the separation of a body into two or more parts when a stress is applied [61]. This separation, whose possible sources are discussed earlier in this section, is initiated at the location of a discontinuity in the body, also known as a crack formation, followed by the propagation of this flow. The mode of fracture is determined by the fashion of crack propagation. The two types of fractures are ductile and brittle, as illustrated in Figure 2-16. Crack growth is slow in ductile fracture, in conjunction with significant plastic deformation. In contrast, brittle fracture happens very quickly, with little or no plastic deformation.

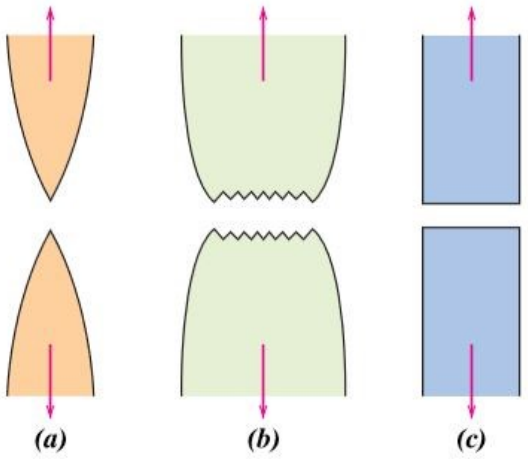

Figure 2-16: (a)Pure ductile fracture, (b)Moderate ductile fracture after necking (decrease in local cross-sectional area), (c)Pure brittle fracture [61].

2.5 Factors Affecting Ice Adhesion Strength

The ice adhesion strength depends on several factors contributing to its high level of complexity. Thus, there is neither a system nor a procedure yet to accurately provide one representative measurable for ice adhesion. The available systems aim to relate the ice adhesion characteristics to the wettability properties and to different engineered surfaces.

A droplet that impacts a solid surface and remains in its spherical shape, or easily rolls off when the surface is tilted, tends to determine if the surface has hydrophobic

characteristics and to what extent. Thus, the desired wettability features for a superhydrophobic surface are a high CA (>160°) and a ROA as small as possible (best if < 10°). A hydrophobic surface exhibits and CA above 90° while the CA of a hydrophilic surface is below 90°.

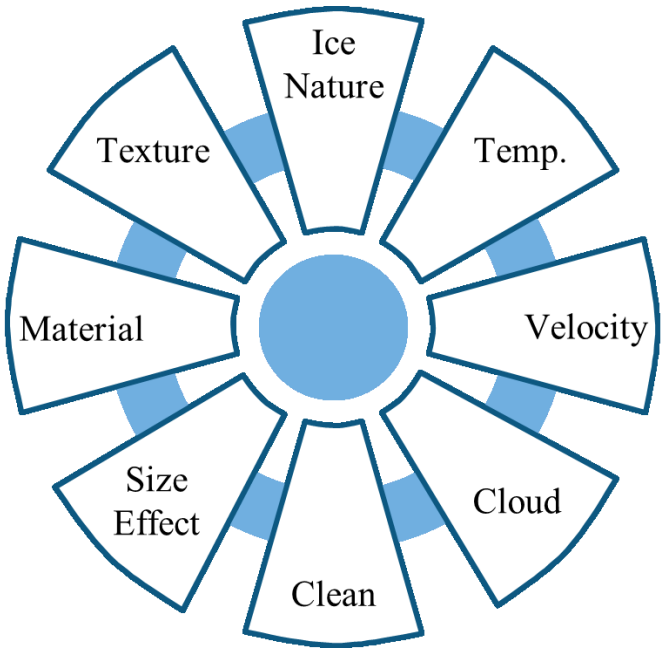

Figure 2-17: Factors affecting ice adhesion strength.

The major factors influencing the ice adhesion to a surface are illustrated in Figure 2-17. The nature of the ice (sea, tap or demineralized water) will disturb the structure of ice. The temperature of the droplets and the temperature of the substrate surface can contribute to the locked thermal strain energy. The cloud characteristics will induce different type of ice growth. Higher velocity of droplets impacting the surface induces stronger interlocking of the droplets onto the surface. The material characteristics affect the ice strength depending on the surface roughness, the porosity, the stiffness, etc. The surface roughness can mechanically influence the ice adhesion since the water droplets can slide into the asperities and become interlocked as freezing, which means that a higher force will be required to detach the ice from the surface. Different water droplet in

size will interact different with a same substrate. If the water droplets are significantly smaller compared to the surface roughness of the substrate, they are likely to have a higher tendency to go into the asperities of the surface and become interlock due to the expansion as a result of freezing. Thus, hydrophilic surfaces lead to higher ice adhesion. In addition, there is a tendency for the sample substrate to have a higher ice adhesion strength for the glaze ice condition. As mentioned in previous section, glaze ice is known to have a higher density compared to rime ice, which is seeded with air pockets.

Characterizing the wettability characteristic of a surface by measuring the contact angles and surface roughness, allows to later establish a prediction factor, if any, to determine if a sample will be promising under the icing wind tunnel (IWT) tests by looking at its contact angles and surface roughness. Some of the most common ice adhesion tests will be briefly introduced in the following sections.

2.6 Review of Ice Adhesion Testing Approaches

Ice adhesion depends on several factors that are covered in previous sections, which contribute to its high level of complexity. Thus, there is neither an unique system nor a procedure yet established to accurately measure the ice adhesion strength for all weather conditions. The available systems aim to relate the ice adhesion characteristics to the wettability properties and to different engineered surfaces.

2.6.1 Centrifuge Adhesion Test (CAT)

A coupon of the surface to be investigated is installed at one end of the beam as shown in Figure 2-18 and to achieve balance, a counter weight is installed on the other end. Ice is formed on top of the surface and the beam is spun inside a close chamber at a constant increasing angular velocity, ω, until the ice separates from the surface. Piezoelectric cells installed on the walls of the chamber detects the moment that the ice hit the surface. Assuming uniformly distributed shear stress at the ice-surface interface, the shear strength of the ice is derived through mathematical calculations. The centrifugal force can be obtained from the mass of the ice, m, the radius of rotation, r_R,:

$$F = m r_R \omega^2 \qquad \text{Equation 2.7}$$

A drawback is that the ice is grown outside the testing rig, and thus it must be manipulated from the support to install it on the CAT prior testing. This can introduce mechanical variations to each sample. If the transfer of the ice is done in a cold chamber, thermal stresses will create little or no variations within the samples. Also, since the ice is sprayed onto the surface, the ice shape is difficult to control which brings other variations to the results of ice adhesion.

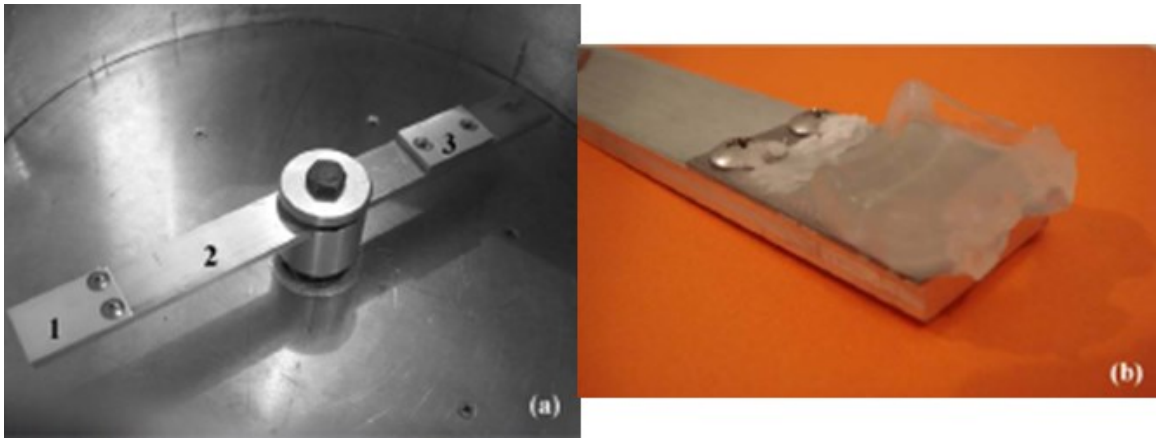

Figure 2-18: (a) Centrifuge setup of aluminium sample: 1) Candidate coating, 2) Beam, and 3) Counter weight. (b) Ice coupon (glaze ice) [62].

2.6.2 Mode I (Tensile) Adhesion Test

Andrews and Stevenson were interested in studying cohesive and adhesive fracture of epoxy in plane strain conditions to overcome the uncertainties of plane stress experiments [63]. The critical pressure required to initiate a crack is obtained and then it can be translated to the critical energy release rate or fracture energy [64]. As shown in Figure 2-19, oil was pumped and stabilized by a nitrogen filled pressure accumulator. An induced bubble trapped in the high pressure tubing acted as a pressure fluid to initiate the crack in the sample holder. The pressure was continuously measured by the transducer and recorded into a chart.

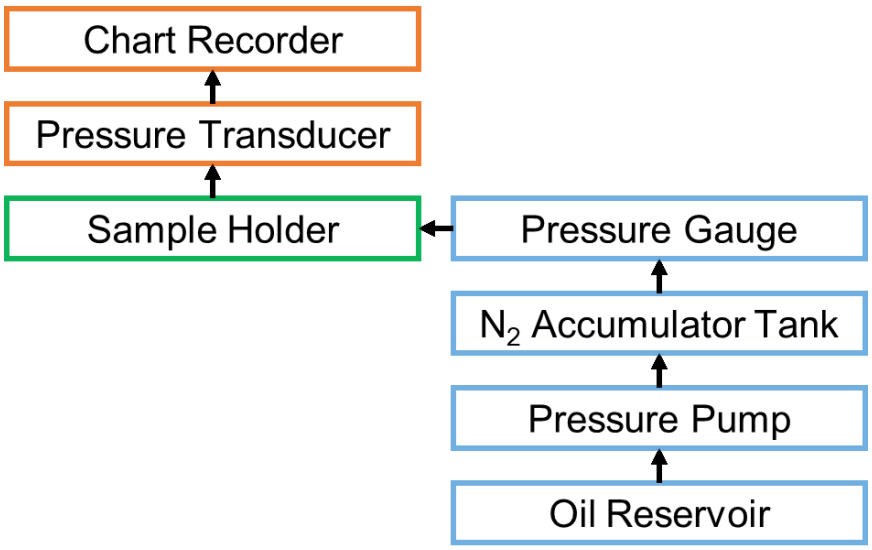

Figure 2-19: Andrews & Stevenson [63] test rig setup illustration.

Andrews and Lockington applied the testing methodology to measure the ice strength on stainless steel, titanium and anodised aluminum samples [64]. As illustrated in Figure 2-20, the ice was casted on a circular and hollow substrate. The inner hole of the substrate was covered by a small PTFE disk with a thickness of 250 μm due to its non-adhering properties, which would act as a defect and initiate crack formation once pressure was applied [63].

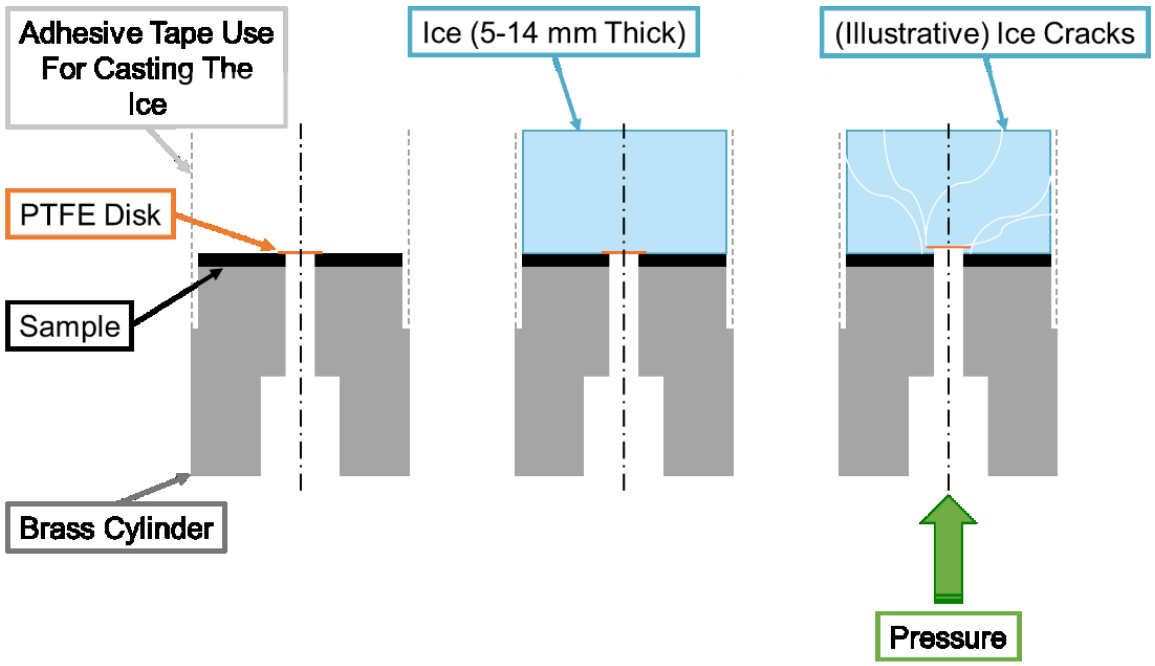

Figure 2-20: Andrews & Lockington [64] test preparation (left), ice casting (middle) and ice fracture (right) (PTFE: Polytetrafluoroethylene).

It was observed that fracture energy measured strongly depends on the amount of air trapped in the ice. Another obtained result was the transition of cohesive to adhesive fracture (Figure 2-21) depends on the pressure loading rate (fracture energy increases at a slower pace as the temperature decreases).

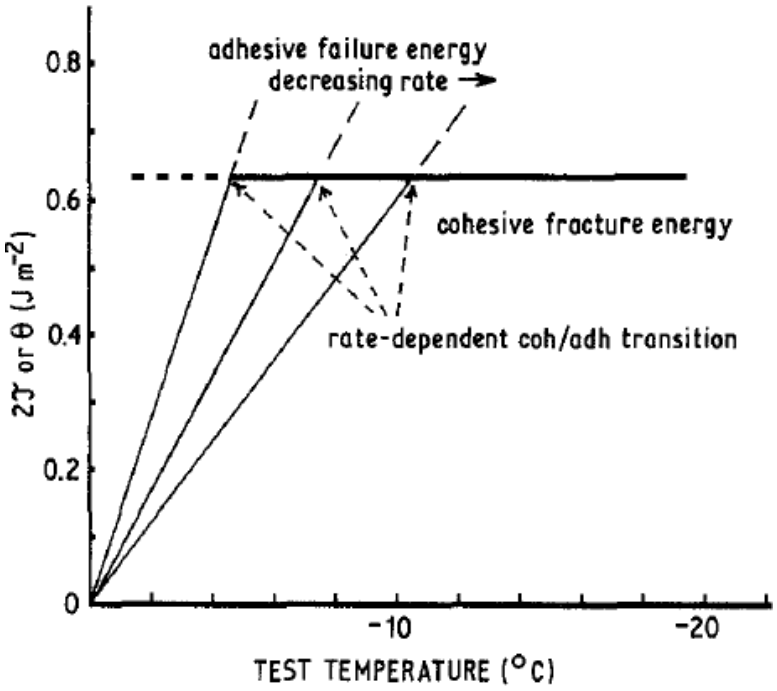

Figure 2-21: Fracture energy vs test temperature diagram showing cohesive-adhesive failure transition [64].

The following equation is based on the Young's modulus of ice, *E*, the critical pressure for failure experimentally obtained, σ_c, the size of the defect, *c*, and the f-factor, *f*:

$$FE = \frac{\sigma_c^2 \, c}{E \, f} \qquad \text{Equation 2.8}$$

The fracture energy is inversely proportional to the f-factor, which depends on the ratio of defect size and ice thickness, *c/h* the fracture mode, *n*, and the Poison's modulus of ice, ν:

$$f = \left(\frac{1}{1-\nu^2}\right)\left\{\frac{3}{32}\left[\left(\frac{c}{h}\right)^3 + \left(\frac{c}{h}\right)\left(\frac{4}{1-\nu}\right)\right] + \frac{n}{\pi}\right\}^{-1} \qquad \text{Equation 2.9}$$

Where *n* is equal to 1 when the failure is adhesive or it is equal to 2 if the failure is cohesive.

The Mode I fracture toughness, K_{IC}, can be obtained from the fracture energy [64]:

$$K_{IC} = \sqrt{\frac{FE * E}{1 - \nu^2}} \qquad \text{Equation 2.10}$$

The tensile strength is based on the average grain size, a_g, and the fracture toughness [65, 38]:

$$\sigma_T = \frac{K_{IC}}{\sqrt{\pi * a_g}} \qquad \text{Equation 2.11}$$

Based on previous investigation, the values for the Poisson's ratio and the Young's modulus used were 0.31 and 8.5 GPa, respectively [38, 64, 66]. Since it is not possible to obtain the grain size from the microstructure pictures, the size of the defect is assumed to also be the grain size [38], which is a reasonable assumption according to research.

Hammond integrated this test to perform ice adhesion studies in an environment mimicking in-flight conditions simulated inside a running icing wind tunnel [38]. As illustrated in Figure 2-22, Hammond adapted the Mode I test system to perform experiments inside the icing wind tunnel by using nitrogen gas instead of an oil fluid to pressurize the specimen in order to initiate a crack and implemented the use of a vacuum system to maintain the small PTFE disk in place [66].

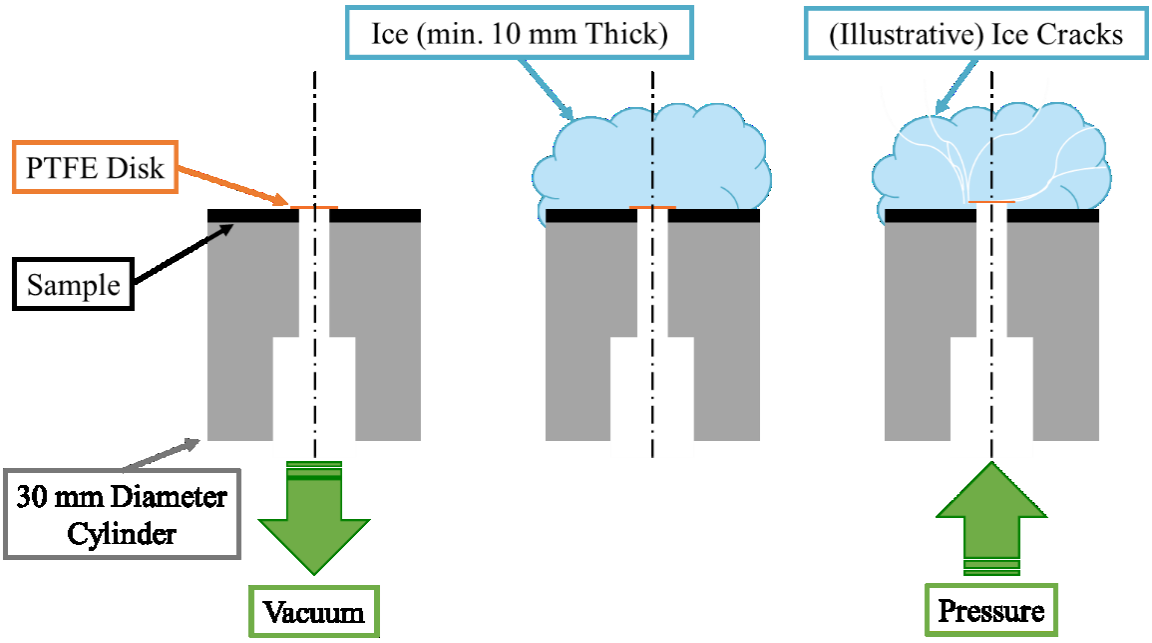

Figure 2-22: Hammond's [66] test preparation (left), ice formation in IWT (middle) and ice fracture (right) (PTFE: Polytetrafluoroethylene, IWT: Icing Wind Tunnel).

Adhesive and cohesive fractures were measured on aluminium, nickel and titanium samples from rime to glaze ice. Hammond observed that more energy was required to crack the ice as the temperature was lowered and a cohesive fracture occurred more often. This adapted test allowed to achieve reproducible tests inside the icing wind tunnel, which eliminated the thermal stress induced to the ice when manipulated outside a cold chamber as in the Andrews and Lockington test procedure. The pressure rate is also a controlled parameter which allows to regulate the applied load rates.

To insure plain strain conditions, Andrews and Lockington [64] derived the equation to obtain the fracture energy after studying the adhesion level of ice and concluded that the ice thickness is 2.5 times the defect size (the inner hole of the sample) [64].

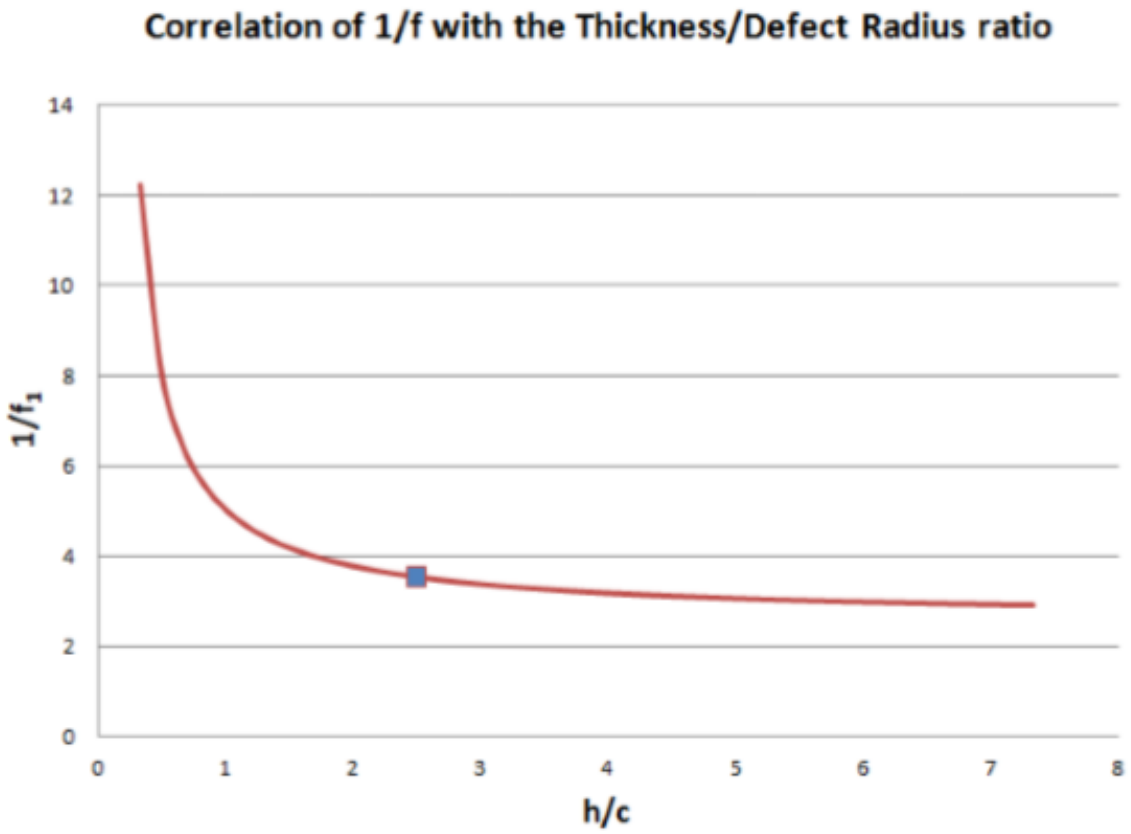

Figure 2-23: Influence of ice thickness and defect size (h/c) in inverse of the f-factor. Defect size was considered to be 3 mm, adhesive fracture was assumed and the thickness was varied to find plain strain conditions within ice [67].

Moncholi performed icing studies in the Cranfield University laboratory and shows that at a 2.5 ratio the value of *1/f* is not significantly affected as the thickness increases (Figure 2-23) [67]. The inverse of the f-factor is proportional to the fracture energy, thus by assuming a defect radius of 3 mm, it is observed that the effect of ice thickness does not influence the fracture energy when ice is thicker than 10 mm.

2.6.3 Mode II (Shear) Ice Adhesion Test

Developed at Cranfield University [38], the shear strength test rig (Figure 2-24) works by the principle of pushing the accreted ice by the movement action of a plunger. The measured pressure needed to move ice accreted in the running icing wind tunnel is used into the finite element analysis allowing to calculate the shear strength.

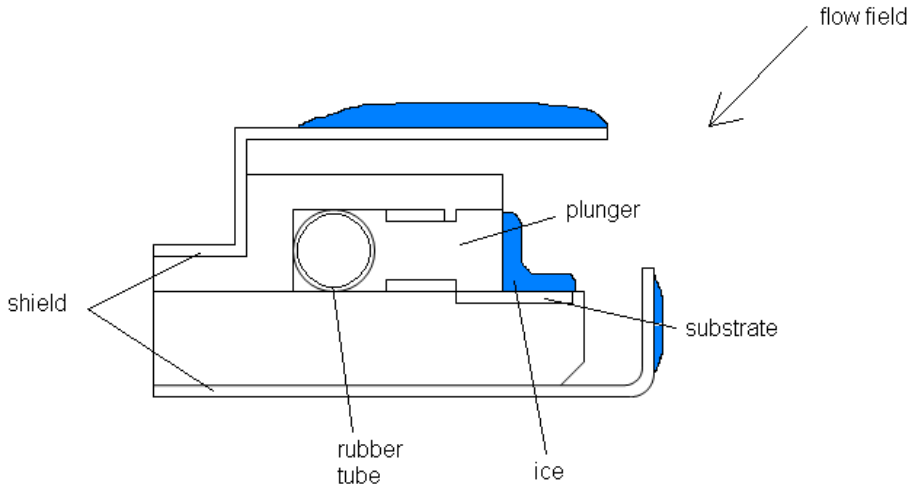

Figure 2-24: Schematic diagram of the shear (Mode II) test jig [38].

The test rig is placed at a 45° to the flow stream. When running a test, the ice will cover all the test rig and the moving parts must be blocked. In addition, since the ice will be formed on the sample and the plunger, the ice adhesion will not only be from the sample but also from the plunger. In addition, after running each test, the complete pressurization system must be purged manually which increases the testing time.

2.6.4 Cantilever Bending Test

An alternative method for studying ice adhesion was developed at the Airbus CRT facilities by accreting ice in an icing wind tunnel on a rectangular beam and investigating

the harmonic excitation with an electromagnetic shaker. The vibrations initiates the ice-substrate interfacial debonding. The analytical model was developed by Strobl et al [68]. As seen in Figure 2-25, beam theory is used to calculate the neutral axis (denoted N.A. in Figure 2-25) of the ice-substrate beam and the maximum magnitude of the internal shear stress can be obtained. The eccentricity *e* of the ice-metal composite beam is given by:

$$e = \frac{1}{2\left(h_{al} + \frac{E_{ice}}{E_{al}} h_{ice}\right)} \left(h_{al}^2 - \frac{E_{ice}}{E_{al}} h_{ice}^2\right) \qquad \text{Equation 2.12}$$

Where h_{al} and h_{ice} are the thickness of the beam (in this case made of aluminum) and the ice respectively, E_{al} and E_{ice} are the Young's moduli of the beam and ice layer.

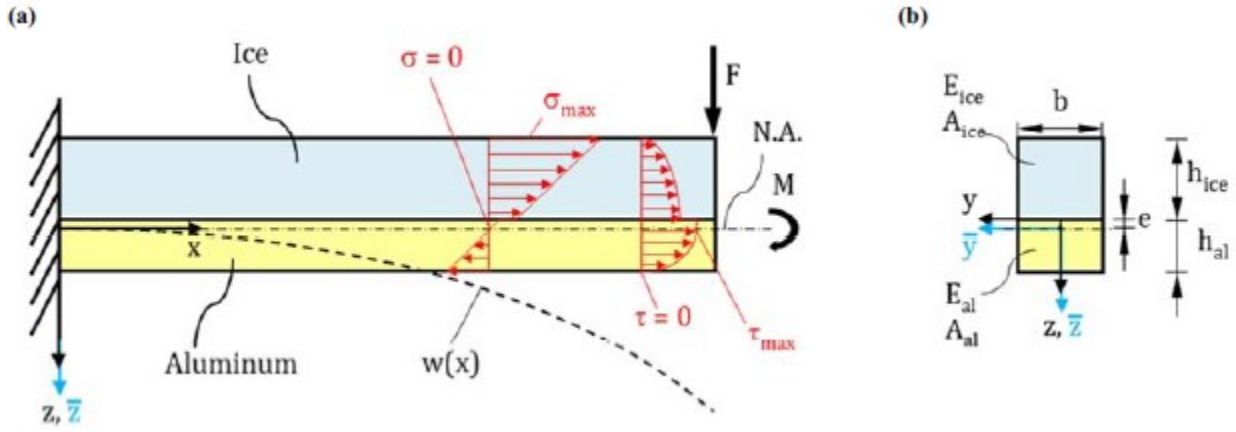

Figure 2-25: (a) Side view of aluminum beam with ice accreted and resultant normal (σ) and shear (τ) stresses as a reponse of an external load (F) application. (b) Cross-section of the aluminum beam with ice accreted on top [68].

Euler-Bernoulli beam theory is employed to obtain the displacement and resultant internal stresses as a response of an external load application. It is assumed that the cross section of the beam is homogenous and rectangular and that the cantilever is initially undeformed:

$$EI_y = \frac{d^4w(x)}{dx^4} = q \qquad \text{Equation 2.13}$$

Where E is Young's modulus of the material of the beam, I_y is the second moment of area of the cross section about the y-axis, $w(x)$ is the deflection of the beam at a position x along the x-axis and q is the distributed load.

The shear stress τ can be obtained by the following equation:

$$\tau(\vec{z}) = \frac{QES_y(\vec{z})}{EIb(\vec{z})} \qquad \text{Equation 2.14}$$

Where Q is the transverse shear force, E is the young modulus, S_y is the first moment of area, EI is the bending stiffness of the beam and b is the width of the beam.

The interfacial shear stress τ_{int} of ice-aluminum composite beam is obtained by:

$$\tau_{int} = \frac{\varepsilon_{EF_{Al}} E_{ice}(h_{ice}^2 + 2h_{ice}|e|)}{2(x-l)(h_{al} - |e|)} \qquad \text{Equation 2.15}$$

Where $\varepsilon_{EF_{Al}}$ is experimentally measured by a strain gauge and represents the strain at the extreme fiber at the bottom layer of the aluminum beam, x is the distance separating the center of the strain gauge and the end of the beam that is clamped, l is the length of the composite beam, h is the measure of thickness, e is the eccentricity.

The sinusoidal input signal to excite the cantilever beam causes a dynamic bending:

$$\frac{EI_y}{\rho A}\frac{d^4w(x,t)}{dx^4} + \frac{d^2w(x,t)}{dt^2} = 0 \qquad \text{Equation 2.16}$$

Where ρ is the density, I_y is the second moment of area of the cross section about the y-axis, A is the cross sectional area of the beam and $w(x,t)$ is the bending displacement at

a position *x* and time *t*. The first resonance frequency of the cantilever beam gives the maximum dynamic bending stress and is obtained by:

$$f_1 \approx 0.560 \sqrt{\frac{EI_y}{\rho A l_{osc}^4}} \qquad \text{Equation 2.17}$$

Where l_{osc} is the free oscillating length of the beam.

The drawbacks of this test are that the stress concentrations at the edges of the substrate material are not taken into consideration. In addition, the analytical solution assumes a constant cross sectional area for the ice layer, which differs from the reality since the thickness of the ice is a maximum at the center of the beam and decreases near the ends.

2.6.5 Summary of Ice Adhesion Data from Literature

Anti-\ and de-icing methods are been used in various industries to lower the ice adhesion and to remove ice once it is accreted on a surface. The development of engineered surfaces to mitigate the ice adhesion problem has gained popularity with the years. The values presented in the literature obtained from ice adhesion testing for aluminum samples are presented in Table 2-1. The best values are found from CAT and the adhesion strength measured was less than 1 kPa. Significant higher values of 2 800 kPa was measured by bending cantilever test. The measuring techniques for ice adhesion testing can greatly affect the result obtained. Each testing rig will create a failure in a different manner e.g., by using an external compressive or tensile load, by using centrifugal forces, etc. Even when comparing results obtained by the same measuring technique, the absolute number of the ice adhesion data cannot be directly compared. The sample preparation, surface characteristics of the sample, measuring techniques, and experimental data affect the results obtained; thus, the data obtained from laboratories experiments is useful to perform a screening with different surfaces.

Table 2-1: Summary of ice adhesion results presented in the literature.

Sample		Size	Ice Adhesion	Test	Ref
Substrate	**Description**	**[mm]**	**[kPa]**		
Al6061	**Mirror-polished**	**32x50**		**CAT**	[62]
Aluminium	Polished	340x30	~380	CAT	[57]
Al6061	Polished using 1 μm diamond suspension	25x75x1	1039±117	-	[69]
Al6061	Sandblasted with a medium grit	25x75x1	1373±130	-	[69]
Al6061	Sandblasted with a coarse grit	25x75x1	1583±125	-	[69]
Aluminium	Etched - superhydrophobic	-	~110	tensimeter equipped with PCS (Peltier cooling stage at -19 °C	[70]
Aluminium	Etched - hydrophobic	-	~70		[70]
Aluminium	Etched - hydrophilic	-	~170		[70]
Al6061-T6	Polished	340x31.8x6.3	0.780±0.102	CAT -hard rime ice	[71]
Al6061-T6	Polished	340x31.8x6.3	0.529±0.119	CAT – impact ice	[71]
Al6061-T6	Polished	340x31.8x6.3	0.284±0.083	CAT – clear ice	[71]
Aluminium	Polished with 220 grit	50x50	450±70	Shear testing	[72]
Aluminium	Polished with 400 grit	50x50	390±60	Shear testing	[72]
Aluminium	Polished with 1000 grit	50x50	340±40	Shear testing	[72]
Aluminium	Polished with 2000 grit	50x50	300±60	Shear testing	[72]
Aluminium	Mirror finish	50x50	130±60	Shear testing	[72]
Aluminium	NeverWet	50x50	420±40	Shear testing	[72]
Aluminium	Hydrobead	50x50	370±90	Shear testing	[72]
Al6061-T6511	Polished with 180 grit	280x25.4x3.1	2800±90	Bending cantilever test - 12 °C	[73]
Al6061-T6511	Polished with 400 grit	280x25.4x3.1	1500±60	Bending cantilever test - 12 °C	[73]

2.7 Context of Research

Within the conceptual framework of the above sections, the plan is to develop an optimized Mode I test rig adapted for the Airbus CRT facilities. This will allow to characterize the ice adhesion of different reference substrates which results will be compared with those obtained from the bending cantilever test. As this is an industrial project, the goal is to develop a test in order to screen different surfaces in an icing wind tunnel as a mean to rank their icephobicity and not to perform fundamental research about icing. Having various approaches to study the ice behavior on a surface allows to have a more complete understanding of the adhesion mechanisms. The Mode I test will give an idea of the tensile strength needed to detach the ice from the surface while the cantilever bending test gives the compressive/tensile stresses at the ice-substrate interface. The reason of choosing the implementation of the Mode I test in contrast of others possible testing devices is due to its simplicity of experimentally procedure and analytical computation employed to derive the adhesion strength of ice. The possibility of being able to accrete the ice and perform the experiment in the same chamber (in the test section of the IWT) without any manipulation required reduces the input of possible influencing factors to the adhesion mechanism (thermal stresses). The Mode I test is capable of reproducing repeatable test according to other authors using it [38, 67, 66].

Chapter 3 - Methodology

The focus of this study is to implement a new test rig to further contribute to the research of ice accretion on engineered surfaces of aerospace applications. The new Mode I test setup is described in this section with detailed explanations about the development of each of its components. iCORE Airbus testing environment is also presented along the related characteristics to the ice adhesion testing.

3.1 iCORE Icing Wind Tunnel Set Up

In addition to the wind tunnel conditions (e.g., airflow velocity, test section temperature, liquid water content (LWC), and median volumetric diameter (MVD)), the critical pressure to break the ice, the type of fracture (adhesive, cohesive or mixed) and ice thickness needed to be measured and monitored for each test performed.

Airbus Central Research & Technology (CRT) has an Aerodynamic Efficient Surface Lab equipped with a small-scale icing wind tunnel (Icing and Contamination Research facility). Inside the 150x100x500 mm test section, an environment can be recreated to mimic in-flight conditions (Figure 3-1) [74]. The test section is composed by a structural frame and four polymethylmethacrylate (PMMA) walls with a thickness of 15 mm each. The structure made out of three layers of spruce wood (with insulation material) allows modularity of sections in addition to simplicity when implementing modifications for new sensors or other instruments. The inner walls of the tunnel is varnished to impede moisture to degrade the wood. The envelope of the total temperature and airflow velocities ranges is presented in Figure 3-2.

Figure 3-1: iCORE icing wind tunnel [75].

Temperature, airflow speed in the test section, and LWC are the principal icing parameters controlled in such an environment. The closed loop icing wind tunnel consists of a circuit where air is pulled by a centrifugal fan (DMVL-710-1-75) 22 kW [76] controlled by a variable frequency drive with a range of 0 to 50 Hz (generating a range airflow speeds in the test section from 0 to 150 m/s). Controlled speeds up to Mach, *Ma,* 0.45 can be reached in the test section [77]. Low temperatures reaching down to -30 °C are induced by the condensing unit with a heat exchanger of 17.5 kW [77].

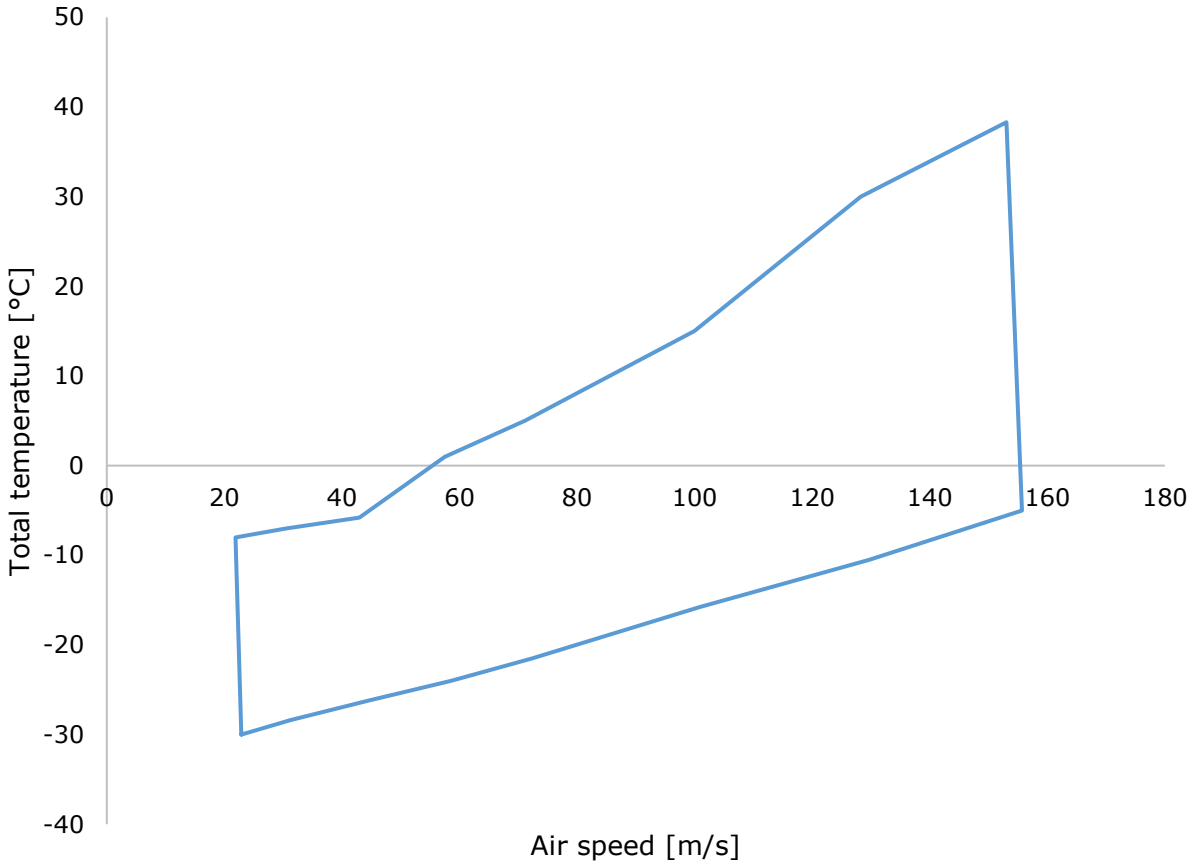

Figure 3-2: Operation envelope of iCORE for closed and open loop configuration [78].

The experiments carried out in this project intend to mimic the ice conditions which lead to elevated risk of ice formation according to the Appendix C [35]. The conditions used for the testing of this project are a temperature of -20 ºC and -5 ºC, LWC varying in the range from 0.3 to 1.0 g/m^3 with a MVD of 20 µm (Table 3-1).

Table 3-1: Icing conditions (supercooled droplets) used during ice adhesion tests for this project.

Ice Type	Total Air Temperature (T_t)	Airspeed (V)	Liquid Water Content (LWC)	Mean Effective Droplet Diameter (MVD)
	[°C]	[m/s]	[g/m^3]	[µm]
Rime	-20	50	0.3	20
Glaze	-5	80	1.0	20

The velocity is continuously monitored upstream in the test section by a pitot-static tube (PAA-8-KL) [79]. This measuring instrument is placed at a distance of 20 mm from the bottom wall of the test section upstream the testing model. By assuming a steady and incompressible flow, the total (stagnation), p_t, and static pressure, p_{st}, are measured with the pitot-static tube instrument. The speed of the airflow, V, is derived from those pressure, the isentropic exponent of air, k, the static- and total temperature, T_{st} T_t, the gas constant, R, and Mach number [80, 81]:

$$Ma = \sqrt{\frac{2}{k-1}\left[\left(\frac{p_t}{p_{st}}\right)^{\frac{k-1}{k}} - 1\right]} \qquad \text{Equation 3.1}$$

$$T_{st} = \frac{T_t}{1 + \frac{k-1}{2} Ma^2} \qquad \text{Equation 3.2}$$

$$V = Ma\sqrt{k\,R\,T_{st}} \qquad \text{Equation 3.3}$$

Figure 3-3: Atomizers arrangement in the wind tunnel [82].

The section upstream of the converging section is comprised of three atomizers horizontally mounted in a 3D printed NACA airfoil (Figure 3-3), which recreate a cloud in

the testing chamber. Each atomizer (Figure 3-4) is connected to a source of nitrogen air and de-ionized water controlled by a mass flow controllers. De-ionized water is pure and should not contain any contamination decreasing the chances of having icing nuclei. To avoid freezing of the water lines when performing icing experiments, the water pipes are maintained at a temperature of above zero by the heating cables contouring them. The water-, P_w, and air-, P_A, pressure are varied to achieve the different, target cloud conditions.

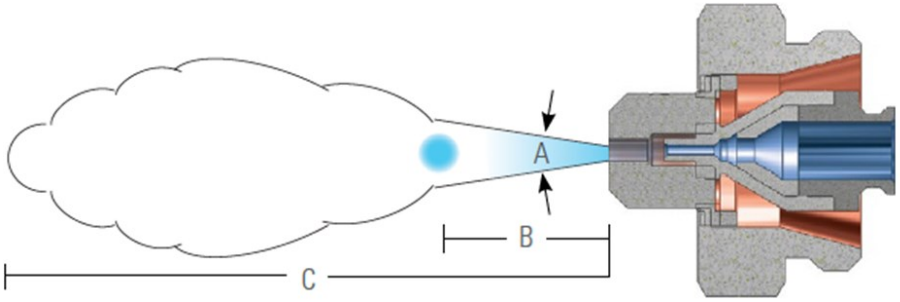

Spray Dimensions		
Spray Angle A (°)	B (in.)	C (ft.)
12 - 15	19 - 23-1/2	13 - 17-1/2

Figure 3-4: Pressure spray SUJ12A, internal spray and round spray [82].

The LWC is defined by the total mass of water content in all the liquid cloud droplets within a unit of volume of cloud [40] and can then be estimated for the testing conditions with the following equation; where K is a derived function depending on each spray configuration and V is the freestream airspeed at the test section [81]:

$$LWC = K\frac{\sqrt{P_w - P_a}}{V} \qquad \text{Equation 3.4}$$

The MVD defines the droplet size in terms of the volume of sprayed liquid [40] and by definition is the midpoint droplet size where half of the sprayed volume is made up of drops with diameter smaller than the median and half with larger than the median value. The nozzles are calibrated with particle image velocimetry (PIV) allowing to predict during testing the MVD by the water and air pressures [81].

The iCORE can mimic clouds with LWC from 0.2 to 1.5 g/m^3 and MVD values from 10 to

40 µm. Previous calibration, which results are shown in Figure 3-5, demonstrated that the iCORE testing capabilities satisfy the acceptance values of icing wind tunnels, which defines an uniform icing cloud as the area where the LWC does not vary from the centerline by more than ±20% [81]. A cloud uniformity can be obtained in the central part as shown in Figure 3-5 where in the vertical position between -10 to 5 mm the LWC values are converged between 0.5 to 0.7 g/m^3.

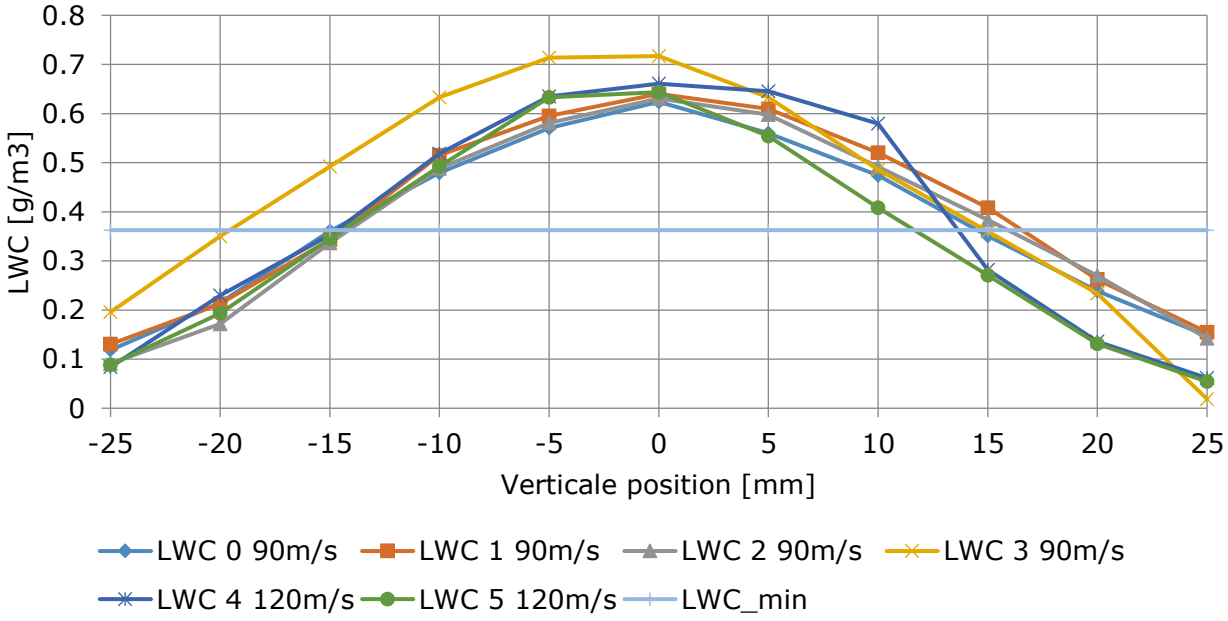

Figure 3-5: LWC measurements at different vertical positions in the iCORE icing wind tunnel — wind speed of 90 and 120 m/s, 22 µm MVD [83].

The spray system of the iCORE was characterized by shadowgraphy and the results are shown in Figure 3-6 [78]. The LWC is regulated by the pressure of the three mass flow controllers and the nitrogen pressure since it cannot be measured during a test; thus, the LWC can vary from 0 to 50 cm^3/min. The MVD is more stable in the middle of the test section rather than near the walls.

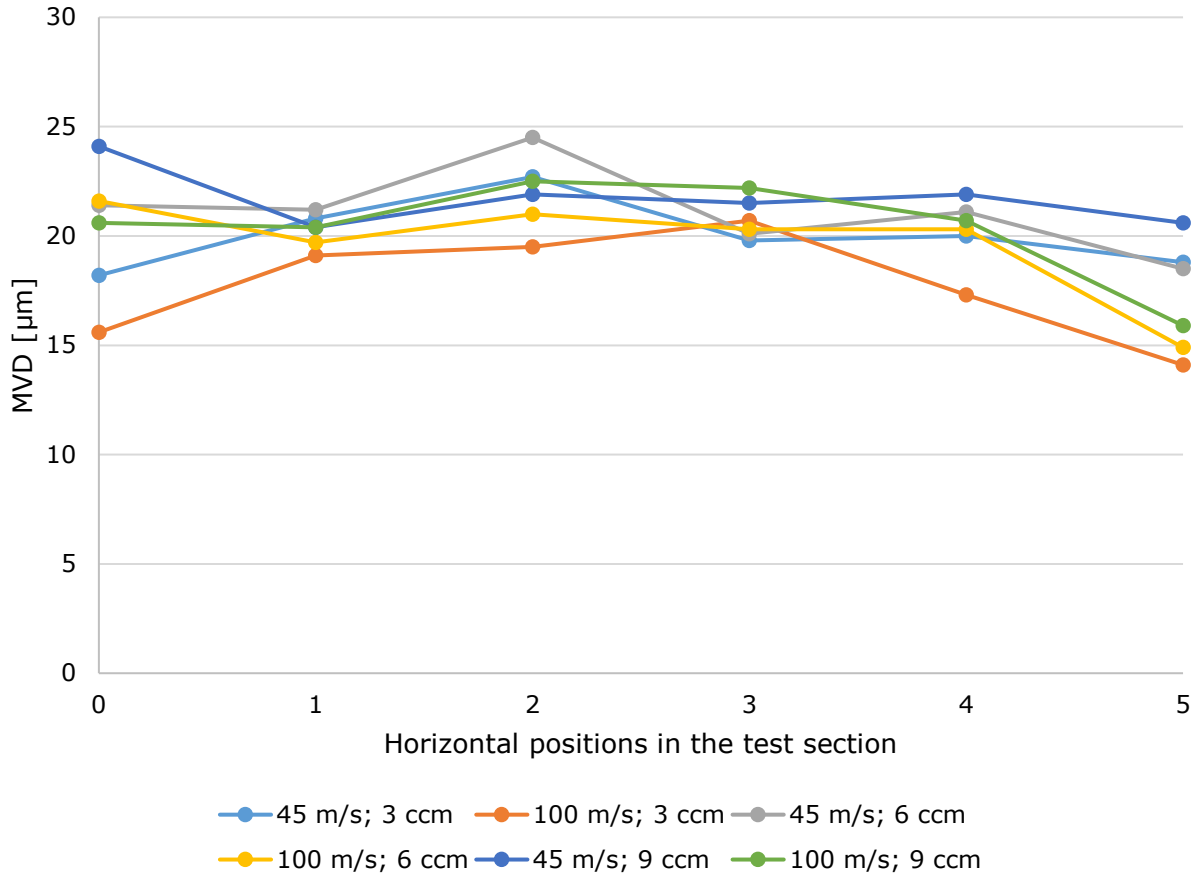

Figure 3-6: MVD measurements at different horizontal positions in the test section of the iCORE — wind speed of 45 and 145 m/s at ambient temperature [78].

In section 2.6, the Mode I test developed by previous researchers is mentioned along with the fundamentals of their testing approach. Different components were studied in isolation from the whole system to validate its performance and seek optimal application.

3.2 Mode I Test Design

The test rig design is based on the blister test [66], which consists of a pressurised system (Figure 3-7), data acquisition, and a sample with a 30 mm diameter and an inner hole of 4 mm in diameter. The dimension of the sample was a requirement from the client. It is based on the concept that ice is accreted on one surface of the sample in the icing wind tunnel, and the required pressure needed to break the ice through the small orifice of the sample is the adhesion force.

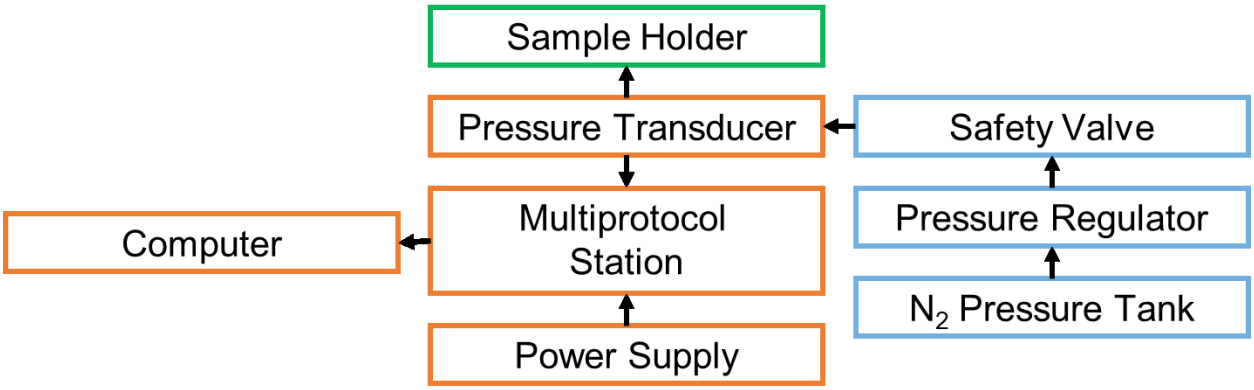

Figure 3-7: Mode I system diagram; the blue boxes represent the pressurized system, the orange represents the data acquisition system and the green is the Mode I test.

Vacuum pumps and vacuum generators can administer negative, or sub-atmospheric, pressure for a wide range of applications. As presented in Chapter 2.6.2, the Cranfield University Mode I test employs a vacuum force that is only required for holding the PTFE disk on the sample at the beginning of the experiment [38, 67]. The sample is glued on the sample holder. The vacuum is produced by removing gas molecules from a delimited volume, hence reducing the particle density. The vacuum system that employs the gas-capture principle requires periodic maintenance since it becomes saturated due to stored gas over a certain period.

3.2.1 Sample Holder Mechanism Action and Design Evolution

In order to avoid the need to use a small PTFE disk, different approaches where studied to find the best solution. The goal is to diminish the preparation and event time by eliminating the step of cutting and installing of small disks. Initially, the objective was to employ a catheter as used in the medical field. The contacted suppliers were unable to produce a catheter able to withstand a temperature of -50 degrees Celsius (°C) and a pressure range of 0-100 bar. Subsequently, companies that produce inflating bags were contacted. However, a solution which would inflate through a 4 mm diameter was needed, which was unrealistic for the contacted companies to supply. Providers of pneumatic booting system were then contacted. However, they could not provide simply one part of their equipment since they only sold the unit as a whole. Going back to the basics, a thin elastomer (i.e., piece of rubber balloon) were tested to study their behavior under pressure and cold conditions. First, three balloons where inflated and left in a freezer at -35 °C. No change was observed through two days, and therefore they withstood icing conditions without cracking or deteriorating. Pressure tests were performed on the balloons to see if they could inflate through a small orifice of 4 mm in diameter using an air source with a maximum pressure of 10 bar. It was found that the best setup was obtained by using the small tube with an outside diameter of 3 mm.

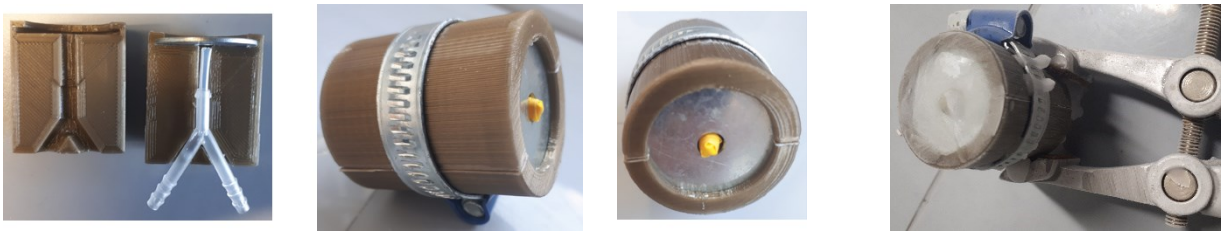

(a) Pohotograph of 3D printed prototype.

(b) Side view.

(c) Front view.

(d) Prototype setup with ice.

Figure 3-8: 3D printed prototype installed with the sample, pneumatic tubes and thin elastomer.

A prototype was designed and 3D printed in order to perform the first tests with ice on the samples as shown in Figure 3-8. This study was performed to validate the functioning of using a thin elastomer to initiate the crack instead of using a PTFE disk. A maximum pressure of 10 bar was used instead of the needed 100 bar; therefore, the thickness of the ice was less than the required amount for the Mode I test calculations. Nevertheless, this temporary setup allowed for quick tests and observations of the thin elastomer material placed behind the sample. As expected, after each test, the thin elastomer needed to be replaced since the pressure shock would rupture it. It corresponded perfectly to the two roles the PTFE disk had for the other laboratory Mode I test which are to impede ice accretion in the pneumatic tubes and to act as a crack initiator. These tests confirmed the functionality of the design concept by having the edges of the sample covered by the sample holder and implementing a thin elastomer instead of PTFE disk with the vacuum system.

3.2.2 Sample Holder Experimental Rig Design

The sample holder prototype was further optimized in SolidWorks 2016 in order to prepare the technical drawings for the technicians in the machine shop of Airbus. Two reasons explain why only one sample can be tested at the time. Firstly, when inserting new objects into the testing chamber, it is important to ensure that there would not be an airflow blockage. Secondly, when the ice accretes on the sample, depending on the conditions, the ice might grow around the sample and on the sample holder and stands. If there would be two sample holders, one beside the other, the ice might grow in a way where it would be connected to both samples and the test would be invalid. Therefore, a certain distance (that can be known from trial-and-error only) must be kept between each sample to avoid this occurrence. The final design of the Mode I test is shown in Figure 3-9 and Figure 3-10.

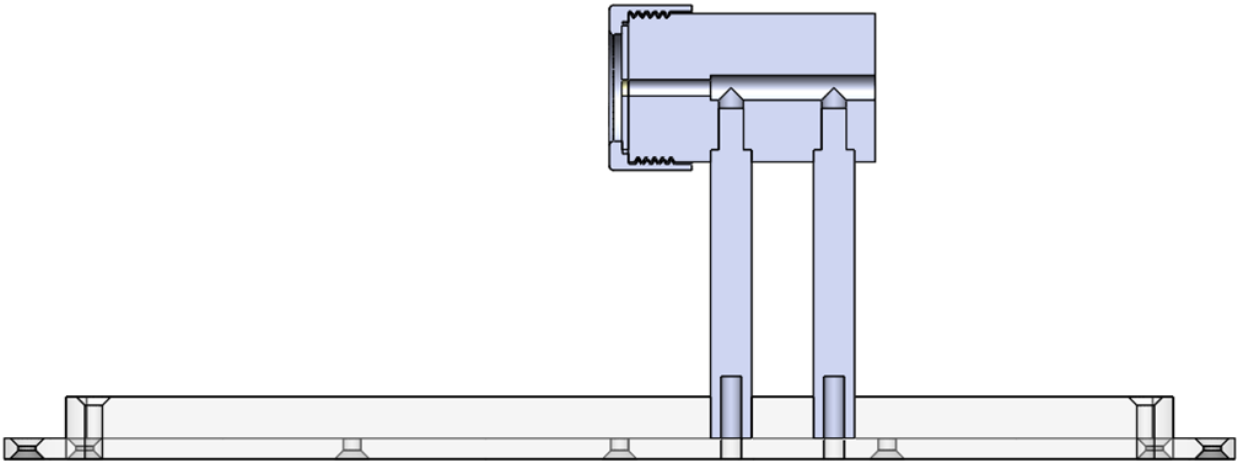

Figure 3-9: CAD drawing of the cross-section view of final design of Mode I test.

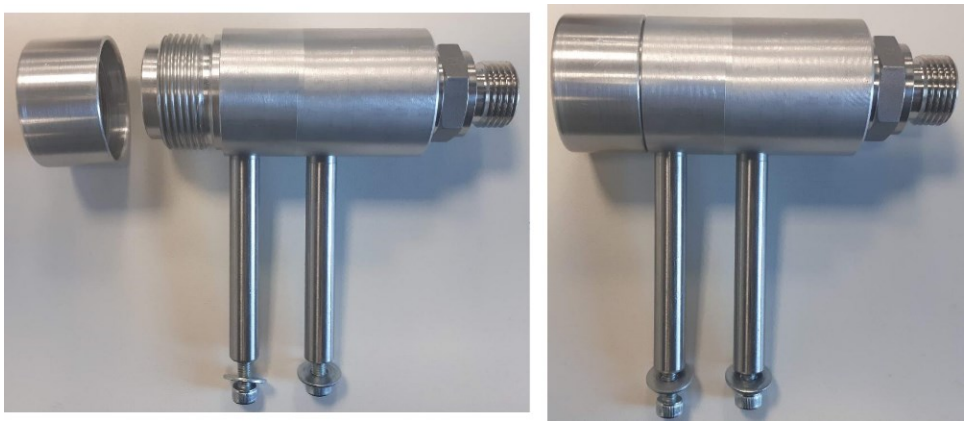

Figure 3-10: Side view of Mode I test sample holder with fitting for pressurized system connection.

As shown in Figure 3-11, the three main parts are: the sample holder, the sample, and the holding cap. By having a hollow cap, there is no need to glue the sample on the sample holder, which eliminates preparation steps. Also, when the test campaign is completed, the sample can be easily removed without any treatment or tools. While the testing time is decreased by installing the sample by adjusting the holding cap, further testing should be done to investigate the effect of the geometry and dimensions (thickness and width) of the lip from the holding cap.

Figure 3-11: Sample holder's components.

As a means of stability when performing experiments at high speeds, the stands are secure in the sample holder by interference fitting. The base of the stands goes half way the bottom test section wall and then there are screws coming from the outside of the test section into the stands. On the right side of the sample holder, there is a fitting that is screwed in. This is the connection to the pressurized system, and the fitting can withstand 300 bar of pressure.

Further improvement of the design of the sample holder can be achieved by changing the material of the holding cap. Since there is a lip of the holding cap superimposing the tested substrate, it could affect the adhesion of the ice result. Ideally, the strength of ice adhesion on the lip of the holding cap should be weaker than the one ice adhesion from the substrate to insure the result obtain is coming from the substrate. Nevertheless, as the Mode I test is a comparative test, the results obtained do not have a representative value when taken in absolute and therefore one can still characterize different samples by ranking their icephobicity results even though there is the lip of the holding cap present. This is a constant factor and it is expected to behave the same on each experiment. However, this test rig can only measure ice adhesion strengths of surfaces that are higher of the adhesion strength of the ice from the side of the lips of the sample cap.

3.2.3 Pressurized Gas System

The pressurized system is required to input a controlled force in order to break the ice accreted on the sample while performing experiments. Due to the high pressure of 100 bar required for the Mode I test, the gas cylinder must be higher. The different components of this subsystem are described in this section.

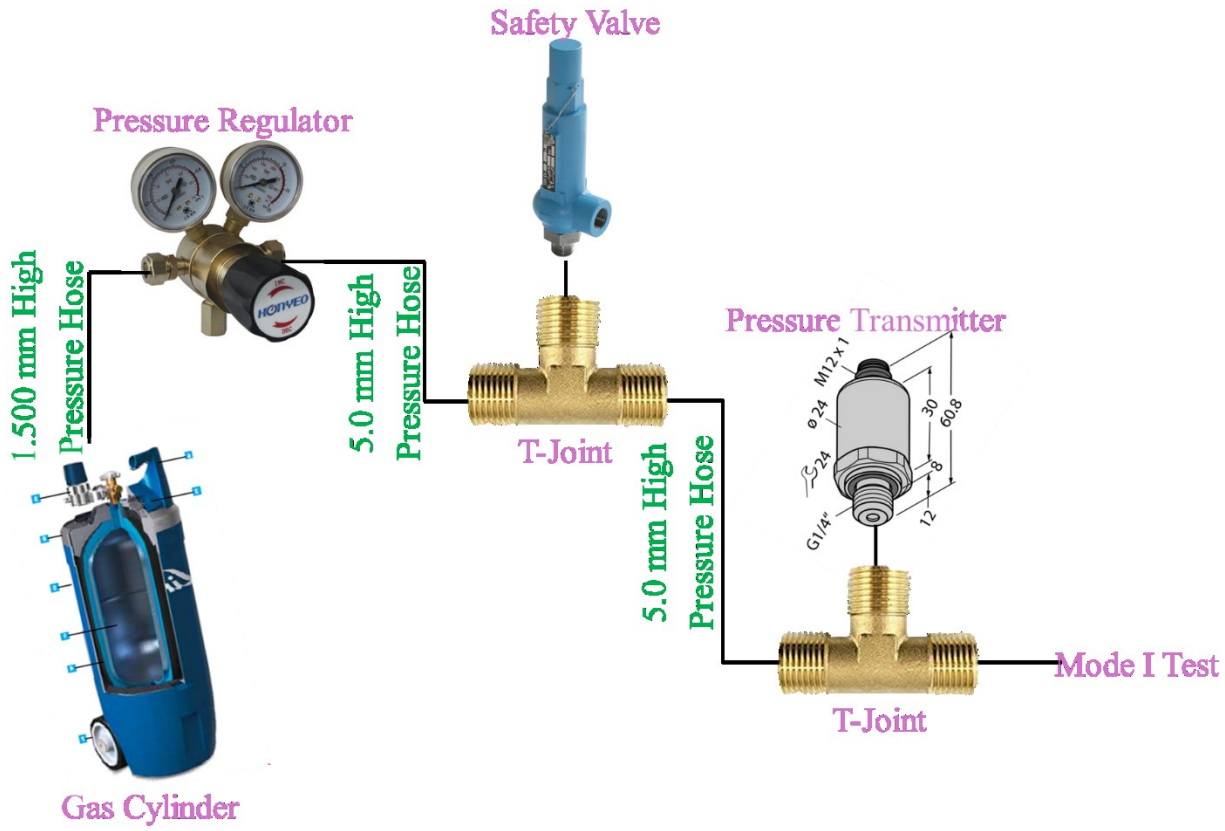

Figure 3-12: Pressurized system diagram.

As seen in Figure 3-12, the gas cylinder is the supply of nitrogen air. The cylinder used for the nitrogen gas is a *Genie*® from *Linde*, that can withstand up to 300 bar of pressure and has a capacity of 20 liters (L) (5,28m^3 for nitrogen gas) [84]. A pressure regulator with an input of 300 bar with a maximum output pressure of 100 bar is then connected to the cylinder head. A second control stage installed on the first pressure regulator is also of

300 bar with maximum pressure of 100 bar. The safety valve can handle up to 130 bar, but is regulated to 100 bar. As in many systems, a failure often occurs at the weakest point; therefore, all the hoses and fittings can withstands 300 bar of pressure to ensure a safe environment for the users.

A pressurized cylinder can cause serious injuries leading to death if not properly handled. To diminish the operating risk of the pressurized system, a cylinder *Genie*® from *Linde* was selected since it has its own stand, and in the event that the cylinder falls down, the handles are protecting the pressure gages to avoid any dramatic consequences. Nevertheless, even though it is a very safe design, it should always be handled and stored with care. In case of a fire emergency, fireman should be aware of the presence of a pressurized bottle. A sign was installed in the door of the laboratory to indicate the presence of a 20 kg gas cylinder with nitrogen.

3.2.4 Data Acquisition System

The outputs of the Mode I tests are the critical pressure, the type of failure (adhesive, cohesive or mixed) and the thickness of the accreted ice. These are the variables required to calculate the tensile strength of ice. The ice thickness is measured by taking a picture of the ice accreted on the sample while still in the test section and obtaining the approximate thickness by post-processing the image with the image processing program Fiji from ImageJ [85]. The type of failure is visually determined. The data acquisition system is essential to obtain the critical pressure of the ice failure. As seen in FigFigure 3-13, the data acquisition system comprises a power supply, a multiprotocol station, the pressure sensor and the computer.

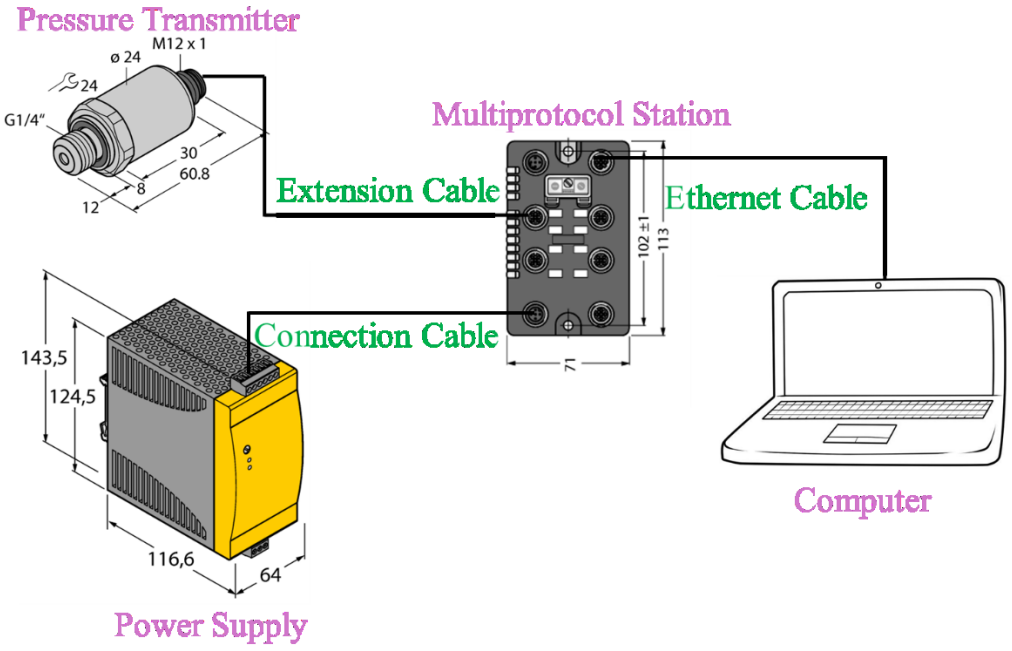

Figure 3-13: Data acquisition system diagram.

The main component of this subsystem is the pressure sensor. The pressure sensor is a device that measures an area which has a force being applied to it by measuring the deflection change. Different types of sensing devices use a strain gauge or diaphragm,

which creates a signal that is sent to the multiprotocol to be processed.

The different aspects to correctly measure and interpret pressure are summarized here. In order to select a proper sensing instrument, the media must be known. For the Mode I test, it was previously establish that compressed nitrogen air would be used. Since the sensor is not inside the test section of the icing wind tunnel, the pressure sensor is not exposed to a corrosive environment. The temperature of the media (nitrogen air) and the ambient temperature of the laboratory should remain constant. Therefore, there should not be any fluctuation in the obtained results. The sensor is placed after the safety valve to avoid any damages from pressure bursts. Pressure spikes can also be avoided by always opening the pressure valves slowly. Electrical noises can alter the representation of pressure and can be caused by high frequency devices near the sensor, or the wiring for the sensor. Therefore, the data acquisition system is isolated from the rest of the iCORE devices by installing it on its own stands.

Figure 3-14: Pressure control unit manufactured and assembled by Linde Group.

The different types of pressure sensors are pressure transducer, transmitter, switch and gauge. Pressure gauges are part of the pressurized system as shown in Figure 3-14, and they allow a visual representation of the applied force. A pressure switch offers an electrical signal when a certain predefined condition is met. Pressure transducers and transmitters are used for measuring continuous pressure and typically do not offer any

type of visual display. The main difference between the two is that they send different signals; a transmitter sends the signals in milliamps, and the transducer sends a signal in volt or millivolt. For the Mode I test, the pressure output is required and thus the pressure gauge and switch do not correspond to the requirements. Therefore, a pressure transducer was chosen for this test. This permitted a device that can withstand a pressure range of 0-160 bar and have a G¼ '' male thread, which was required for the pressurized system. The specs of the chosen sensor are in the Appendix I. The accuracy is ±0.3 % Full scale, Best Fit Straight Line (FS BSL) which translates to 160±0.48 bar.

The compact multiprotocol (Appendix K) is module is required to have an Ethernet connection to achieve the fastest transmission rate of 10 megabits per seconds (Mbps). The advantage of this multiprotocol is that it only required a supply voltage of 24VDC. Such a power supply (Appendix L) can be directly connected to a wall plug and does not require installation to the main electrical relay from an electrician.

The relevant specs of the Multiprotocol TBEN-S2-4I are [86]:

- → Integrated Ethernet switch
- → Shock and vibration tested
- → 4 Analog inputs (Thermocouples, Voltage, Current, Resistance or RTD Input)
- → Operating temperature: -40 °C to +70 °C
- → Cyclic process data transfer in typical 2.3 ms

3.2.5 Experimental Procedure

The goal of doing Mode I tests is to obtain the tensile strength required to shed off the accreted ice on a surface inside the icing wind tunnel. The development of the Mode I test of this thesis is based on the Mode I test used in Cranfield University developed by Hammond [66]. In this test, pressurized air is forced through a small aperture which is covered by a thin elastomer. The pressurized air initiates a crack grow in the ice or at the ice-substrate interface. When a complete failure (i.e., when the ice detaches from the surface) occurs, the critical pressure is obtained and used to obtain the ice adhesion strength through derived calculations.

The sample to be studied is installed in the sample holder by inserting a thin elastomer in order to cover the small aperture of the pneumatic system, centering the sample on the sample holder, and then screwing on the cap. Improperly collecting and handling of the samples can lead to procedural errors since the presence of impurities on the surface can affect the wettability and ice adhesion results. Thereby, gloves should we wear to avoid contamination from the natural oils from the skin and dirt to the sample to be studied. The icing wind tunnel is set to the desired conditions and once the airspeed and total air temperature are stabilized, the spray system was turned on until the ice thickness became approximately 15 mm from visual estimation. The spray system was turned off before starting to manipulate the Mode I test system. The data acquisition of the pressurized system was turned on, and the pressurized system was slowly opened and was left open until the ice shredded off. The type of fracture (adhesive, cohesive, mixed) and the graph (Figure 3-15) obtained from the data acquisition system was saved. For each testing condition and for each sample, the test is repeated as a minimum three times for each data point in order have a better average result.

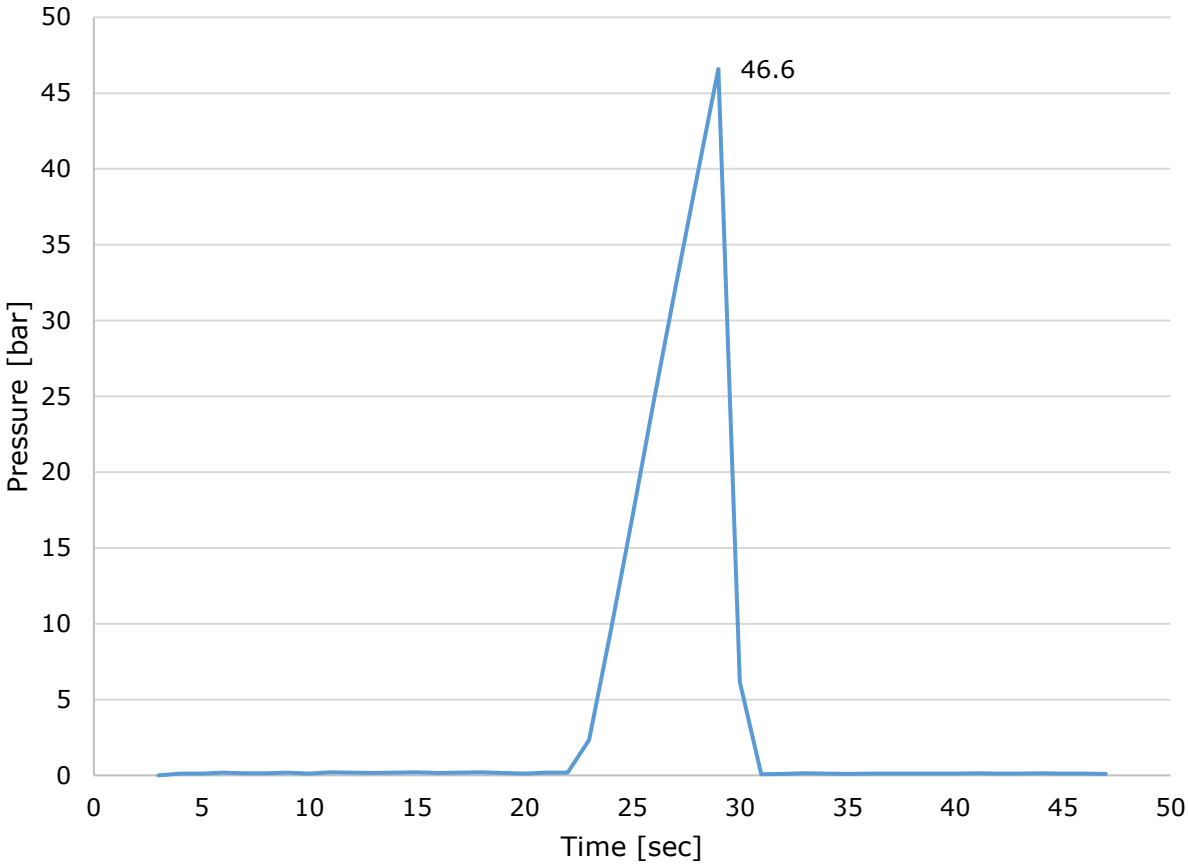

Figure 3-15: Pressure versus time graph obtained from IWT testing — Al2024 TSA sample in glaze ice conditions.

Figure 3-15 shows the raw data obtained where the pressure is the force applied by the pneumatic system, it can be observed that the pressure increases at a constant rate until it reaches a maximum. When the ice is covering the center hole of the tested sample it creates a closed-system. The pressure builds up until a maximum where the ice strength is weaker than the force applied by the pressure inputted; as a consequence, the ice breaks off creating an open-system, which explains the sudden pressure drop illustrated in the graph.

The critical pressure is an electric signal, *Volt*, in mV obtained by the Modbus Poll software [87] and is translated into pressure magnitude through the equation below. The pressure range the transducer can withstand is 0 to 160 bar which it is equivalent to 0 to 100 mV [88].

$$\sigma_c = Volt\ [mV] * \frac{1\ [V]}{1000\ [mV]} * 16[{}^{bar}/_{V}] \qquad \text{Equation 3.5}$$

3.3 Materials

The main goal of this thesis was to develop a Mode I test rig to set-up in the iCORE facilities. In addition to the already installed bending cantilever test in the iCORE, the Mode I test allows having more than one way of performing ice tests campaigns as mean to cross-validate the ice adhesion results for screening of different surfaces. Surfaces that were previously studied in the bending cantilever test were prepared and investigated under the Mode I Test. The goal was to validate the functioning of the new developed test equipment. Characterizing the surfaces also allows correlating the ice adhesion results obtained with the wetting behavior and to the CAT results.

3.3.1 Sample Preparation

As shown in Figure 3-16, the dimensions of the test samples were required to be 30 mm in diameter cylinders with an inner hole of 4 mm and a thickness of 1.6 mm, and they are directly mounted on the holder where the pneumatic system is centered in the small cavity. From a metal sheet with a thickness of 1.6 mm, squares of 33x33 mm were cut. Then an inner hole was made by drilling an opening with a diameter of 4 mm. With a lathe machine, the small squares were shaped to perfect circles of 30 mm outer diameter.

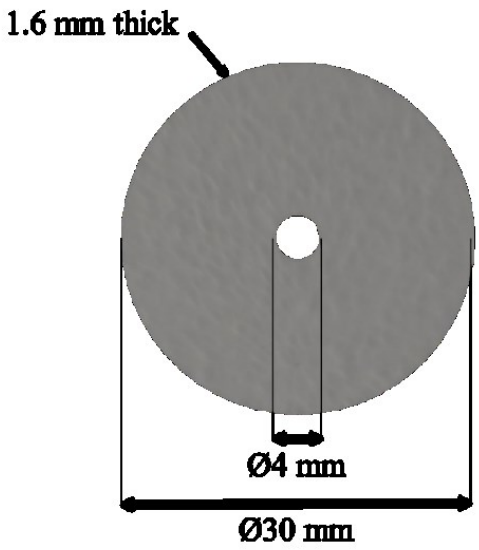

Figure 3-16: Dimensions of Mode I test samples .

The material used as a substrate was Al-2024 (Figure 3-17). Aluminum was selected since the same aluminium samples were tested previously with the bending cantilever test and it is widely used in the literature [47, 89, 17, 23, 90, 38]. The three different treatments studied were polished Tartaric Sulphuric Acid (TSA) (Appendix N), polished TSA and MecaSurf [91] (Appendix O).

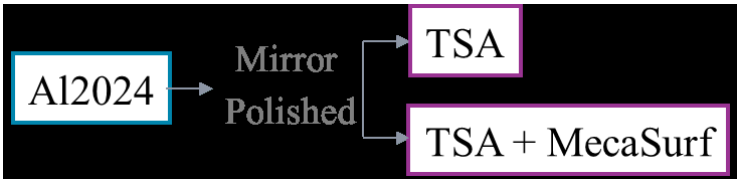

Figure 3-17: Material and surface techniques used for sample preparation of Mode I test.

Roughly, 30 samples were machined for the reference metal material and those that were not treated nor tested are kept for the next testing campaign. Three samples were prepared for each treatment to allow having one sample for characterization and two others for testing. It also allows having a selection for the best quality sample after applying the treatment.

3.3.2 Sample Characterisation

Prior characterisation, all samples were cleaned in the ultrasonic bath (Figure 3-18) for 5 min in distilled water followed by 5 min in alcohol. Then, the samples were dried with nitrogen (N_2) air. This will allow to remove all the contamination that might be present on the surface due to transport and manipulation.

Figure 3-18: SONOREX UltraSonic bath [92].

The wettability of each sample was determined by measuring the points of intersection of the image (three-phase contact points) of a sessile drop with a volume of 10 µl taken by the KRÜSS [93] drop shape analyser in a conditioned room with an ambient temperature of 23 °C with a relative humidity of 44% (Figure 3-19). The volume of the droplet was chosen according the recommendations of the manufacturer.

Figure 3-19: KRÜSS Drop shape analyser – DSA25 [93].

In order to analyze the wettability, the CA, CAH and ROA, each data point was repeated three times on each sample at different locations to achieve a better average result. An example of CA measurements for the case of an hydrophilic (left) and hydrophobic (right) aluminum cases are presented in Figure 3-20.

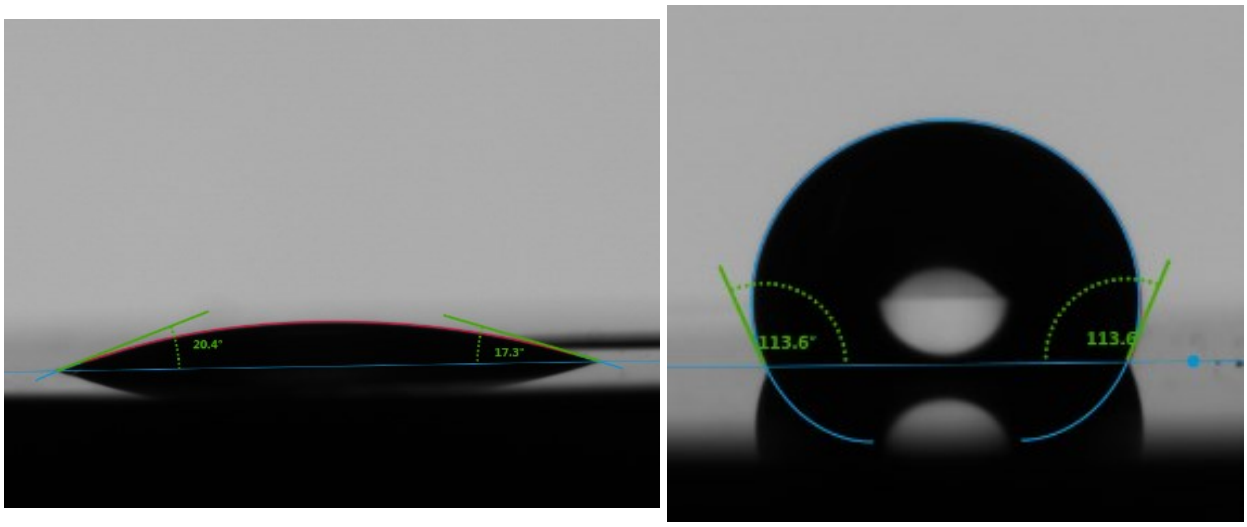

Figure 3-20: Sessile droplet (10 µl) on Al2024 TSA (on the left) Al2024 TSA with MecaSurf (on the right) from contact angles measurements.

Surface roughness enhances ice adhesion. Therefore, it is important to have clean and impurity-free surfaces in order to reduce the strength of ice adhesion thereon. As a mean to relate the wettability properties of a surface to its behavior in the icing wind tunnel, the surface roughness is measured with the Hommel-Etamic T8000 R (Figure 3-21). With an automated program, the measuring instrument was set to read the profile over a length of 2 cm in one log. Three measurements were taken and an average was then obtained for each sample for the surface properties (surface profile, R_a, R_z).

Figure 3-21: HOMMEL-ETAMIC T8000 R120-400E Roughness and contour measurement [94].

Chapter 4 - Results & Discussion

The results obtained from the sample characterisation and the icing wind tunnel tests are presented and analyzed in this section. The data for the surface repellency, droplet mobility and surface roughness is correlated with the ice adhesion results.

4.1 Sample Characterization Results

4.1.1 Surface Repellency and Mobility

The CA, CAH and ROA for the three different samples were obtained to analyze their surface wettability. The summary of the measured contact angles is presented along their water repelling characteristics in Table 4-1. A droplet that impacts a solid surface and remains in its spherical shape, or easily rolls off when the surface is tilted, tends to determine if the surface has hydrophobic characteristics and to what extent. Thus, as previously mentioned, the desired wettability features for a superhydrophobic surface are a high CA (>160°) and a ROA as small as possible (best if < 10°) [17, 23, 53]. A hydrophobic surface exhibits and CA above 90° while the CA of a hydrophilic surface is below 90°. Superhydrophobic surfaces are in Cassie-Baxter state, which suggest that air is captured in the cavities of the surface between the surface and droplet. On the other hand, surfaces with high CAH have lower droplet mobility since the droplets will sit deeper in the surface texture and are in between Cassie-Baxter and Wenzel wetting state [90].

Table 4-1: Summary of contact angle measurements of Al2024 samples.

Sample			Size	CA	ROA	CAH	Wetting property
Test	Texture	Coating	[mm]	[°]	[°]	[°]	
Mode I	Ref	-	ø30x1.6	104	90	33	HB
Mode I	TSA	-	ø30x1.6	20	87	27	HL
Bending	TSA	-	125x13x1.6	59	90	-	HL
Mode I	TSA	MecaSurf	ø30x1.6	97	89	31	HB
Bending	TSA	EpiSurf	125x13x1.6	122	90	-	HB

TSA: Tartaric Sulphur Acid anodizing to enhance the attraction to liquid and improve the adhesion with the MecaSurf
CA: Static contact angle
ROA: Roll-off-angle
CAH: Contact angle hysteresis
SH: Superhydrophobic
HB: Hydrophobic
HL: Hydrophilic
Ref: Reference

The roll-off-angle for the aluminium samples is approximately 90°. The reference sample for Al2024 has an average CA of 104° and when it undergoes TSA anodizing, the surface becomes hydrophilic and thereby the CA decreases to 20°. The TSA treatment enhances the attraction to another liquid and improves the adhesion with the MecaSurf. The MecaSurf on the anodized aluminium increases the CA to 97°.

The contact angles of the samples for the bending cantilever test previously taken are also summarized in Table 4-1. The samples for this test have a rectangular shape of 125x13x1.6 mm. The characteristics for the Al2024 sample with TSA anodizing and EpiSurf, or MecaSurf, are similar for the samples of both tests. On the other hand, the aluminium sample treated with TSA and MecaSurf has a high ROA leading to a low mobility of the droplet.

Table 4-2: Wetting characteristics of aluminium samples from values presented in literature.

Sample		Size	CA	ROA	CAH	Ref.
Substrate	**Description**	**[mm]**	**[°]**	**[°]**	**[°]**	
Al6061	Mirror-polished	32x50	57.3±2.8	-	~50	[62]
Aluminium	Polished	340x30	~66	-	~60	[57]
Al6061	Polished using 1 µm diamond suspension	25x75x1	103.5±1.5	-	43.8±3.5	[69]
Al6061	Sandblasted with medium grit	25x75x1	38.1±1.5	-	26.7±1	[69]
Al6061	Sandblasted with a coarse grit	25x75x1	86.8±4	-	54.7±2.5	[69]
Aluminium	Etched - superhydrophobic	-	158.5±2.2	7.5±1.2	-	[70]
Aluminium	Etched - hydrophobic	-	126.0±1.5	-	-	[70]
Aluminium	Etched - hydrophilic	-	45.2±1.8	-	-	[70]
Al6061	Etching	-	-	-	64±2	[48]

CA: Static contact angle
ROA: Roll-off-angle
CAH: Contact angle hysteresis
Ref: Reference

According to literature (Table 4-2), high CAH has been reported which signifies a poor drop mobility [62, 69]. For a mirror polished aluminium, categorized as reference sample in this thesis, the measure CA was 104° which is in line with was founded by Fillion et al. for an aluminum polished using a 1 µm diamond suspension [69].

4.1.2 Surface Roughness

The wetting behavior is affected by the surface roughness [55]. The surface roughness is the measure of the deviations in the normal direction of the surface, and the measurements were done according to ISO4287 (Appendix Q). The arithmetical mean deviation of the assessed profile, R_a, and the maximum height of profile, R_z, were taken and are shown in Table 4-3. The surface roughness can mechanically influence the ice adhesion since the water droplets can slide into the asperities and become interlock as freezing which means that a higher force will be required to detach the ice from the surface [89, 46]. Different surface roughness can be obtained by employing different methods — sand blasting, etching, or coating applications. As an attempt to correlate the

sample characteristic to its ice properties, the surface roughness is measured. This allows to later establish a prediction factor, if any, to determine if a sample will be promising under the icing wind tunnel tests by looking at its contact angles and surface roughness.

Table 4-3: Summary of surface roughness measurements of Mode I test and bending cantilever test samples.

Sample			Size	R_a	R_z
Substrate	**Texture**	**Coating**	**[mm]**	**[µm]**	**[µm]**
Al2024	Ref	-	ø30x1.6	0.61±0.02	5.36±0.23
Al2024	TSA	-	ø30x1.6	0.09±0.01	1.53±0.94
Al2024	TSA	MecaSurf	125x13x1.6	0.16±0.04	1.95±0.47

TSA: Tartaric Sulphur Acid anodizing to enhance the attraction to liquid and improve the adhesion with the MecaSurf
Ref: Reference
Ra: Arithmetical mean deviation of the assessed profile
Rz: Maximum height of profile

The reference Al2024 has a rougher surface compared with the two other cases that have TSA as seen in Table 4-3. The R_z value is the difference between the tallest peak and the deepest valley. Higher R_z values suggest a poor droplet mobility since droplets will have a tendency to impinging on the high valleys.

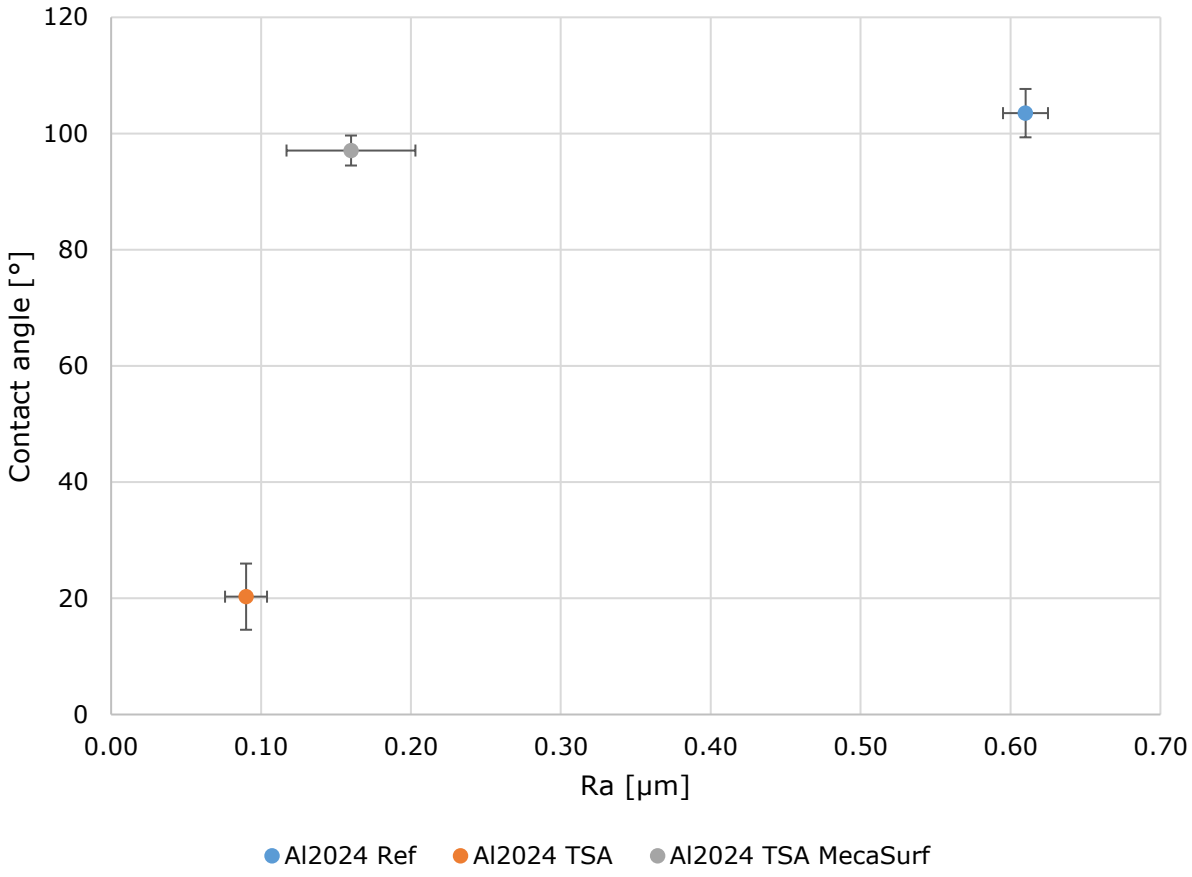

Figure 4-1: Surface roughness vs contact angle of Mode I test samples.

The influence of surface roughness on the wettability can be observed from Figure 4-1 where the measured CA are plotted against their respective surface roughness. The MecaSurf coating allow to reach a higher CA without affecting the surface roughness significantly. On the other hand, Figure 4-2 shows that for all cases the CAH was comparable. A lower CAH was expected for the Al2024 TSA MecaSurf compared with the reference case. This could be explained by the fact that the MecaSurf was poorly applied, or by a poor surface polishing before applying the coating. The large standard deviation in the case of Al2024 TSA could be to defects present on the surface. According to the literature, a higher surface roughness increases the ice adhesion strength [46, 95].

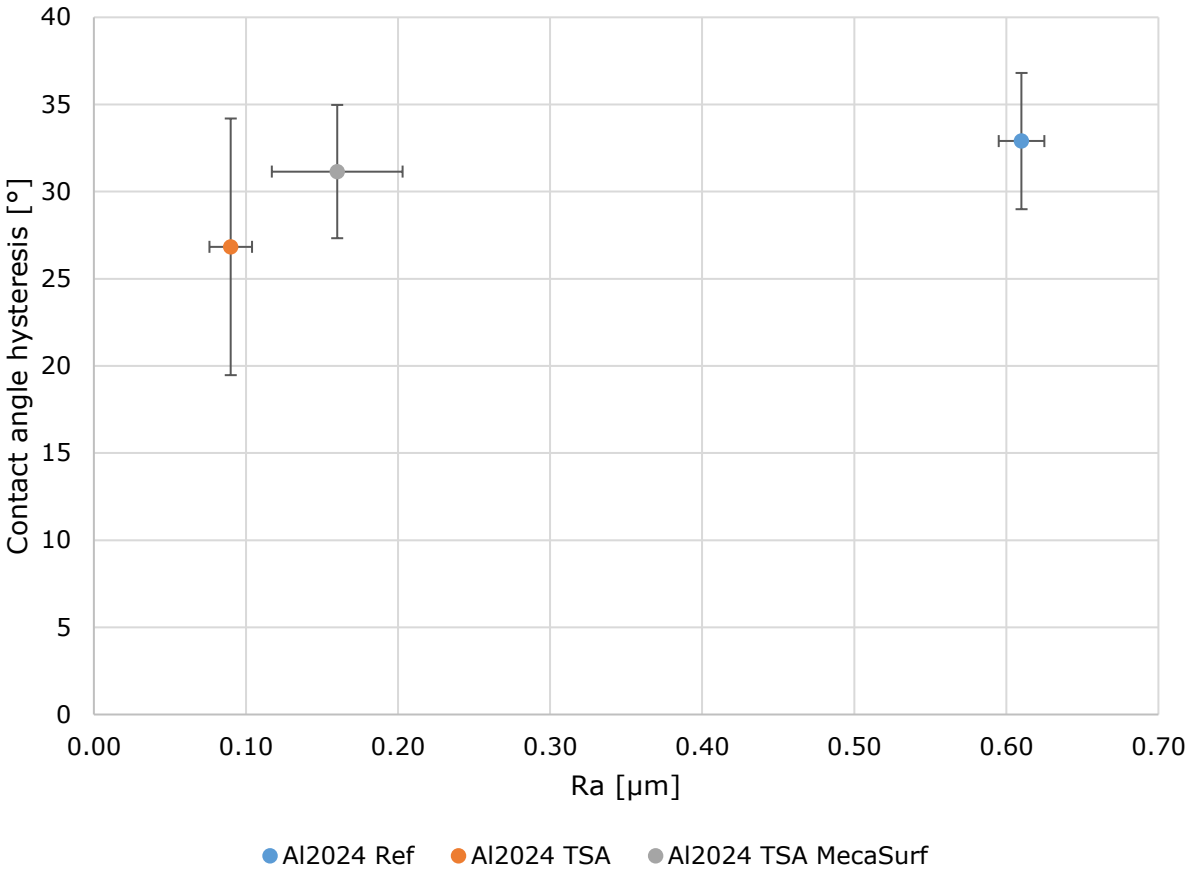

Figure 4-2: Surface roughness vs contact angle hysteresis of Mode I test samples.

4.2 Icing Wind Tunnel Tests

The primary goal of performing ice adhesion test was to validate the overall functioning of the Mode I test developed in this thesis. The ice adhesion strength measured with the Mode I test are presented for two samples in two different icing conditions (glaze and rime ice conditions). Additionally, the ice adhesion strength for similar samples previously measured with the bending cantilever test are presented and compared with those found with the Mode I test. An analysis of the correlation with the ice adhesion strength and wettability behavior is presented.

4.2.1 Testing the Functionality of Mode I Test Sample Holder

The sample holder was tested in the icing wind tunnel to study the overall functionality. Various test runs were performed in rime and glaze ice conditions without activating the pressurized system. Stability of the stands were observed in addition to the ice shape created. The sample holder was stable, and no abnormalities were observed. The ice shapes grown in both conditions are shown in Figure 4-3 and corresponded to the expectations from the literature review [38, 67]. For the rime ice conditions, the ice was white and opaque with a granulated aspect, while the ice was transparent for the glaze ice conditions.

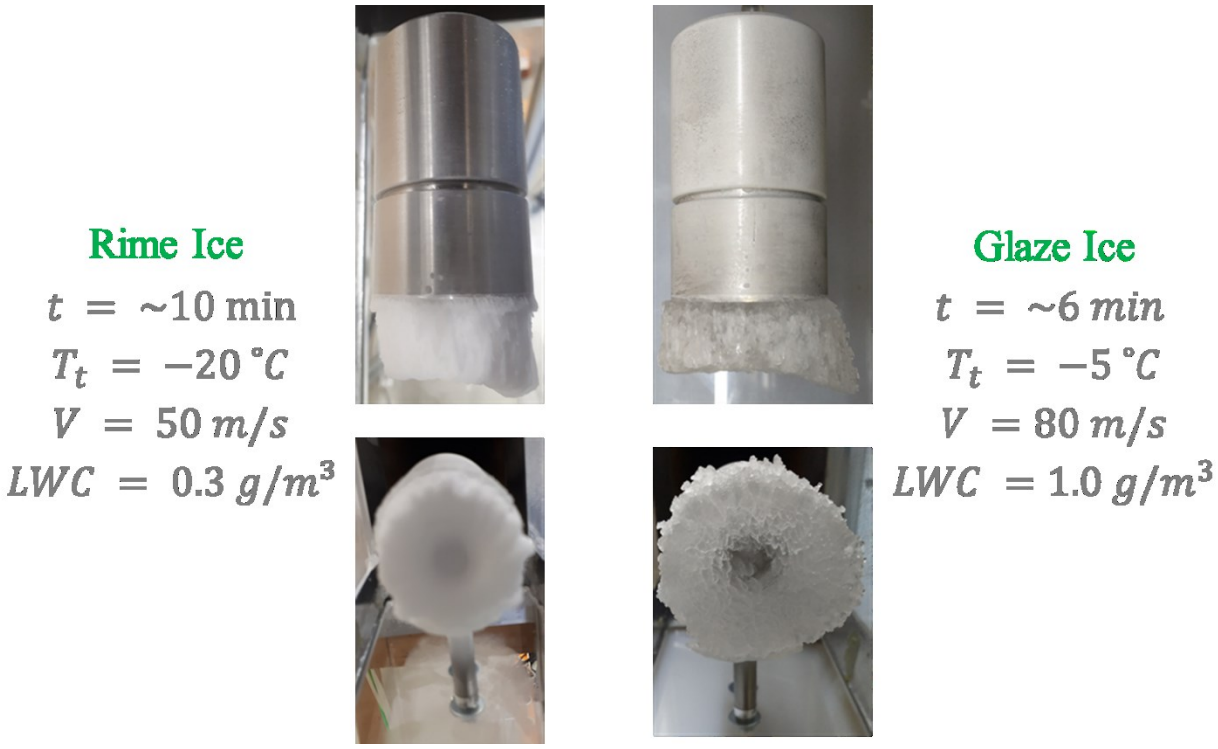

Figure 4-3: Testing of Mode I test rig in the iCORE.

The new design differs from the others Mode I test from the sample installation. At Cranfield University research laboratory, the sample holder, based on the test described by Andrews [63], is a cylinder with an outer diameter of 30mm, inner diameter of 4 mm and a length of 30 mm. The cylinders are screwed in transversal bars that are placed in the test section. With a test section of a cross area of 760x760 mm, they are equipped with pneumatic system for their Mode I test allowing to test eight samples [67, 38]. The samples tested in their facilities have outer diameter of 30 mm and inner diameter of 4 mm, with a 1.6 mm thickness. The samples are glued onto the cylinders with furniture glue.

The new developed Mode I test in the iCORE was successfully set up. Although the method of measuring the ice adhesion strength by applying a tensile force is already used in other research laboratories, this newly developed test rig is unique in the way the sample is secured and the mechanism the force is applied to break the ice. The iCORE

Mode I test avoid the complexity of having to glue each time the sample on the sample holder and to cut small PTFE disk to cover the pneumatic system, which also removes the need of having a vacuum system. In addition, to the screwing cap, there is a flexibility of using different thickness for the sample to be tested.

4.2.2 Results of Ice Adhesion Tests

The aim of ice adhesion testing was to validate the performance of the Mode I test rig developed and not to perform research on parameters affecting ice adhesion values. Two Al2024 samples with TSA anodizing and TSA with a surface treatment (EpiSurf or MecaSurf) were tested with the Mode I test (Figure 4-4) in order to compare the results of the bending cantilever tests (Figure 4-5). The samples were tested in two different icing conditions which parameters are presented in Table 4-4. The ice adhesion strength for both samples and each test are presented in Figure 4-4 and Figure 4-5 along the error distribution.

Table 4-4: Icing conditions (supercooled droplets) used during ice adhesion tests for this project.

Ice Type	Total Air Temperature (T_t)	Airspeed (V)	Liquid Water Content (LWC)	Mean Effective Droplet Diameter (MVD)
	[°C]	[m/s]	[g/m^3]	[µm]
Rime	-20	50	0.3	20
Glaze	-5	80	1.0	20

The trend from the Mode I tests result (Figure 4-4) was anticipated, the average tensile strength is higher for the Al2024 TSA sample than for the Al2024 TSA MecaSurf sample in both icing conditions. MecaSurf is a commercially available surface treatment that has the ability of reducing the surface tension of the substrate and consequently preventing substances from spreading on its surface. The contact area of the droplet with the surface for the Al2024 TSA sample is more than two times larger than the contact area of the droplet with the surface of the same sample with MecaSurf coating. As expected from the

hypothesis, having a small contact area signifies that the interlocking of the water into the surface is smaller, and thus when ice grows on the surface it requires a lower force to remove it.

When considering the effect of type of ice, it can be noticed when looking at Figure 4-4 that higher average ice adhesion values for glaze ice conditions when compared to rime ice.

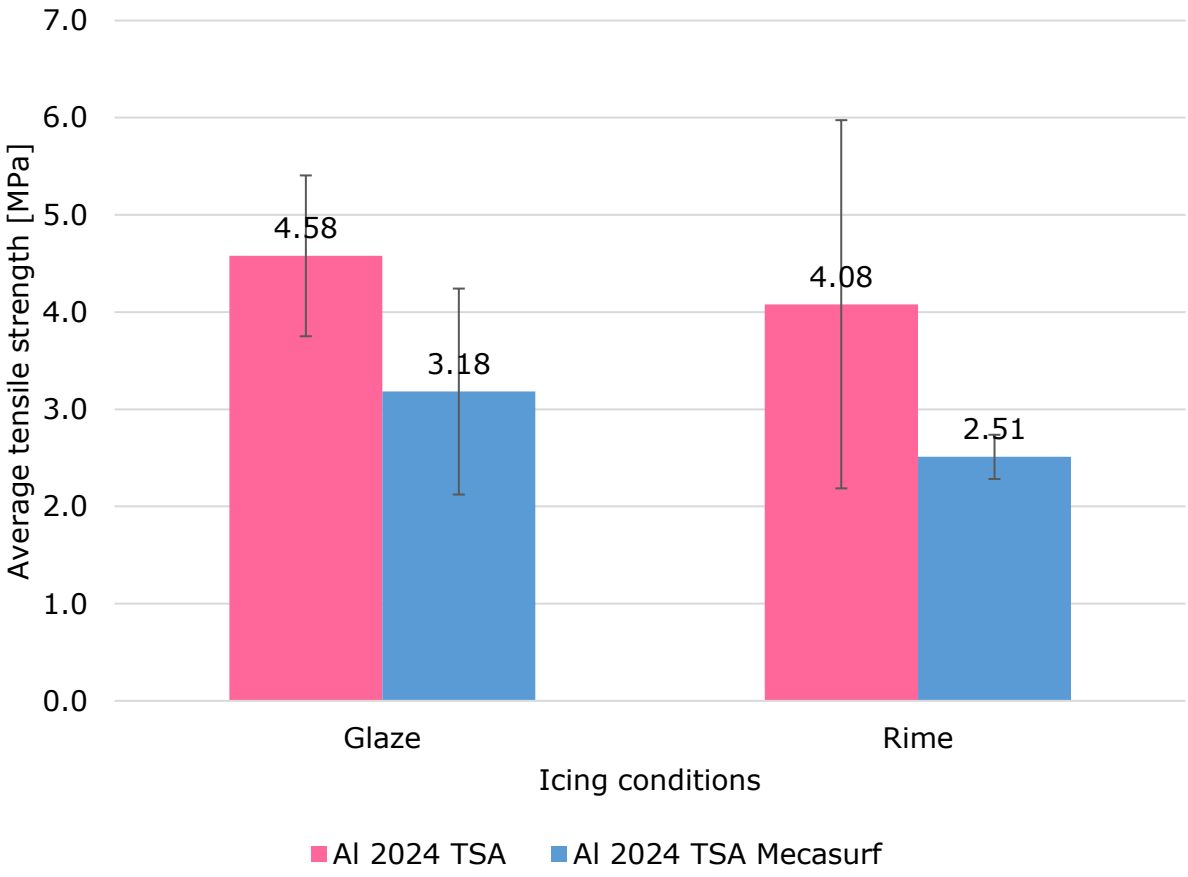

Figure 4-4: Results of Mode I test experiments in the icing wind tunnel with Al2024 TSA and Al2024 TSA MecaSurf.

The same behavior was observed with the results from the bending cantilever tests for only the rime ice conditions. However, an untypical trend was observed for the glaze ice conditions by noticing that a larger work was required to remove the ice from a substrate

that has the additional surface treatment. There are different reasons that could explain this unexpected behavior. One reason could be that the anti-spreading coatings are not eternally durable and it might have deteriorated between tests. Since there is not a test performed after the application of the coating, there is not a confirmation that it was properly applied throughout the whole sample's surface. The EpiSurf might not have properly adhered to the surface.

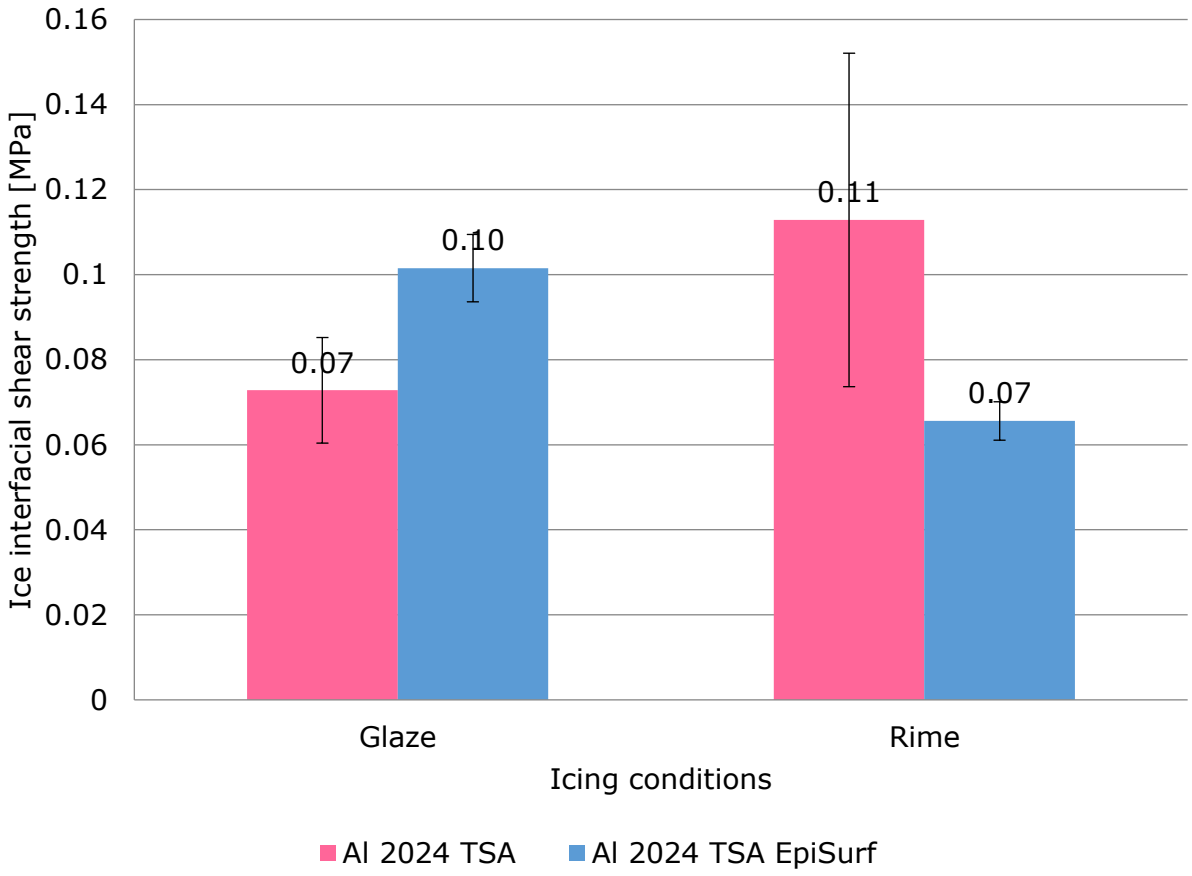

Figure 4-5: Results of bending cantilever test experiments in the icing wind tunnel with Al2024 TSA and Al2024 TSA EpiSurf.

In the bending cantilever test, the sample goes through 12 icing cycles before being tested in glaze ice conditions which results are shown in Figure 4-6 and in Table 4-5. Therefore, it could be possible that the sample degrades due to the ice shedding off the surface and consequently affecting the ice adhesion results.

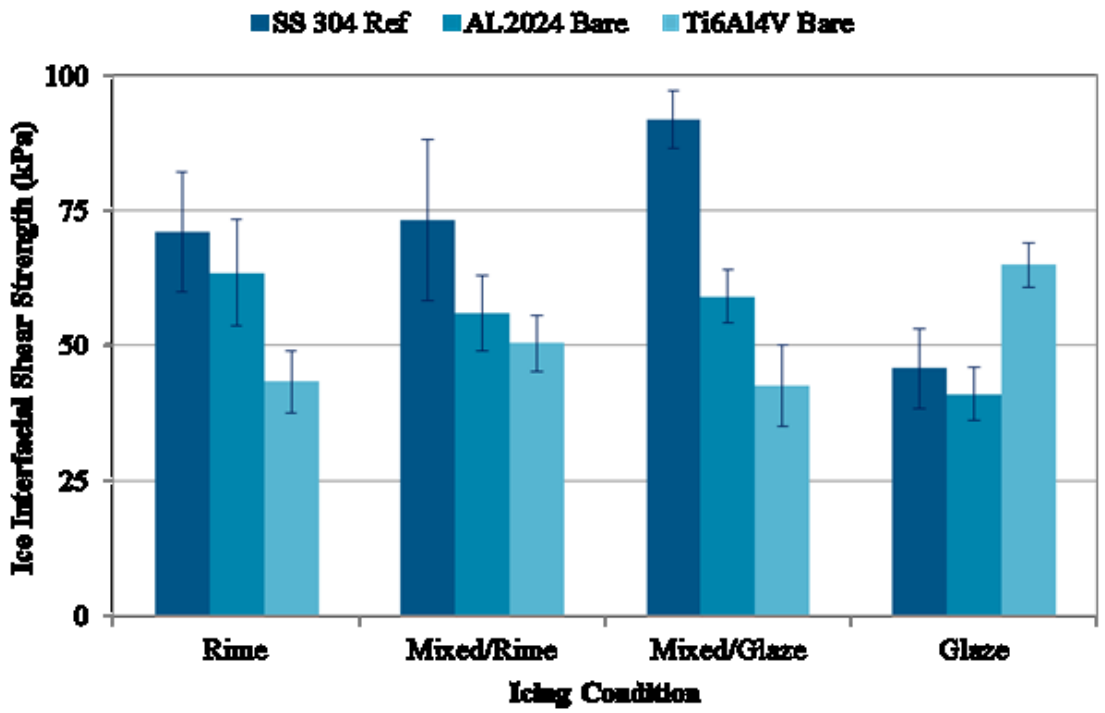

Figure 4-6: Results of bending cantilever test experiments in the icing wind tunnel [96].

Table 4-5: Summary of ice adhesion results in kPa from bending cantilever tests [96].

Sample		Test Condition			
Substrate	**Description**	**Rime**	**Mixed/Rime**	**Mixed/Glaze**	**Glaze**
Al2024	Ref	63±10	56±7	59±5	41±5
Ti6Al4V	Bare	43±6	50±5	43±8	65±4
SS304	Bare	71±11	73±15	92±5	46±7

The testing conditions used for the bending cantilever test are presented in Table 4-6. In glaze ice conditions, the cloud is concentrated in the center due to the higher LWC (1.0 g/m^3) thus creating a different ice shape. The temperature of the droplet at impact is zero degrees, thus the spreading of the droplet is different. After the first impact of a droplet on the surface, the surface will warm up and then the droplet will freeze. As ice builds up on thickness, the difference in temperature within the ice will create residual stress which will affect the heat transfer. Upon impact, the droplet can take the shape of a 'pancake', bounce back to a spherical shape or split, consequently the weber number (i.e., the dimensionless number that relates the inertial forces to the surface tension) different. The

airspeed in glaze ice conditions is 80 m/s compared to all the other conditions that are at 50 m/s, thus the droplet energy is also different. The ice adhesion results of glaze ice conditions can be affected due to the different accretion phenomena, different accretion rate, and different droplet interaction.

Table 4-6: Icing conditions (supercooled droplets) used during iCORE ice adhesion .

Ice Type	Total Air Temperature (T_t)	Airspeed (V)	Liquid Water Content (LWC)	Mean Effective Droplet Diameter (MVD)
	[°C]	[m/s]	[g/m^3]	[µm]
Rime	-20	50	0.3	20
Mixed/Rime	-20	50	0.8	20
Mixed/Glaze	-5	50	0.3	20
Glaze	-5	80	1.0	20

4.2.3 Correlation of Wettability Characteristics and Icephobic Results

Further analysis can be made by comparing the ice adhesion strengths of the surfaces obtained from the IWT tests to their respective wetting characteristics. Figure 4-7 and Figure 4-8 illustrate the trends of the CA of the surface against the measured adhesion strength for the Mode I test and the bending cantilever test respectively. From the results obtained from the Mode I test, it can be noted that a lower CA leads to a greater strength required to detach the ice from the surface. Thus, hydrophilic surfaces require leads to higher ice adhesion. Also, there is a tendency for the sample substrate to have a higher ice adhesion strength for the glaze ice condition. As mentioned in previous section, glaze ice is known to have a higher density compared to rime ice which is composed of air pockets.

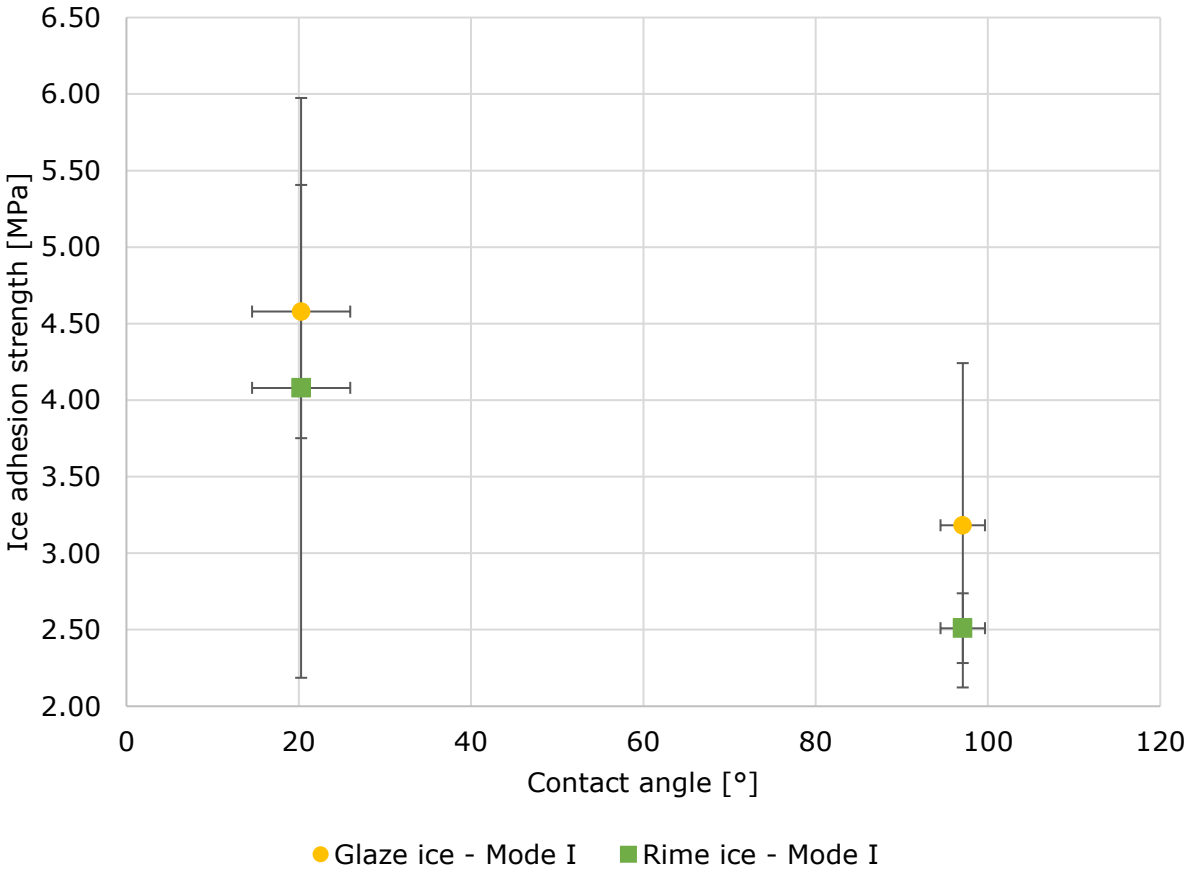

Figure 4-7: Contact angle vs ice adhesion strength obtained from Mode I test of Al2024 TSA (pink) and Al2024 TSA MecaSurf (blue) at glaze (square) and rime (triangle) ice conditions.

On the other hand, the trend of the results obtained from the bending cantilever tests is different from the Mode I test. For the Al2024 TSA, a higher ice adhesion strength resulted from the rime ice and not from the glaze ice. In addition, the statement that hydrophilic surface leads to higher adhesion strength is no longer valid in this case.

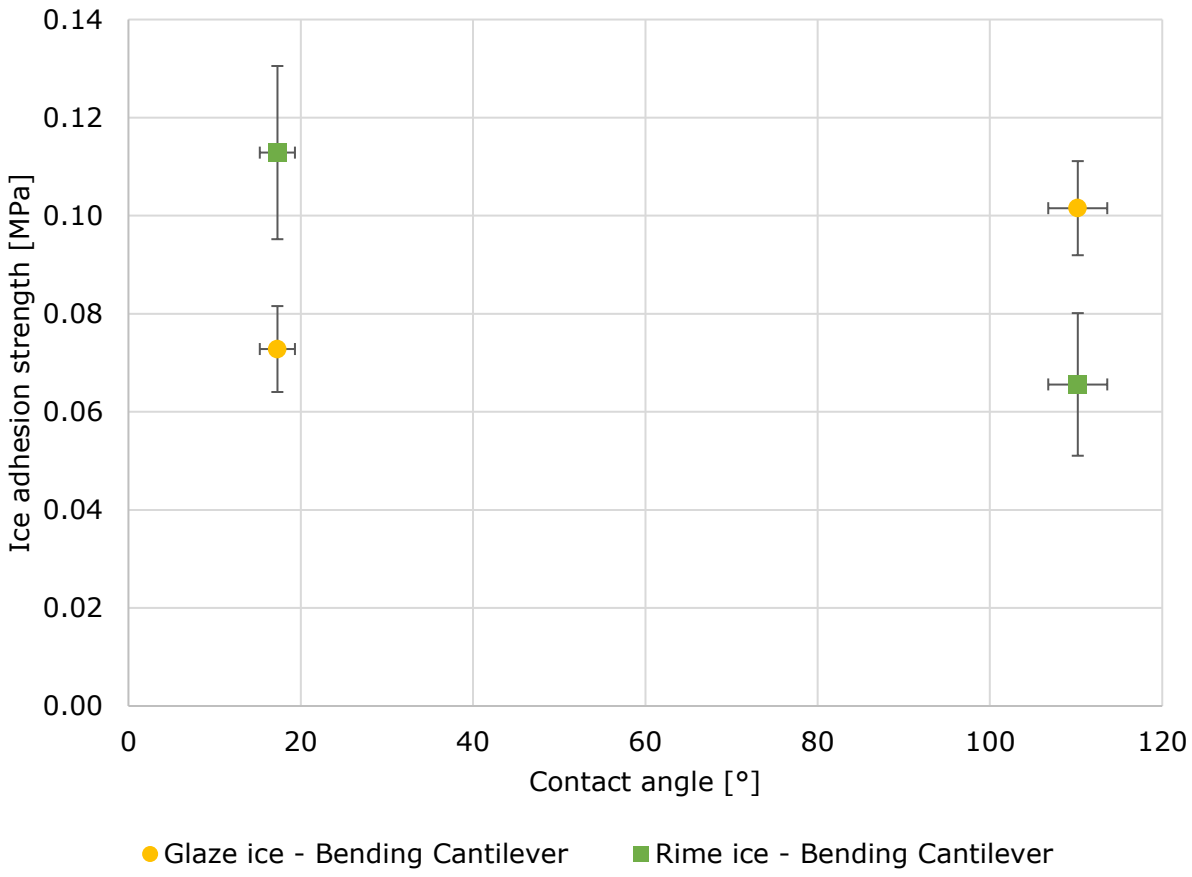

Figure 4-8: Contact angle vs ice adhesion strength obtained from bending cantilever test of Al2024 TSA (pink) and Al2024 TSA EpiSurf (blue) at glaze (square) and rime (triangle) ice conditions.

An extensive test campaign should be conducted to conclude on the ice adhesion trends and behaviors. Also, since only two samples were studied under two conditions, there is not enough information on what is happening in between these extreme conditions.

As expected, the average tensile strength obtained from the Mode I test is higher for the untreated sample than for the MecaSurf sample in both icing conditions. MecaSurf is a commercially available surface treatment that has the ability of reducing the surface tension of the substrate and consequently preventing substances from spreading on its surface. The same behavior was observed with the results from the bending cantilever tests for only the rime ice conditions. However, an untypical trend was observed for the

glaze ice conditions by noticing that a larger work was required to remove the ice from a substrate that has the additional surface treatment. In the bending cantilever test, bending and tensile stress are used to break the ice. Due to the complexity of this test method, the analytical model is idealizes since we do not understand yet what is actually happening at the ice-substrate interface. Using the Mode I test is preferred since we understand better what is happening and the results are more intuitive.

4.2.4 Source of Errors and Limitations

The test design could be modified by having a polymer holding cap; by doing so, the ice adhesion strength of the superimposing lip will be lower than the tested material. This will allow to have an ice adhesion result due to the substrate and not the holding cap. In addition, further testing can be performed to study the thickness of the superimposing lip from the holding cap to see how it affects the formation and adhesion results of ice. A simple test could be done by gluing the substrate directly on the sample holder and perform an investigation without the holding cap.

Extensive test campaign should be conducted with the same samples on both the Mode I test and the bending cantilever test under the same icing condition. By having enough data, the ice adhesion trends from the two tests can be correlated within each other and also the wetting characteristics of the surfaces.

Chapter 5 - Conclusions and Future Work

Countless industries face icing problems since it affects system performance, safety, efficiency, and operation. Anti-\ and de-icing systems are widely used to fight this issue. In the aviation field, different de-icing methods, e.g., chemicals and pneumatic boots, and active anti-icing methods, e.g., electrothermal heating elements, are commonly used to deal with the icing problem. These methods can be efficient in certain scenarios and atmospheric weather conditions at a cost: they are not always environmentally friendly since they require a certain energy source and some of the chemicals that are used can be harmful. Passive icephobic coatings are beneficial in contrast to other used methods since they can be derived from environmentally friendly chemicals and they do not require additional energy to operate. The development of newly-engineered coatings involves fundamental understanding of the physical mechanism of bonding between the ice and surface interface.

Intended to contribute to further study the icing problem and to develop a deeper understanding of the ice adhesion issue, a Mode I test was developed and set-up in the lab-scale icing wind tunnel at Airbus. The simple (in principle) Mode I test helps screening different surfaces by measuring the level of ice adhesion on the surface; however, the results obtained are valid for comparison and not to be taken as absolute numbers. In addition, the testing goal is not to perform fundamental ice research but rather to have a validation tool and to better understand the icing behavior on a surface. To validate the performance of the new implemented Mode I test, samples that were previously tested with a bending cantilever rig were tested with the new Mode I test rig. The data comparison between both tests accommodated an evaluation of the testing setup quality and validated the obtained data. The bending cantilever and the Mode I tests are causing ice fracture and delamination in different manners; thereby, the ice adhesion results from the same samples in the same icing conditions are not expected to be similar, but to show a similar trend.

The primary objective of developing and implementing a Mode I test into the iCORE IWT to measure the ice adhesion strength in different icing conditions was successfully achieved. Based on previous developed Mode I testing apparatus, the system was optimized by eliminating the vacuum system and replacing the PTFE disk with a thin elastomer (e.g., small piece of rubber balloon). This reduces the preparation and experimental time. In addition, the sample holder was designed to be versatile and be able to accommodate samples with varying thickness as well to accommodate non-metallic substrates. This optimized design allows a simple and quick installation of the sample to be tested, thereby reducing the time within testing runs. Further studies can be conducted by changing the material of the holding cap of the sample holder to a material with a known adhesion strength (any polymer). This will allow to increase the accuracy of the adhesion strength of the tested sample. Three reference substrates were characterized by measuring the wetting properties (CA, ROA, and CAH) and their respective surface roughness.

In order to validate the functioning of the new testing rig, the ice adhesion results of two samples, Al2024 TSA and Al2024 TSA MecaSurf, tested in glaze and rime ice conditions were compared with the previously obtained results of the same substrates from the bending cantilever test. The wettability characteristics and surface roughness for each sample were measured. Based on the results obtained for this thesis, the CA of the sample increased significantly when the commercially available hydrophobic coating, e.g., MecaSurf or EpiSurf, was applied. Nevertheless, the droplet mobility remained the same since the ROA only varied from three of degrees. The surface became smoother by applying the hydrophobic coating since the surface roughness decreased. The results from the Mode I adhesion test corroborated the hypothesis that more force is required to remove the accreted ice on a surface that showed poor wettability characteristics. However, the previously obtained results from the bending cantilever test showed a different trend: in glaze ice conditions there was a switch and a higher ice adhesion strength resulted for the sample with the hydrophobic coating. One of the explanations for this behavior is that when bending cantilever tests are done, a sample will go through 9 icing cycles before being studied in glaze ice conditions since other icing conditions

(rime, mixed/rime, mixed/glaze) are performed before. In glaze ice conditions, the LWC and the airspeed are larger; this means that bigger droplet are impacting the surface at higher speeds which results in faster ice growth with random nucleation. A possible wear of the coating could be due to the impact of the droplet and the shedding of the ice. Correlation studies were performed by comparing the wetting properties and the ice adhesion results which revealed that there could be a tendency of hydrophilic surfaces to have higher ice adhesion strength. More testing should be done in order to validate why higher ice adhesion strength resulted in glaze conditions for a surface that resulted in lower ice adhesion strength for the other testing conditions. Based on the experiments performed, the Mode I test was successfully working and all the sub systems were functioning well.

The experiments done in the IWT were performed with the goal to confirm the overall functioning of all the sub-systems as a unit and its operation when installed in the IWT. Despite the successful implementation of the new test rig, there still exist areas for continued development; while operating the new Mode I test as the scope of this thesis, the opportunities for enhancing testing and analysis features were highlighted. Some recommendations for further improvement of the new test rig are listed below:

- → Make use of a combination of pressure and acoustic emission sensors for early crack detection and crack propagation until total failure of the accreted ice.
- → Perform testing to investigate on the efficient surface area of the sample needed to perform the test. In other words, the actual surface of the sample that is useful for the ice to accrete and necessary to perform Mode I test.
- → Perform Mode I test without an installed sample to obtain the offset result of the apparatus. This offset can be used when performing cross-validation of the ice adhesion results with a Mode I test installed in a different research facility.
- → The lip of the holding cap can have an effect on the results obtained from Mode I test. If the sample to be tested has a high quality surface with a low adhesion, the ice might adhere to the exposed area of the holding cap which will induce errors to the obtained fracture energy. This can be resolved by having a holding cap made

of a material with a known lower ice adhesion (e.g., plastic). Then, tests should be performed to see it the material of the holding cap has an effect on the Mode I test results. The sensibility of the testing capability of the Mode I test developed can be found; consequently, the limit of the coating quality level that can be investigated in the Mode I test will be known. Also, when ice is formed in the IWT by accelerating droplets on the sample, water droplets will freeze and expand due the water properties. This will create strong interlocking effect of the ice on the lip of the sample holder creating false ice adhesion results. Ideally, the ice would be accreted only on the sample surface.

→ The ice thickness set for the Mode I tests was based on the theoretical derivation from the fracture energy equation and was found to be 2.5 fold the defect size [67, 38]. However, the ice adhesion also depends on the surface area where the ice is accreted and the pressure used to break it. More testing should be done with varying ice thickness to correlate with the ice thickness found from the fracture energy equation.

→ The thickness of the sample must be rigid enough to avoid excessive deformation when the bulk ice is detached when performing Mode I tests. The neutral axis depends on the thickness of the sample relative to the ice thickness; ideally, the neutral axis should be at the ice-sample interface. For this study, the sample thickness was a requirement but further experiments can be performed with different sample thickness to observe if it has an effect on the ice adhesion found.

The implementation of the Mode I test to the iCORE facilities contributes to further investigation of the icing behavior of surfaces for anti-icing applications. The bending cantilever test allows to study the ice adhesion at the interface as a result of compressive and tensile stresses. On the other hand, the Mode I test is a complementary experiment that allows to study the ice adhesion due to tensile stresses leading to a more profound characterization of ice phobic samples.

References

[1] F. Lamraoui, G. Fortin, R. Benoit, J. Perron and C. Masson, "Atmospheric icing severity: Quantification and mapping," *Atmospheric Research,* vol. 125, pp. 57-75, 2013.

[2] E. L. Lecomte, A. W. Pang and J. W. Russell, "Ice Storm'98," *ICLR Research Paper Series,* vol. 1, 1998.

[3] Statistics Canada, "The Storm," *Catalogue no. 16F0021XIB.*

[4] N. Dalili, A. Edrisy and R. Carriveau, "A review of surface engineering issues critical to wind turbine performance," *Science Direct - Renewable and Sustainable Energy Reviews,* vol. 13, pp. 428-438, 2009.

[5] J. L. Laforte, M. A. Allaire and J. Laflamme, "State-of-the-art on power line de-icing," *Atmospheric Research,* vol. 46, pp. 143-158, 1998.

[6] C. Laforte and A. Beisswenger, "Icephobic material centrigue adhesion test," in *International Workshop on Atmospheric Icing of Structures (IWAIS XI)*, Montreal, 2005.

[7] K. M. Al-Khalil, T. G. Keith, K. J. Dewitt, J. K. Nathman and D. A. Dietrich, "Thermal analysis of engine inlet anti-icing systems," *Journal of Propulsion and Power,* vol. 6, no. 5, pp. 628-634, 1990.

[8] National Transportation Safety Board, "Aircraft Accident Report - Crash During

Approach to Landing Circuit City Stores, Inc. Cessna Citation 560, N500AT," Colorado, 2005.

[9] J. M. Sayward, "Seeking Low Ice Adhesion," Special Report 79-11; U.S. Army Cold Regions Research and Engineering Laboratory, Hanover, 1979.

[10] The AOPA Air Safety Foundation, "Aircraft Icing," *Safety Advisor,* vol. 1, 2008.

[11] J. W. Jasiknski, S. C. Noe, M. C. Selig and M. B. Bragg, "Wind turbine performance under icing conditions," *Journal of Solar Energy Engineering,* vol. 120, no. 1, pp. 60-65, 1998.

[12] P. M. Struk, A. P. Broeren, J.-C. Tsao, M. Vargas and W. B. Wright, "Fundamental Ice Crystal Accretion Physics Studies - NASA/TM—2012-217429," in *International Conference on Aircraft and Engine Icing and Ground Deicing sponsored by SAE International*, Chicago, 2011.

[13] M. B. Bragg, A. P. Broeren and L. A. Blumenthal, "Iced-airfoil aerodynamics," *Progress in Aerospace Sciences,* vol. 41, no. 5, pp. 323-362, 2005.

[14] E. W. Brouwers, J. L. Palacios and E. C. Smith, "The experimental investigation of a rotor hover icing model with shedding," in *American Helicopter Society 66th Annual Forum*, Phoenix, 2010.

[15] Bureau d'Enquêtes et d'Analyses, "Final Report on the accident on 1st June 2009 to the Airbus A330-203 registered F-GZCP operated by Air France flight AF 447 Rio de Janeiro - Paris," 2012.

[16] W. Xi, Z. Qiao, C. Zhu, A. Jia and M. Li, "The preparation of lotus-like super-

hydrophobic copper surfaces by electroplating," *Applied Surface Sciences,* vol. 255, pp. 4836-4839, 2009.

[17] S. Farhadi, M. Farzaneh and S. A. Kulinich, "Anti-icing perforamce of superhydrophobic surfaces," *Applied Surface Science,* vol. 257, pp. 6264-6269, 2011.

[18] S. S. Latthe, A. B. Gurav, C. S. Maruti and R. S. Vhatkar, "Recent Progress in Preparation of Superhydrophobic Surfaces: A Review," *Journal of Surface Engineered Materials and Advanced Technology,* vol. 2, pp. 76-94, 2012.

[19] V. K. Croutch and R. A. Hartley, "Adhesion of ice to coating and the performance of ice release coating," *Journal of Coatings Technologies,* vol. 64, no. 815, pp. 41-52, 1997.

[20] Y. Wang, D. Orol, J. Owens, K. Simpson and H. J. Lee, "Design and Development of Anti-Icing Aluminum Surface," *Materials Sciences and Applications,* vol. 4, no. 6, 2013.

[21] T. M. e. a. Schutzius, "Physics of Icing and Rational Design of Surfaces with Extraordinary Icephobicity," *Langmuir,* vol. 31, pp. 4807-4821, 2015.

[22] C. Laforte, J.-C. Carrière and J.-L. Laforte, "How a solid coating can reduce the adhesion of ice on a structure," in *International Workshop on Atmospheric Icing on Structures*, 2002.

[23] S. A. Kulinich, S. Farhadi, K. Nose and X. W. Du, "Superhydrophobic Surfaces: Are They Really Ice-Repellent?," *Langmuir,* vol. 27, no. 1, pp. 25-29, 2011.

[24] E. Bonaccurso, E. Campazzi, C. Herrles and V. Vercillo, "Testing Functional Aeronautical Coatings for Improved Performance and Durability," *Airbus, Surface Engineering Department,* 2018.

[25] R. J. Hansam and S. Turnock, "Investigation of surface water behavior during glaze ice accretion," *Journal of Aircraft,* vol. 26, no. 2, pp. 140-147, 1989.

[26] C. Antonini, M. Innocenti, T. Horn, M. Marengo and A. Amirfazli, "Understanding the effect of surperhydrophobic coatings on energy reduction in anti-icing system," *Cold regions science and technology,* vol. 67, pp. 58-67, 2011.

[27] S. M. Fikke, E. Kristjánsson and B. E. K. Nygaard, *Modern meteorology and atmospheric icing, in Atmospheric Icing of Power Networks,* Dordrecht: Springer, 2008, pp. 1-29.

[28] G. Fortin and J. Perron, "Ice Adhesion Models to Predict Shear Stress at Shedding," *Journal of Adhesion Science and Technology,* vol. 26, no. 4-5, pp. 523-553, 2012.

[29] M. J. Kreder, J. Alvarenga, P. Kim and J. Aizenberg, "Design of Anti-Icing Surfaces: Smooth, Textured or Slippery?," *Nat. Rev. Mater.,* vol. 1, 2016.

[30] K. K. Varanasi, T. Deng, J. D. Smith, M. Hsu and N. Bhate, "Frost Formation and Ice Adhesion on Superhydrophobic Surfaces," *Appl. Phys. Lett.,* vol. 97, pp. 2010-2012, 2010.

[31] "World Atlas," What Is The Hydrologic Cycle?, [Online]. Available: https://www.worldatlas.com/articles/what-is-the-water-hydrologic-cycle.html.

[Accessed 14 06 2019].

[32] Aviation Weather Services, Hazardous Weather Phenomena, Airframe Icing, Australian Government Bureau of Meteorology, 2013.

[33] M. H. Foder, "ISO 12494" Atmospheric Icing of Structures" and How to Use It," *The Eleventh International Offshore and Polar Engineering Conference. International Society of Offshore and Polar Engineers,* 2001.

[34] Civil Aviation Authority, "Aircraft Icing Handbook Version 1," Safety Education and Publishing Unit, New Zealand, 2000.

[35] R. K. Jeck, "14 CFR Appendix C to Part 25, Appendix C to Part 25," Federal Aviation Administration (FAA) Airport and Aircraft Safety, Washington.

[36] J. Blake, D. D. Thompson, D. Raps, T. Strobl and E. Bonaccurso, "Effects of Surface Characteristics and Droplet Diameter on the Freezing of Supercooled Water Droplets Impacting a Cooled Substrate," *Transactions of Japanese Society for Medical and Biological Engineering,* vol. 51, 2014.

[37] Civil Aviation Authority, Aircraft Icing Handbook, New Zealand: Safety Education and Publishing Unit, 2002.

[38] M.-L. Pervier, "Mechanics of ice detachment applied to turbomachinery (Phd Thesis)," Cranfield University, Cranfield, 2012.

[39] M. Kline, "How High? Clouds and their relative heights," *DogFoose,* 2012.

[40] Federal Aviation Administration, U.S. Code of Federal Regulations, Title 14

(Aeronautics and Space), Part 25 (Airworthiness Standard: Transport Category Airplanes), Appendix C, Washington D.C.: National Archives and Records Administration, U.S. Government Printing Office, 1999.

[41] P. J. Perkins and W. J. Rieke, In-flight icing, Ohio: Sporty's Pilot Shop, 1999.

[42] T. Strobl, S. Storm, M. Kolb, J. Haag and M. Hornung, "Development of a hybrid ice protection system based on nanostructured hydrophobic surfaces," in *29th Congress of the International Council of the Aeronautical Sciences*, St. Petersburg, 2014.

[43] A. Heinrich, R. Ross, G. Zumwalt, J. Provorse, V. Padmanabhan, J. Thompson and J. Riley, Aircraft Icing Handbook, vol. 2, Springfield: National Technical Information Service, 1991.

[44] D. L. Kohlmann, W. G. Schweikhard and P. Evanich, "Icing-Tunnel Tests of a GlycolExuding, Porous Leading-Edge Ice Protection System," *Journal of Aircraft,* vol. 19, no. 8, pp. 647-654, 1982.

[45] L. Makkonen, "Ice Adhesion - Theory, Measurements and Countermeasures," *Journal of Adhesion Science and Technology,* vol. 26, pp. 413-445, 2012.

[46] M. Susoff, K. Siegmann, C. Pfaffenroth and M. Hirayama, "Evaluation of icephobic coatings—Screening of different coatings and influence of roughness," *Applied Surface Science,* vol. 282, pp. 870-879, 2013.

[47] R. Menini and M. Farzaneh, "Advanced Icephobic Coatings," *Journal of Adhesion Science and Technology,* vol. 25, pp. 971-992, 2011.

[48] C. Antonini, "Superhydrophobicity as a strategy agaisnt icing," *Universta Degli Studi Di Bergamo,* 2011.

[49] J. Chen, J. Liu, M. He, K. Li, D. Cui, Q. Zhang, X. Zeng, Y. Zhang, J. Wang and Y. Song, "Superhydrophobic surfaces cannot reduce ice adhesion," *Applied Physics Letter,* vol. 101, no. 11, pp. 111603-1-11603-3, 2012.

[50] H. J. Ensikat, P. Ditsche-Kuru, C. Neinhuis and W. Barthlott, "Superhydrophobicity in perfection: the outstanding properties of the lotus leaf," *Beilstein Journal of Nanotechnology,* vol. 2, pp. 152-161, 2011.

[51] C.-J. Zhou, D. Tian and J.-H. He, "What factors affect Lotus effect?," *Thermal Science,* vol. 22, no. 4, pp. 1737-1743, 2018.

[52] M. Nosonovsky and V. Hejazi, "Why Superhydrophobic Surfaces Are Not Always Icephobic," *ACS Nano,* vol. 6, no. 10, pp. 8488-8491, 2012.

[53] H. Dodiuk, S. Kenig and A. Dotan, "Do Self-cleaning Surfaces Repel Ice?," *Journal of Adhesion Science and Technology 26,* vol. 26, pp. 701-714, 2012.

[54] Y. Yuan and T. Randall Lee, Contact Angle and Wetting Properties. In: Bracco G., Holst B. (eds) Surface Science Techniques, Berlin, Heidelberg: Springer Series in Surface Sciences, 2013.

[55] T. Strobl, D. Raps, D. Paulus and M. Hornung, "Evaluation of Roughness Effects on Ice Adhesion," in *5th AIAA Atmospheric and Space Environments Conference*, San Diego, 2013.

[56] M. F. Hassan, "The variation of ice adhesion strength with substrate surface," *Measurement Science and Technology,* vol. 21, pp. 1-9, 2010.

[57] H. Koivuluoto, C. Stenroos, R. Ruohomaa, G. Bolelli, L. Lusvarghi and P. Vuoristo, "Vuoristo, Research on icing behavior and ice adhesion testing of icephobic surfaces," in *IWAIS*, Uppsala, 2015.

[58] D. Myers, Surfaces, Interfaces, and Colloids: Principles and Applications, 2nd edn, New York: Wiley-VCH, 1999.

[59] M. R. Kasaai and M. Farzaneh, "Evaluation of mechanisms of ice adhesion on power network equipment," in *Proceedings of OMEGA, 23 International Conferences of Offshore*, Vancouver, 2004.

[60] Z. Ghalmi, R. Menini and M. Farzaneh, "Theoretical studies and quantification of ice adhesion mechanisms," in *Proceeding of the 13th International Workshop on Atmospheric Icing of Structures, IWAIS*, Andermatt, 2009.

[61] W. D. Callister and D. G. Rethwisch, "Materials Science and Engineering An Introduction.," *John Wiley & Sons,* vol. 9, 2013.

[62] S. Kulinich and M. Farzaneh, "Ice adhesion on super-hydrophobic surfaces," *Applied Surface Science,* vol. 255, pp. 8153-8157, 2009.

[63] E. H. Andrews and A. Stevenson, "Fracture energy of epoxy resin under plane strain conditions," *J. Mater. Sci. ,* vol. 13, pp. 1680-1688, 1978.

[64] E. H. Andrews and N. A. Lockington, "The cohesive and adhesive strength of ice,"

J. Mater. Sci. , vol. 18, p. 1455–1465, 1983.

[65] H. Tada, P. C. Paris and G. R. Irwin, "The stress analysis of cracks handbook - Third Edition," ASME, New York, 2000.

[66] D. W. Hammond, "Microstructure and Mechanical Properties of Some Small Impact Ice Accretions," *7th International Workshop on Atmospheric Icing of Structures,* pp. 55-59, 1996.

[67] E. P. Moncholi, "An experimental and numerical study on the effect of some properties of non-metallic materials on the ice adhesion level (PhD Thesis)," Cranfield University, Cranfield, 2013.

[68] T. Strobl, D. Raps and M. Homung, "Comparative Evaluation of Ice Adhesion Behavior," *World Academy of Science, Engineering and Technology,* vol. 68, pp. 1673-1678, 2012.

[69] R. M. Fillion, A. R. Riahi and A. Edrisy, "Design factors for reducing ice adhesion," *Journal of adhesion science and technology,* vol. 31, no. 21, p. 2271–2284, 2017.

[70] O. JunFei, S. QinWen, W. ZhiLe, W. Fajun, X. MingShan, L. Wen and Y. GuiLong, "Sessile droplet freezing and ice adhesion on aluminum with different surface wettability and surface temperature," *Science China, Physics, Mechanics & Astronomy,* vol. 58, no. 7, pp. 076801-1-076801-8, 2016.

[71] S. Ronneberg, C. Laforte, C. Volat, J. He and Z. Zhang, "The effect of ice type on ice adhesion," *AIP Advances,* vol. 9, pp. 055604-1-055604-8, 2019.

[72] P. Beeram, R. Waldman and H. Hu, "Ice Adhesion Measurements of Ice Mitigation

Coatings Pertinent to Aircraft Icing," in *9th AIAA Atmospheric and Space Environments Conference*, Colorado, 2017.

[73] M. Javan-Mashmool, "Theoretical and Experimental Investigations for Measuring Interfacial Bonding Strength between Ice and Substrate," *Université du Québec,* 2005.

[74] M. Bottin and M. Carbonaro, "Concept Design of Wind Tunnel for Icing Application," von Karman Institute for Fluid Dynamics, Sint-Genesius-Rode, 2009.

[75] T. Hauk, "Erweiterung des Eis-Windkanals (iCORE) und Durchführung der ersten Kalibrier- und Strömungsqualitätsmessungen," 2012.

[76] Karl Klein Ventilatorenbau GmbH - Industrieventilatoren, "Company Profile," [Online]. Available: https://www.karl-klein.de/fileadmin/PDFs/Kataloge_Broschueren/KK_Gesamtkatalog.pdf. [Accessed 14 August 2018].

[77] T. Hauk, T. Strobl, D. Raps and E. Bonaccurso, "Icing and COntamination REsearch Facility (iCORE) Technical Report inclusive Satisfaction Form for IW CustomerTaufkirchen," Airbus Group, Taufkirchen, 2014.

[78] N. Karpen, "Analysis of the Influence of Air Stream and Spray Conditions on Drop Size Distribution, Drop Velocity and Drop Supercooling in an Icing Cloud Based on Optical Measurements Methods inside an Icing Wind Tunnel.," Airbus Group Innovations, Ottobrunn, 2017.

[79] United Sensor Corporation, [Online]. Available: http://www.unitedsensorcorp.com/pitot-pa.html. [Accessed 14 April 2018].

[80] R. S. Swanson and C. L. Gillis, "Wind-Tunnel Calibration and Correction Procedures for Three-Dimensional Models," National Advisory Committee for Aeronautics, Washington, 1944.

[81] Aerospace Recommended Practice ARP 5905, "Calibration and Acceptance of Icing Wind Tunnels," SAE International, 2015.

[82] Spraying Systems Co., "Automatic & Air Atomizing Spray Nozzles," 2015. [Online]. Available: https://www.spray.com/cat76/automatic/. [Accessed 14 March 2018].

[83] R. Adam, Experimentelle Untersuchung eines hybriden Enteisungssystems - Confidential, Ottobrunn: Airbus, 2014.

[84] The Linde Group, "GENIE® steckt voller Leben! Standfeste, mobile, intelligente Gasflasche.," Gases Division, Linde Gas Deutschland, Pullach, 2015.

[85] ImageJ, "Fiji Is Just ImageJ (FIJI)," [Online]. Available: https://imagej.net/Fiji. [Accessed 14 August 2018].

[86] Hans Turck GmbH & Co. KG, "Compact Multiprotocol I/O Module for Ethernet (TBEN-S2-4A)," [Online]. Available: https://pdb2.turck.de/repo/media/_us/Anlagen/Datei_EDB/edb_6814025_eng_us.pdf. [Accessed 14 June 2018].

[87] Modbus Tools, "Witte Software - Modbus Poll User Manual - Modbus Master Simulation," February 2018. [Online]. Available: http://www.modbustools.com/ModbusPollManual.pdf. [Accessed 14 May 2018].

[88] Hans Turck GmbH & Co. KG, "Pressure Transmitter With Voltage Output (3-wire) PT160R-2004-U1-H1141," [Online]. Available: https://pdb2.turck.de/repo/media/_us/Anlagen/Datei_EDB/edb_6836543_eng_us.pdf. [Accessed 14 June 2018].

[89] T. Bharathidasan, V. Kumar, M. S. Bobji and R. Chakradhar, "Effect of wettability and surface roughness on ice-adhesion strength of hydrophilic, hydrophobic and superhydrophobic surfaces," *Applied Surface Science,* vol. 314, pp. 241-250, 2014.

[90] S. Kulinich and M. Farzaneh, "On ice-releasing properties of rough hydrophobic coatings," *Cold Regions Science and Technology,* vol. 65, no. 1, pp. 60-64, 2011.

[91] Surfactis Technologies, "MECASURF anti-spreading agents for micromechanisms," Surfactis Technologies, [Online]. Available: https://www.surfactis.com/mecasurf.html. [Accessed 14 April 2018].

[92] BANDELIN electronic GmbH & Co. KG, 2018. [Online]. Available: https://bandelin.com. [Accessed 14 August 2018].

[93] KRÜSS GmbH, "Advancing your Surface Science," [Online]. Available: https://www.kruss-scientific.com/products/contact-angle/dsa25/drop-shape-analyzer-dsa25/. [Accessed 14 August 2018].

[94] JENOPTIK AG, [Online]. Available: https://www.jenoptik.com. [Accessed 14 March 2018].

[95] S. Tarquini, C. Antonini, A. Amirfazli, M. Marengo and J. Palacios, " Investigation of ice shedding properties of superhydrophobic coatings on helicopter blades,"

Cold Regions Science and Technology, vol. 100, pp. 50-58, 2014.

[96] A. Laroche, V. Vercillo, N. Karpen and E. Bonaccurso, "Novel Setup for Measuring Ice Adhesion Strength in an Icing Wind Tunnel," in *SAE International Conference on Icing of Aircraft, Engines, and Structres*, Minneappolis, 2019.

[97] F. P. Beer, E. R. Johnston Jr, J. T. DeWolf and D. F. Mazurek, "Mechanics of Materials," *Mc Graw Hill,* vol. 7, p. 984, 2015.

[98] Hans Turck GmbH & Co. KG, "Turck Service Tool," [Online]. Available: http://pdb2.turck.de/en/DE/products/0000001a000293cb0002003a. [Accessed 14 June 2018].

[99] Modbus tools, "Modbus Poll," [Online]. Available: http://www.modbustools.com/modbus_poll.html. [Accessed 14 August 2018].

[100] G. Liger-Belair, "How Many Bubbles in your Glass of Bubbly?," *Phys. Chem. B,* vol. 118, pp. 3156-3163, 2014.

[101] "Aviation Accident Synopses World Wide Web Page," National Transportation Safety Board, [Online]. Available: http://www.ntsb.gov/avdata. [Accessed 13 August 2018].

[102] N. Sharifi, M. Pugh, C. Moreau and A. Dolatabadi, "Developing hydrophobic and superhydrophobic TiO2 coatings by plasma spraying," *Surface & Coatings Technology,* vol. 289, pp. 29-36, 2016.

[103] Simply Modbus, "Data Communication Test Software," [Online]. Available: http://www.simplymodbus.ca/FAQ.htm. [Accessed 14 July 2018].

[104] Modbus Organization, [Online]. Available: http://www.modbus.org/specs.php. [Accessed 14 June 2018].

[105] Modbus Organization, "Modbus messaging on TCP/IP - Implementation guide 1.0," Modbus.org, 2002.

[106] Modbus Organization, "Modbus application protocol specification V1.1b3," Modbus.org, 2012.

[107] J.-N. Helbach, "Empirical Investigation on the Icing Behaviour of Grid Structures in a Lab-scale Icing Wind Tunnel (Bachelor Thesis)," Airbus Group Innovations, München, 2015.

[108] Hans Turck Gmbh & Co. KG, "Compact power supply module in IP67 (PSU67-11-2440/P)," [Online]. Available: http://pdb2.turck.de/repo/media/_en/Anlagen/Datei_EDB/edb_6884257_gbr_en.pdf. [Accessed 14 June 2018].

[109] Hans Turck GmbH & Co. KG, "User Manual TBEN-S product family, digital and analog standard modules (D301347 1015 - TBEN-S1/S2)," TURCK, Muelheim an der Ruhr, 2015.

[110] L. H. Lee, Fundamentals of Adhesion, New York: Springer, 1991.

[111] V. F. Petrenko and R. W. Whitworth, Physics of ice, Oxford: Oxford University Press, 2002.

[112] A. J. Meuler, J. D. Smith, K. K. Varanasi, J. M. Mabry, G. H. McKinley and R. E. Cohen, "Relationships between Water Wettability and Ice Adhesion," *ACS Applied Materials Interfaces,* vol. 2, no. 11, pp. 3100-3110, 2010.

[113] K. R. Petty and C. D. Floyd, A statistical review of aviation airframe icing accidents in the U.S., Washington: National Transportation Safety Board, 2004.

[114] SAE Aerospace, Calibration and Acceptance of Icing Wind Tunnels - ARP-5905, Warrendale: SAE International, 2003.

[115] E. P. Lozowski and L. Makkonen, "Fifty Years of Progress in Modelling the Accumulation of Atmospheric Ice on Power Network Equipment," *IWAIS XI,* 2005.

[116] M. C. Chu and R. J. Scavuzzo, "Adhesive shear strength of impact ice," *AIAA Journal,* vol. 29, no. 11, pp. 1921-1926, 1991.

[117] A. Brooks, M. Cassissa and S. Halls, "GKN Technology: Leading the way toward more efficient aircraft," *GKN Aerospace,* 2014.

Appendices

Appendix A List of Equations

Equation 2.1	$cos\theta^* = r\ cos\theta$	20
Equation 2.2	$cos\theta^* = -1 + \emptyset_s\ [cos\theta + 1]$	20
Equation 2.3	$cos\theta = \frac{\gamma_{sv} - \gamma_{sl}}{\gamma_{lv}}$	20
Equation 2.4	$CAH = \theta_A - \theta_R$	22
Equation 2.5	$W_a = \gamma_S + \gamma_i - \gamma_{i,s}$	23
Equation 2.6	$W_a \approx \gamma_w(1 + cos\theta)$	23
Equation 2.7	$F = mr_R\omega^2$	31
Equation 2.8	$FE = \frac{\sigma_c^2\ c}{E\ f}$	35
Equation 2.9	$f = \left(\frac{1}{1-\nu^2}\right)\left\{\frac{3}{32}\left[\left(\frac{c}{h}\right)^3 + \left(\frac{c}{h}\right)\left(\frac{4}{1-\nu}\right)\right] + \frac{n}{\pi}\right\}^{-1}$	35

Equation 2.10 $K_{IC} = \sqrt{\frac{FE*E}{1-\nu^2}}$ 36

Equation 2.11 $\sigma_T = \frac{K_{IC}}{\sqrt{\pi* a_g}}$ 36

Equation 2.12 $e = \frac{1}{2\left(h_{al}+\frac{E_{ice}}{E_{al}}h_{ice}\right)}(h_{al}^2 - \frac{E_{ice}}{E_{al}}h_{ice}^2)$ 40

Equation 2.13 $EI_y = \frac{d^4w(x)}{dx^4} = q$ 41

Equation 2.14 $\tau(\vec{z}) = \frac{QES_y(\vec{z})}{EIb(\vec{z})}$ 41

Equation 2.15 $\tau_{int} = \frac{\varepsilon_{EF_{Al}}E_{ice}(h_{ice}^2+2h_{ice}|e|)}{2(x-l)(h_{al}-|e|)}$ 41

Equation 2.16 $\frac{EI_y}{\rho A}\frac{d^4w(x,t)}{dx^4} + \frac{d^2w(x,t)}{dt^2} = 0$ 41

Equation 2.17 $f_1 \approx 0.560\sqrt{\frac{EI_y}{\rho A l_{osc}^4}}$ 42

Equation 3.1 $Ma = \sqrt{\frac{2}{k-1}\left[\left(\frac{p_t}{p_{st}}\right)^{\frac{k-1}{k}} - 1\right]}$ 48

Appendix B Principle of Stresses and Planes

The fracture energy obtained from the Mode I test experiments is based on the plain strain [63, 30]. A body made of an elastic material can undergo shape and size changes as a response to an applied, external force. The stress (also called engineering stress), σ, is produced by the load being imposed perpendicularly, F, on the body cross section, A_0 [61]:

$$\sigma = \frac{F}{A_0} \qquad \text{Equation 5.1}$$

Strain (also called engineering strain), ε, is the response of the body under an applied static (or moving extremely slowly) stress represented by a unitless value, where l_o is the original length before a load application, and l_i is the instantaneous length [61]:

$$\varepsilon = \frac{l_i - l_0}{l_0} \qquad \text{Equation 1.2}$$

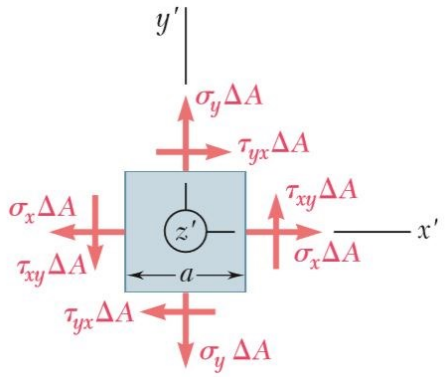

Figure 1-1: Positive resultant forces on a small element resulting from applied stress [97].

A body may be subjected to normal stress (either tensile or compressive), tangential stress (shear), or torsional stress. When the body is long enough and the strain is oriented in a particular direction — it can be assumed it is in the z-direction for these purposes, which is negligible compared with the two other orthogonal directions — the situation can be treated in a bi-dimensional space, as shown in Figure 1-1.

Appendix C Mode I Test Wind Tunnel Procedure

One of the principal goals established for this project was to set a testing procedure in order to ease the cross-validation of wind tunnel results from different facilities. This testing protocol was an attempt to synthetize the different approaches used for the simulation of icing conditions in wind tunnel tests. This set of recommendations focuses on wind tunnel research for characterisation and development of coatings that can be implemented in aircrafts to battle against icing, rain and sand erosion. It is an additional criterion to the SAE Aerospace Recommended Practice (Aerospace Recommended Practice) for the calibration and acceptance of icing wind tunnels [81].

Connecting Pressure Sensor

1. Connect the pressure sensor to the multiprotocol module at the channel 0 with the grey cable
2. Connect the power supply to the multiprotocol module with the grey cable
3. Connect the multiprotocol to the computer with the Ethernet cable (green color)
4. Plug the power supply to the wall socket
5. If everything is properly connected, the small LED light beside Channel 0 should be on
6. Secure the multiprotocol module in a fixed position
7. Open Turck Service Tool (Figure 1-2)

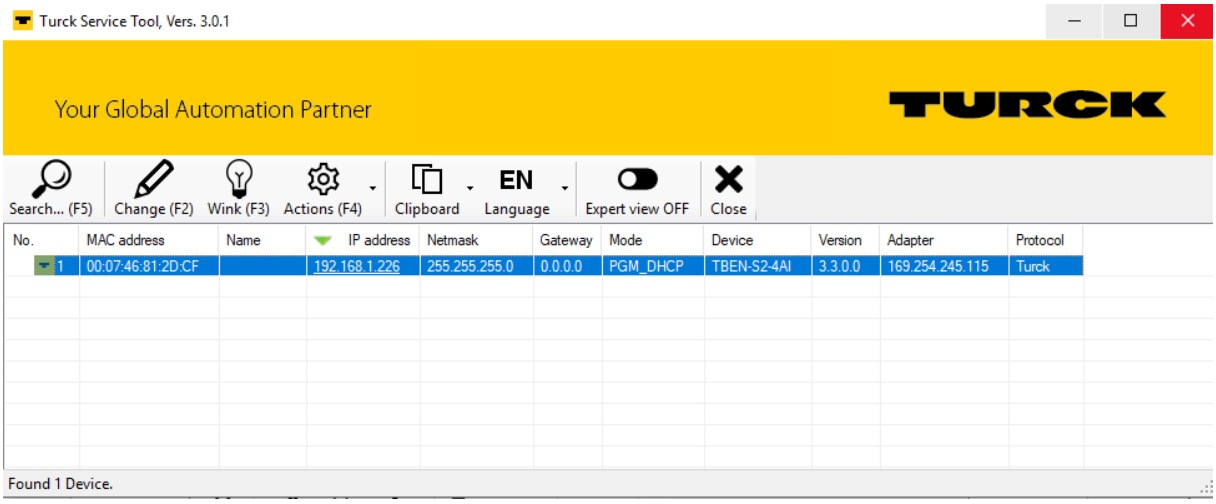

Figure 1-2: Turck service tool [98].

8. To access the device through the web server, open the web using the IP address
    - The default IP address is 192.168.1.254
    - http://192.168.1.254/index.html (PC and device must be on same network)
    - Login as an administrator using the password ‘password’
    - You can change the default password from this website
9. Configuration of the fieldbus interface
    - In the ‘Station Configuration’ tab on the left
    - Make sure the Ethernet and Modbus protocol do not have a check mark

Modbus Poll Setup

1. Open the Modbus Poll program [99]
2. Setup the connection by pressing F3 and referring to Figure 1-3

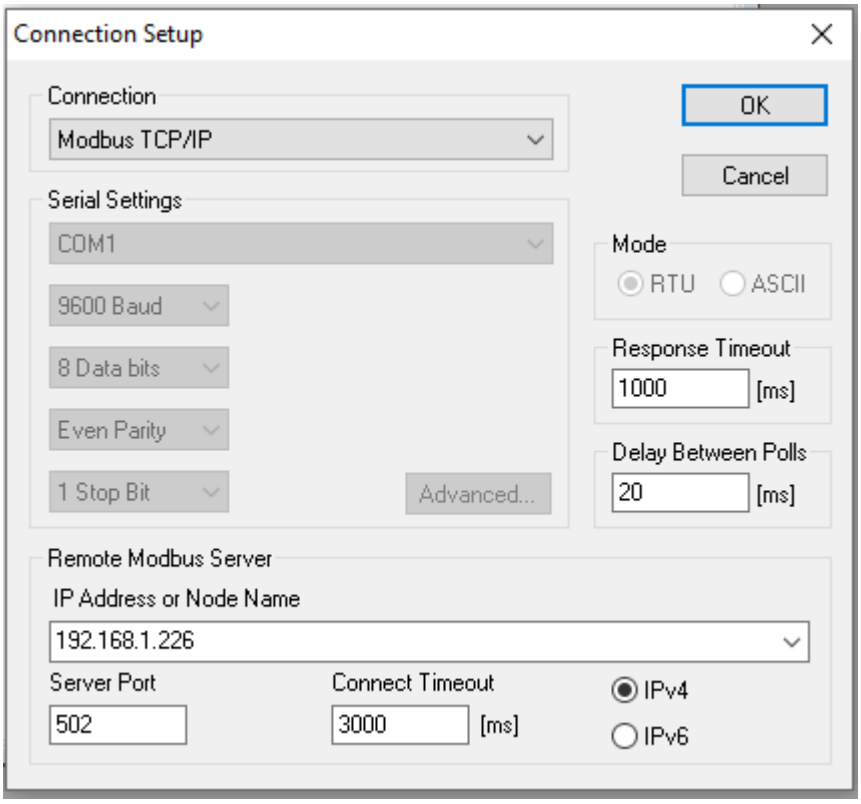

Figure 1-3: Connection setup of Modbus poll [99].

3. Define the data to be monitored by pressing F8 and referring to Figure 1-4. To achieve a faster transfer rate, set the *Scan Rate* in the *Read/Write Definition* to 1ms

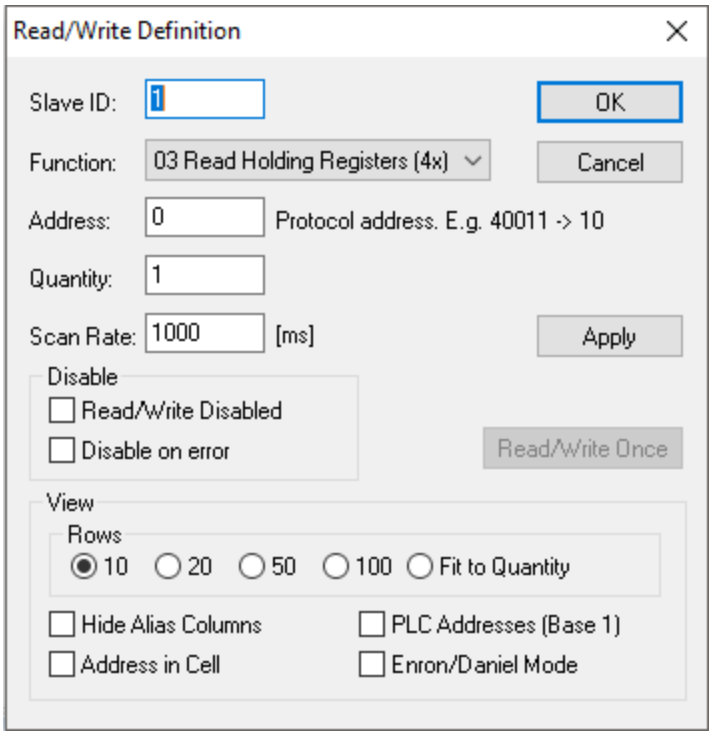

Figure 1-4: Data definition of Modbus poll [99].

4. Change the first cell name to *Voltage (mV)* as shown in Figure 1-5

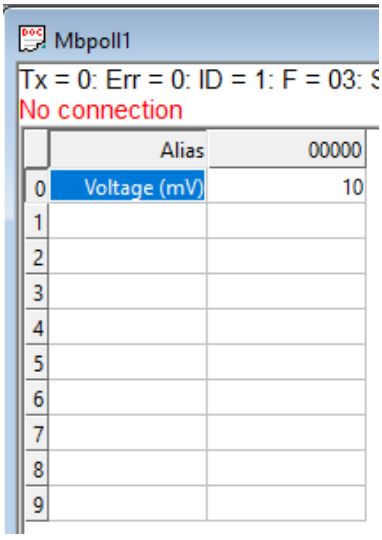

Figure 1-5: Modbus poll window example [99].

5. To configure the Excel logging press *Alt+X* and refer to Figure 1-6

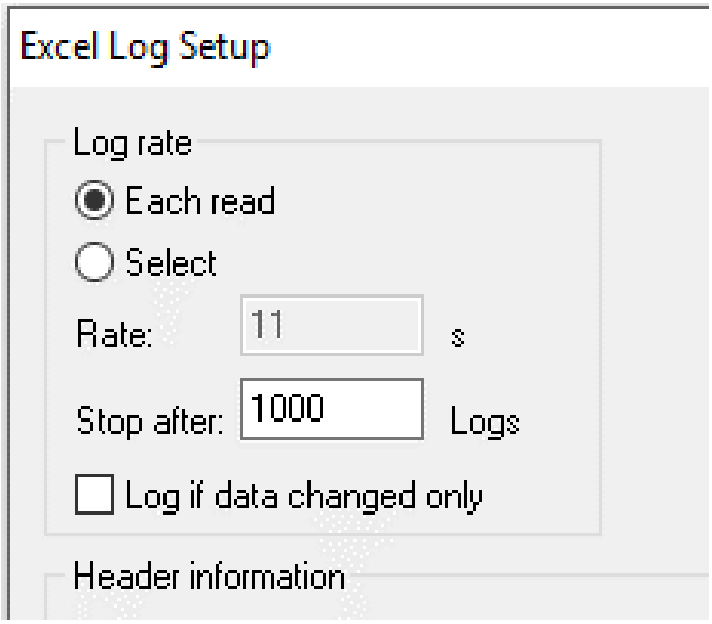

Figure 1-6: Setup for Modbus poll excel log [99].

Icing Wind Tunnel Procedure

1. Before installing the sample, make sure all the valves from the pressurized system and the gas cylinder are closed
2. Open the pressure valve SLOWLY on the first stage on the gas cylinder. No tools should be required
3. Open the pass valve of the pressurized system (Figure 1-7)

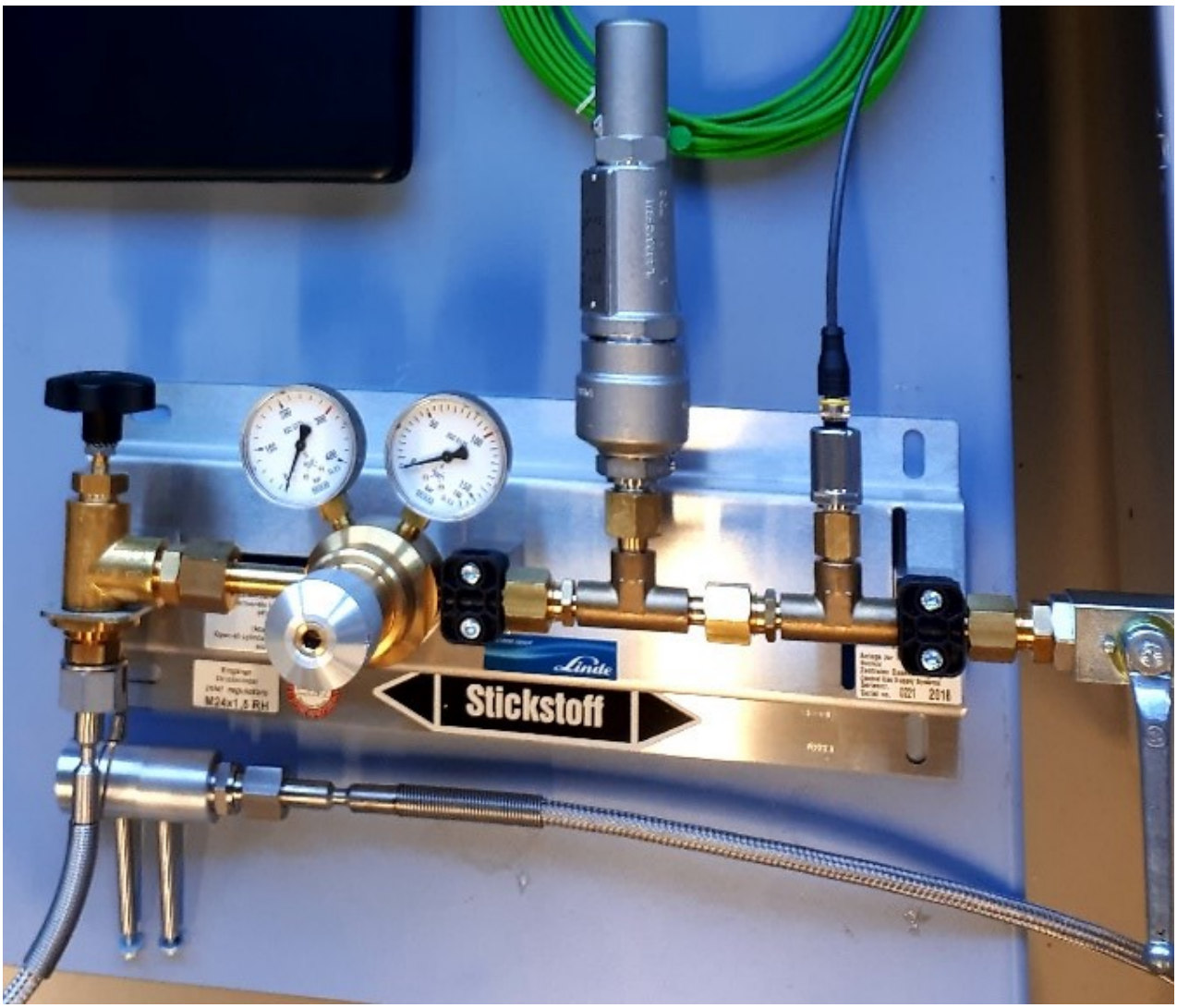

Figure 1-7: Mode I test pressurized system.

4. Install the sample on the holder. Make sure to wear gloves in order to avoid contaminating the surface
5. When screwing the cap, no force should be required. In the event that turning the cap becomes difficult, STOP and remove the cap carefully. Look for any defect in the threads of the cap and the sample holder. With the nitrogen air supply form the iCORE (not from the Mode I test), clean all surfaces of the threads. If after cleaning you cannot screw the cap without force, seek the help of the machinist
6. Secure all walls of the test section

7. Start main fan and cooling system
8. When the aimed parameters (ambient temperature and tunnel air speed) are stable, note it down in the prepared Excel sheet
9. Turn on the spray system according to the parameters settled with the conditions
10. Observe thickness of ice accretion to a target of 15 mm (thickness required for analytic solution [64])
11. Open the Excel log of Modbus poll
12. Switch on the pressurized system (Pressurization rate of 10 bar/sec)
13. Wait for the ice to shed
14. Switch off pressurized system when the ice is expulsed
15. Take note of the type of fracture (adhesive, cohesive or mixed)
16. From the pressure data acquired, take note of the critical pressure
17. For statistical analysis, repeat at least 3 times each condition for each sample

Appendix D Obtained Data From Sample Characterization

Table 1-1: Summary of contact angle measurements of Mode I test and bending cantilever test samples.

Sample			Size	CA	ROA	CAH	Wetting property
Substrate	Texture	Coating	[mm]	[°]	[°]	[°]	
Al2024	**Ref**	**-**	**ø30x1.6**	**104**	**90**	***33***	HB
Al2024	TSA	-	ø30x1.6	20	87	27	HL
Al2024	TSA	-	125x13x1.6	59	90	-	HL
Al2024	TSA	EpiSurf	125x13x1.6	122	90	-	HB
Al2024	TSA	MecaSurf	ø30x1.6	97	89	31	HB
Ti6Al4V	Ref	-	ø30x1.6	83	85	26	HL
Ti6Al4V	Nanotubes	-	ø30x1.6	13	53	18	HL
Ti6Al4V	Nanotubes	MecaSurf	ø30x1.6	158	4	19	SH
Ti6Al4V	Nanotubes	EpiSurf	125x13x1.6	166	24	-	SH

TSA: Tartaric Sulphur Acid anodizing to enhance the attraction to liquid and improve the adhesion with the MecaSurf

SH: Superhydrophobic

HB: Hydrophobic

HL: Hydrophilic

The reference titanium sample has a CA of 83° and 13° with the nanotubes applied to the surface and increases to 158° when the MecaSurf is applied. The ROA is decreased from 85° from the referenced Ti6Al4V to 53° with the nanotubes and when the MecaSurf is applied it decreases even more to 5°. The titanium surface treated with nanotubes and MecaSurf shows significant CA when compared to all the other samples with a really low ROA angle.

Table 1-2: Summary of surface roughness measurements of Mode I test and bending cantilever test samples.

Sample			Size	R_a	R_z
Substrate	Texture	Coating	[mm]	[µm]	[µm]
Al2024	**Ref**	**-**	**ø30x1.6**	**0.61±0.015**	**5.36±0.231**
Al2024	TSA	-	ø30x1.6	0.09±0.014	1.53±0.941
Al2024	TSA	MecaSurf	125x13x1.6	0.16±0.043	1.95±0.469
Ti6Al4V	Ref	-	ø30x1.6	0.45±0.007	3.03±0.084
Ti6Al4V	Nanotubes	-	ø30x1.6	0.44±0.081	3.11±0.801

Ti6Al4V	Nanotubes	MecaSurf	ø30x1.6	0.41±0.015	3.21±0.024

TSA: Tartaric Sulphur Acid anodizing to enhance the attraction to liquid and improve the adhesion with the MecaSurf

Ref: Reference

R_a: Arithmetical mean deviation of the assessed profile

R_z: Maximum height of profile

Table 1-3: Summary of surface roughness measurements of bending cantilever test samples [96].

Sample		Size	R_a	R_z	CA
Substrate	**Description**	**[mm]**	**[µm±SD]**	**[µm±SD]**	**[°±SD]**
Al2024	**Ref**	**125x13x1.6**	**0.017±0.005**	**0.150±0.037**	**59±3**
Ti6Al4V	Bare	125x13x1.6	**0.501±0.028**	**3.973±0.174**	**51±1**
SS304	Bare	125x13x1.6	**0.170±0.012**	**1.634±0.012**	**70±5**

Ref: Reference

R_a: Arithmetical mean deviation of the assessed profile

R_z: Maximum height of profile

CA: Contact angle

Table 1-4: Comparison of surface roughness of samples on values presented in literature.

Sample		Size	R_a	Ref
Substrate	**Description**	**[mm]**	**[µm]**	
Al6061	**Mirror-polished**	**32x50**	**0.0062**	[62]
Aluminium	Polished	340x30	~0.17	[57]
Al6061	Polished using 1 µm diamond suspension	25x75x1	0.022±0.001	[69]
Al6061	Sandblasted with a medium grit	25x75x1	3.04±0.1	[69]
Al6061	Sandblasted with a coarse grit	25x75x1	5.06±0.28	[69]
Al6061	Etching	-	0.05±0.02	[48]

R_a: Arithmetical mean deviation of the assessed profile

R_z: Maximum height of profile

Ref: Reference

Appendix E Obtained Data from Mode I Test

Mode I Test Samples

Date			Picture Number	Sample	Contact angle				Tilting table				
Sample Preparation	Characterization	IWT Test			Left (°)	Right (°)	Average (°)	Fitting Method	Roll-off Angle (°)	Advancing (°)	Receding (°)	Hysterisis(°)	Fitting Method
N/A	8/23/2018	N/A	1	Al2024 Ref	106.20	105.70	105.95	Young Laplace	90.00	111.10	74.00	37.10	Tangent
N/A	8/23/2018	N/A	2		102.70	102.30	102.50	Young Laplace	90.00	104.70	72.60	32.10	Tangent
N/A	8/23/2018	N/A	3		95.20	96.30	95.75	Young Laplace	90.00	95.60	66.40	29.20	Tangent
N/A	8/23/2018	N/A	4	Al2024 Ref	107.50	107.00	107.25	Young Laplace	90.00	107.60	75.90	31.70	Tangent
N/A	8/23/2018	N/A	5		108.00	107.20	107.60	Young Laplace	90.00	105.00	75.00	30.00	Tangent
N/A	8/23/2018	N/A	6		102.70	101.30	102.00	Young Laplace	90.00	107.50	70.20	37.30	Tangent
8/1/2018	8/23/2018	N/A	1	Al2024 TSA	30.50	23.90	27.20	Tangent	88.17	46.10	10.10	36.00	Tangent
8/1/2018	8/23/2018	N/A	2		10.00	15.90	12.95	Tangent	88.25	36.20	18.70	17.50	Tangent
8/1/2018	8/23/2018	N/A	3		38.00	11.50	24.75	Tangent	83.94	41.70	5.60	36.10	Tangent
8/1/2018	8/23/2018	N/A	4	Al2024 TSA	24.50	21.00	22.75	Tangent	87.88	39.50	11.50	28.00	Tangent
8/1/2018	8/23/2018	N/A	5		15.70	14.70	15.20	Tangent	88.31	38.80	18.80	20.00	Tangent
8/1/2018	8/23/2018	N/A	6		20.40	17.30	18.85	Tangent	86.72	40.00	16.60	23.40	Tangent
7/30/2018	8/23/2018	N/A	1	Al2024 TSA Mecasurf	111.40	111.40	111.40	Young Laplace	89.79	123.60	93.40	30.20	Tangent
7/30/2018	8/23/2018	N/A	2		109.30	109.30	109.30	Young Laplace	88.53	120.70	89.20	31.50	Tangent
7/30/2018	8/23/2018	N/A	3		113.60	113.60	113.60	Young Laplace	89.57	127.60	90.50	37.10	Tangent
7/30/2018	8/23/2018	N/A	4	Al2024 TSA Mecasurf	83.00	87.30	85.15	Ellipse Tangent-1	89.83	89.00	55.40	33.60	Tangent
7/30/2018	8/23/2018	N/A	5		84.30	83.00	83.65	Ellipse Tangent-1	89.72	93.30	64.50	28.80	Tangent
7/30/2018	8/23/2018	N/A	6		79.40	79.30	79.35	Ellipse Tangent-1	86.51	87.50	61.80	25.70	Tangent
N/A	8/23/2018	N/A	1	Ti6Al4V Ref	81.70	81.80	81.75	Ellipse Tangent-1	88.32	78.90	55.90	23.00	Tangent
N/A	8/23/2018	N/A	2		84.40	84.40	84.40	Young Laplace	86.86	83.30	59.00	24.30	Tangent
N/A	8/23/2018	N/A	3		85.70	85.70	85.70	Young Laplace	73.98	81.70	57.90	23.80	Tangent
N/A	8/23/2018	N/A	4	Ti6Al4V Ref	85.00	84.40	84.70	Ellipse Tangent-1	88.29	78.90	53.50	25.40	Tangent
N/A	8/23/2018	N/A	5		80.50	79.60	80.05	Ellipse Tangent-1	88.12	75.20	46.20	29.00	Tangent
N/A	8/23/2018	N/A	6		83.90	83.40	83.65	Ellipse Tangent-1	86.85	79.70	48.50	31.20	Tangent
8/1/2018	8/23/2018	N/A	1	Ti6Al4V Nanotubes	20.60	17.70	19.15	Tangent	88.50	38.00	14.80	23.20	Tangent
8/1/2018	8/23/2018	N/A	2		21.00	14.50	17.75	Tangent	87.87	34.00	9.00	25.00	Tangent
8/1/2018	8/23/2018	N/A	3		20.60	16.30	18.45	Tangent	70.95	36.10	3.20	32.90	Tangent
8/1/2018	8/23/2018	N/A	4	Ti6Al4V Nanotubes	8.40	6.00	7.20	Tangent	13.37	21.20	12.90	8.30	Tangent
8/1/2018	8/23/2018	N/A	5		5.30	12.30	8.80	Tangent	13.27	10.60	2.60	8.00	Tangent
8/1/2018	8/23/2018	N/A	6		4.60	11.80	8.20	Tangent	41.33	21.00	9.10	11.90	Tangent
8/30/2018	8/30/2018	N/A	1	Ti6Al4V Nanotubes MecaSurf	159.80	159.80	159.80	Young Laplace	1.41	164.00	159.70	4.30	Tangent
8/30/2018	8/30/2018	N/A	2		149.50	149.80	149.65	Ellipse Tangent-1	7.36	169.90	135.60	34.30	Tangent
8/30/2018	8/30/2018	N/A	3		164.90	164.90	164.90	Young Laplace	4.23	170.70	151.40	19.30	Tangent

	Average for each Sample					
	Contact angle		Tilting table			
	Average (º)	Std Dev	Roll-off Angle (º)	Std Dev	Hysterisis(º)	Std Dev
Al2024 Ref	101	5.2	90	0.0	33	4.0
Al2024 Ref	106	3.1	90	0.0	33	3.8
Al2024 TSA	22	7.6	87	2.5	30	10.7
Al2024 TSA	19	3.8	88	0.8	24	4.0
Al2024 TSA Mecasurf	111	2.2	89	0.7	33	3.7
Al2024 TSA Mecasurf	83	3.0	89	1.9	29	4.0
Ti6Al4V Ref	84	2.0	83	7.9	24	0.7
Ti6Al4V Ref	83	2.4	88	0.8	29	2.9
Ti6Al4V Nanotubes	18	0.7	82	10.0	27	5.2
Ti6Al4V Nanotubes	8	0.8	23	16.2	9	2.2

Color Legend	
Experiment Specs	User Input
Test Input	
Test Output	
Calculated Results	Excel Formulas

Constants		
k	1.405	Isentropic exponent of air
R	287.06	Gas constant [J/(kg·K)]
ρ	1.225	Air density at STP [kg/m3]
Pstp	101325	Air pressure at STP [Pa]
Tstp	20	Absolute air temperature at STP [°C]
E	8500000000	Young Modulus [Pa]
ν	0.31	Poisson's ratio
ag	0.00039	Grain Size [m]

Formulas

Mach Number (Ma)

$$Ma = \sqrt{\frac{2}{k-1}\left[\left(\frac{p_t}{p_{st}}\right)^{\frac{k-1}{k}} - 1\right]}$$

Static Temp. (Tst)

$$T_{st} = \frac{T_t}{1 + \frac{k-1}{2} Ma^2}$$

Velocity (V)

$$V = Ma\sqrt{k\,R\,T_{st}}$$

f-factor (f)

$$f = \left(\frac{1}{1-\nu^2}\right)\left\{\frac{3}{32}\left[\left(\frac{c}{h}\right)^3 + \left(\frac{c}{h}\right)\left(\frac{4}{1-\nu}\right)\right] + \frac{\pi}{\pi}\right\}^{-1}$$

Energy of Fracture (FE)

$$FE = \frac{\sigma_c^2\, c}{E\, f}$$

Fracture Toughness (K1c)

$$K_{IC} = \sqrt{\frac{FE * E}{1-\nu^2}}$$

Tensile Strength (σt)

$$\sigma_T = \frac{K_{IC}}{\sqrt{\pi * a_g}}$$

Name	Date of Test	Sample Studied		Test Condition	Test Start Time (t_i)	Total Temp. (T_t)	Ambient Temp. (T_a)	Fan Frequency	Condesing Unit Power	Humidity	Static Pressure (P_{st})	Total Pressure (P_t)	Mach Number (Ma)	Static Temp. (T_{st})	Velocity (V)
		Type	Day of 1st test			[°C]	[°C]	[Hz]	[%]		[Pa]	[Pa]		[°C]	[m/s]
20180730-Al2024_TSA_MecaSurf-005-Rime	30-Jul	Al 2024 TSA Mecasurf	30-Jul	Rime	Ø	-20.0	Ø	20.00	29.5	Ø	Ø	Ø	-	-	-
20180730-Cranfield_Sample-002-Rime	30-Jul	Cranfield	Old	Rime	Ø	-20.0	Ø	16.15	30.0	Ø	Ø	Ø	-	-	-
20180730-Cranfield_Sample-004-Rime	30-Jul	Cranfield	Old	Rime	Ø	-20.0	Ø	16.15	31.5	Ø	Ø	Ø	-	-	-
20180731-Al2024_TSA_MecaSurf-009-Glaze	31-Jul	Al 2024 TSA Mecasurf	30-Jul	Glaze	Ø	-5.0	Ø	30.00	26.0	Ø	Ø	Ø	-	-	-
20180731-Al2024_TSA_MecaSurf-010-Glaze	31-Jul	Al 2024 TSA Mecasurf	30-Jul	Glaze	Ø	-5.0	Ø	30.00	26.0	Ø	Ø	Ø	-	-	-
20180731-Al2024_TSA_MecaSurf-011-Glaze	31-Jul	Al 2024 TSA Mecasurf	30-Jul	Glaze	Ø	-5.0	Ø	29.50	31.0	Ø	Ø	Ø	-	-	-
20180731-Al2024_TSA_MecaSurf-012-Glaze	31-Jul	Al 2024 TSA Mecasurf	30-Jul	Glaze	Ø	-5.0	Ø	29.50	25.0	Ø	Ø	Ø	-	-	-
20180731-Al2024_TSA_MecaSurf-013-Glaze	31-Jul	Al 2024 TSA Mecasurf	30-Jul	Glaze	Ø	-5.0	Ø	30.00	30.5	Ø	Ø	Ø	-	-	-
20180731-Al2024_TSA_MecaSurf-Sys-000	31-Jul	Al 2024 TSA Mecasurf	30-Jul	Trial	Ø	Ø	Ø	Ø	Ø	Ø	Ø	Ø	-	-	-
20180801-Al2024_TSA_MecaSurf-000-Rime	1-Aug	Al 2024 TSA Mecasurf	1-Aug	Rime	10:20	-20.0	Ø	15.30	46.5	Ø	Ø	Ø	-	-	-
20180801-Al2024_TSA_MecaSurf-001-Rime	1-Aug	Al 2024 TSA Mecasurf	1-Aug	Rime	12:05	-18.4	Ø	15.30	45.0	Ø	Ø	Ø	-	-	-
20180801-Al2024_TSA_MecaSurf-002-Rime	1-Aug	Al 2024 TSA Mecasurf	1-Aug	Rime	12:50	-21.7	Ø	17.00	45.0	Ø	Ø	Ø	-	-	-
20180801-Al2024_TSA_MecaSurf-004-Rime	1-Aug	Al 2024 TSA Mecasurf	1-Aug	Rime	13:20	-20.9	Ø	17.00	45.0	Ø	1002.6	1019.7	0.16	-20.80	49.56
20180801-Al2024_TSA_MecaSurf-005-Rime	1-Aug	Al 2024 TSA Mecasurf	1-Aug	Rime	13:55	-21.7	Ø	20.00	38.0	Ø	1002.5	1018.7	0.15	-21.60	48.17
20180801-Al2024_TSA_MecaSurf-006-Glaze	1-Aug	Al 2024 TSA Mecasurf	1-Aug	Glaze	15:07	-4.6	Ø	29.50	30.0	Ø	978.8	1021.1	0.25	-4.54	81.02
20180801-Al2024_TSA_MecaSurf-007-Glaze	1-Aug	Al 2024 TSA Mecasurf	1-Aug	Glaze	15:38	-6.0	Ø	29.50	24.5	Ø	977.8	1020.1	0.25	-5.93	80.85
20180801-Al2024_TSA_MecaSurf-008-Glaze	1-Aug	Al 2024 TSA Mecasurf	1-Aug	Glaze	15:55	-5.0	Ø	29.90	32.5	Ø	977.5	1019.7	0.25	-4.94	80.92
20180801-Al2024_TSA_MecaSurf-009-Glaze	1-Aug	Al 2024 TSA Mecasurf	1-Aug	Glaze	16:07	-6.4	Ø	31.00	23.5	Ø	975.4	1018.5	0.25	-6.32	81.64
20180801-Al2024_TSA_MecaSurf-010-Glaze	1-Aug	Al 2024 TSA Mecasurf	1-Aug	Glaze	16:29	-5.4	Ø	31.00	25.1	Ø	975.2	1018.0	0.25	-5.33	81.52
20180801-Al2024_TSA_MecaSurf-011-Glaze	1-Aug	Al 2024 TSA Mecasurf	1-Aug	Glaze	16:43	-5.0	Ø	31.20	25.1	Ø	976.3	1018.4	0.25	-4.94	80.87
20180801-Al2024_TSA-012-Rime	1-Aug	Al 2024 TSA	1-Aug	Rime	17:09	-19.2	Ø	15.10	35.0	Ø	1001.2	1019.8	0.16	-19.10	51.88
20180801-Al2024_TSA-013-Rime	1-Aug	Al 2024 TSA	1-Aug	Rime	17:50	-19.8	Ø	17.00	38.5	Ø	999.5	1017.2	0.16	-19.70	50.60
20180801-Al2024_TSA-014-Rime	1-Aug	Al 2024 TSA	1-Aug	Rime	18:25	-20.6	Ø	17.00	38.5	Ø	999.8	1017.0	0.16	-20.50	49.80
20180802-Al2024_TSA-000-Rime	2-Aug	Al 2024 TSA	1-Aug	Rime	9:07	-20.3	Ø	15.45	37.5	Ø	1004.8	1022.5	0.16	-20.20	50.42
20180802-Al2024_TSA-001-Rime	2-Aug	Al 2024 TSA	1-Aug	Rime	10:13	-20.4	Ø	17.50	49.0	Ø	1004.6	1022.1	0.16	-20.30	50.13
20180803-Al2024_TSA-000-Rime	3-Aug	Al 2024 TSA	3-Aug	Rime	8:30	-20.1	20.3	16.10	44.5	Ø	1003.6	1021.7	0.16	-20.00	51.04
20180803-Al2024_TSA-001-Rime	3-Aug	Al 2024 TSA	3-Aug	Rime	9:48	-20.9	20.3	16.70	43.0	Ø	1003.9	1020.9	0.15	-20.80	49.38
20180803-Al2024_TSA-002-Rime	3-Aug	Al 2024 TSA	3-Aug	Rime	10:25	-20.5	20.3	17.65	43.0	Ø	1003.6	1021.5	0.16	-20.40	50.71
20180803-Al2024_TSA-003-Rime	3-Aug	Al 2024 TSA	3-Aug	Rime	10:58	-20.7	20.1	18.50	42.5	Ø	1003.9	1021.4	0.16	-20.60	50.12
20180803-Al2024_TSA-004-Rime	3-Aug	Al 2024 TSA	3-Aug	Rime	11:37	-20.7	20.0	18.30	43.5	Ø	1003.3	1021.4	0.16	-20.59	50.98
20180803-Al2024_TSA-005-Rime	3-Aug	Al 2024 TSA	3-Aug	Rime	13:32	-19.8	20.3	16.20	45.5	Ø	1003.2	1021.0	0.16	-19.70	50.65
20180803-Al2024_TSA-006-Glaze	3-Aug	Al 2024 TSA	3-Aug	Glaze	14:12	-5.0	19.8	30.10	19.0	Ø	981.0	1022.1	0.24	-4.94	79.73
20180803-Al2024_TSA-007-Glaze	3-Aug	Al 2024 TSA	3-Aug	Glaze	14:42	-5.0	20.3	30.00	26.0	Ø	982.0	1021.4	0.24	-4.94	78.05
20180803-Al2024_TSA-008-Glaze	3-Aug	Al 2024 TSA	3-Aug	Glaze	15:12	-5.7	20.0	31.50	23.0	Ø	980.0	1021.1	0.24	-5.63	79.67

Mach Number (Ma)	Static Temp. (T_{st})	Velocity (V)	Spray Time		Mass Flow Control - Volume of Water Sprayed [mL]			Test End Time (tf)	Spray N_2 Pressure	LWC	Type of Fracture (n)		Critical Pressure (σ_c)	Radis of Flaw (c)	Ice Thickness (h)	f-factor (f)	Energy of Fracture (FE)	Fracture Toughness (K_{1c})	Tensile Strength (σ_t)
	[°C]	[m/s]	Start	End	Nozzle 2	Nozzle 3	Nozzle 1		[bar]	[ccm]			[bar]	[mm]	[mm]		[J/m²]	[kPa√m]	[MPa]
-	-	-	17:59	18:10	Ø	Ø	Ø	Ø	2	2.5	Ø	Ø	Ø	Ø	Ø	-	-	-	-
-	-	-	15:30	15:48	Ø	Ø	Ø	Ø	2	2.5	Ø	Ø	Ø	Ø	Ø	-	-	-	-
-	-	-	16:50	17:10	Ø	Ø	Ø	Ø	2	2.5	Ø	Ø	Ø	Ø	Ø	-	-	-	-
-	-	-	Ø	Ø	Ø	Ø	Ø	Ø	2	6	Ø	Ø	Ø	Ø	Ø	-	-	-	-
-	-	-	Ø	Ø	Ø	Ø	Ø	Ø	2	6	Ø	Ø	8.2	4.0	15.0	-	-	-	-
-	-	-	Ø	Ø	Ø	Ø	Ø	Ø	2	6	Ø	Ø	27.1	4.0	15.0	-	-	-	-
-	-	-	Ø	Ø	Ø	Ø	Ø	Ø	2	6	Ø	Ø	12.4	4.0	15.0	-	-	-	-
-	-	-	17:19	17:22	Ø	Ø	Ø	Ø	2	6	Ø	Ø	5.248?	4.0	15.0	-	-	-	-
-	-	-	Ø	Ø	Ø	Ø	Ø	Ø	Ø	Ø	Ø	Ø	Ø	Ø	Ø	-	-	-	-
-	-	-	10:47	11:08	Ø	Ø	Ø	11:11	2	2.5	Adhesive	1.0	23.1	4.0	15.0	2.38	1.05	99.44	2.84
-	-	-	12:17	12:35	Ø	Ø	Ø	12:39	2	2.5	Adhesive	1.0	19.5	4.0	15.0	2.38	0.75	83.91	2.40
-	-	-	12:57	13:15	Ø	Ø	Ø	13:19	2	2.5	Adhesive	1.0	20.6	4.0	15.0	2.38	0.84	88.88	2.54
0.16	-20.80	49.56	13:27	13:45	Ø	Ø	Ø	13:47	2	2.5	Adhesive	1.0	17.5	4.0	15.0	2.38	0.61	75.49	2.16
0.15	-21.60	48.17	14:07	14:26	Ø	Ø	Ø	14:27	2	2.5	Cohesive	2.0	16.4	4.0	15.0	1.41	0.89	91.62	2.62
0.25	-4.54	81.02	15:27	15:33	Ø	Ø	Ø	15:35	2	6	Adhesive	1.0	37.2	4.0	15.0	2.38	2.74	160.58	4.59
0.25	-5.93	80.85	15:42	15:48	Ø	Ø	Ø	15:50	2	6	Adhesive	1.0	21.5	4.0	15.0	2.38	0.91	92.54	2.64
0.25	-4.94	80.92	15:58	16:04	Ø	Ø	Ø	16:05	2	6	Adhesive	1.0	37.1	4.0	15.0	2.38	2.72	160.02	4.57
0.25	-6.32	81.64	16:19	16:25	Ø	Ø	Ø	16:26	2	6	Adhesive	1.0	25.4	4.0	15.0	2.38	1.27	109.44	3.13
0.25	-5.33	81.52	16:33	16:39	Ø	Ø	Ø	16:40	2	6	Adhesive	1.0	14.9	4.0	15.0	2.38	0.44	64.31	1.84
0.25	-4.94	80.87	16:48	16:54	Ø	Ø	Ø	16:56	2	6	Adhesive	1.0	18.9	4.0	15.0	2.38	0.71	81.50	2.33
0.16	-19.10	51.88	17:24	17:43	Ø	Ø	Ø	17:46	2	2.5	Mixte	1.5	23.7	4.0	15.0	1.77	1.49	118.32	3.38
0.16	-19.70	50.60	18:00	18:18	Ø	Ø	Ø	18:22	2	2.5	Adhesive	1.0	58.9	4.0	15.0	2.38	6.85	253.87	7.25
0.16	-20.50	49.80	18:32	18:54	Ø	Ø	Ø	18:56	2	2.5	Adhesive	1.0	41.7	4.0	15.0	2.38	3.45	180.04	5.14
0.16	-20.20	50.42	9:46	10:06	Ø	Ø	Ø	10:07	2	2.5	Mixte	1.5	19.0	4.0	15.0	1.77	0.96	94.98	2.71
0.16	-20.30	50.13	10:28	10:48	49.67	49.67	49.67	10:49	2	2.5	Adhesive	1.0	11.0	4.0	15.0	2.38	0.24	47.54	1.36
0.16	-20.00	51.04	9:22	9:42	50.06	50.04	50.09	9:44	2	2.5	Adhesive	1.0	31.2	4.0	15.0	2.38	1.92	134.35	3.84
0.15	-20.80	49.38	9:59	10:19	50.03	50.01	49.91	10:21	2	2.5	Mixte	1.5	21.2	4.0	15.0	1.77	1.19	105.85	3.02
0.16	-20.40	50.71	10:34	10:55	49.67	49.70	49.70	10:55	2	2.5	Mixte	1.5	9.7	4.0	15.0	1.77	0.25	48.29	1.38
0.16	-20.60	50.12	11:07	11:26	49.38	49.39	49.39	11:28	2	2.5	Mixte	1.5	44.8	4.0	15.0	1.77	5.32	223.61	6.39
0.16	-20.59	50.98	11:50	12:10	50.06	50.05	50.03	12:11	2	2.5	Adhesive	1.0	50.7	4.0	15.0	2.38	5.09	218.75	6.25
0.16	-19.70	50.65	13:48	14:08	50.45	50.44	50.43	14:09	2	2.5	Adhesive	1.0	33.7	4.0	15.0	2.38	2.25	145.46	4.16
0.24	-4.94	79.73	14:29	14:37	50.93	50.79	50.75	14:38	2	6	Adhesive	1.0	33.4	4.0	15.0	2.38	2.21	144.15	4.12
0.24	-4.94	78.05	15:00	15:09	51.56	51.54	51.50	15:10	2	6	Adhesive	1.0	46.6	4.0	15.0	2.38	4.29	200.94	5.74
0.24	-5.63	79.67	15:35	15:43	50.02	50.02	50.02	15:44	2	6	Adhesive	1.0	31.5	4.0	15.0	2.38	1.96	135.73	3.88

Appendix F Technical Drawing of Mode I Test

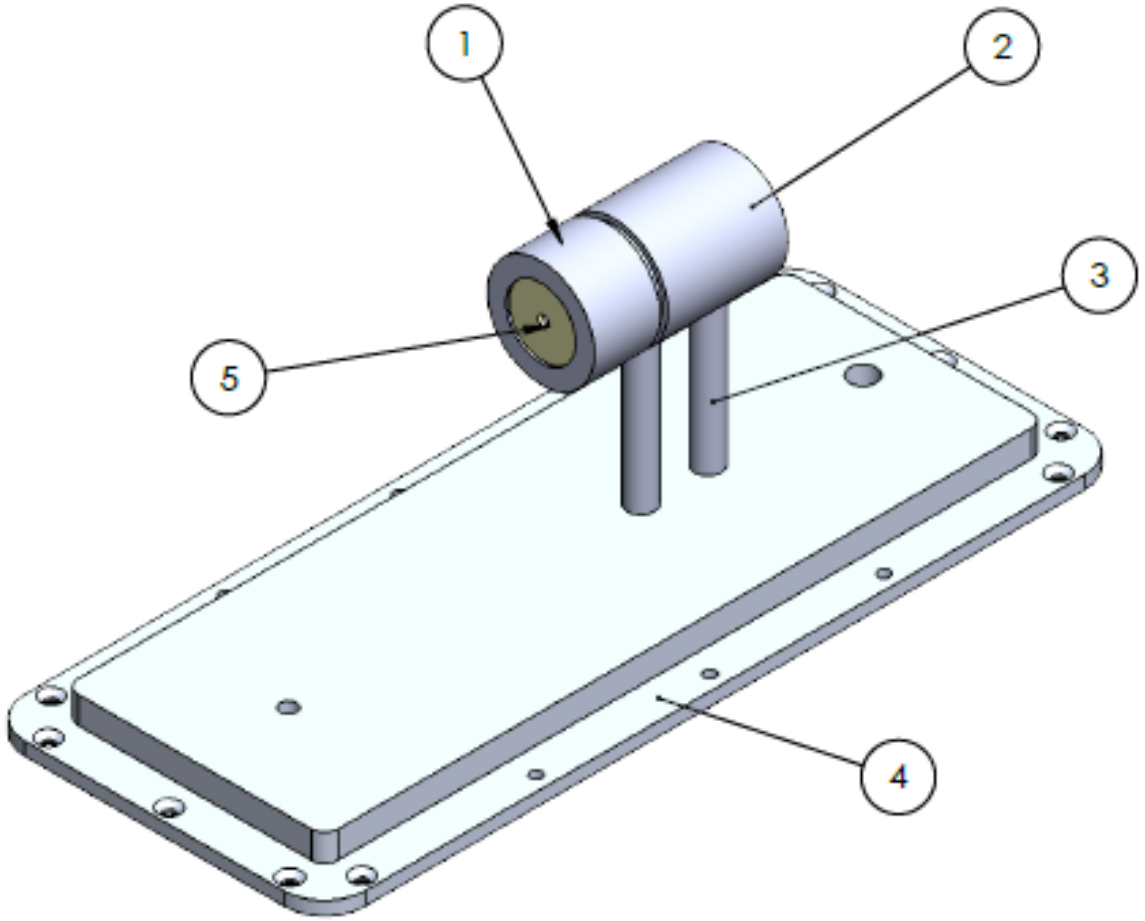

ITEM NO.	PART NUMBER	QTY.
1	12Cap1	1
2	12Substrate1	1
3	12Stand1	2
4	12Test Section Bottom	1
5	07Sample	1

UNLESS OTHERWISE SPECIFIED:

DIMENSIONS ARE IN MM
TOLERANCES:
FRACTIONAL ±
ANGULAR: MACH ± BEND ±
TWO PLACE DECIMAL ±
THREE PLACE DECIMAL ±

INTERPRET GEOMETRIC TOLERANCING PER:

MATERIAL

FINISH

DO NOT SCALE DRAWING

	NAME	DATE
DRAWN	GRASSO M.	19/06/18
CHECKED		
ENG APPR.		
MFG APPR.		
Q.A.		

COMMENTS:

iCORE

TITLE:

MODE I TEST

SIZE	DWG. NO.	REV
A	12Model Test	12

SCALE: 1:1 | WEIGHT: | SHEET 1 OF 6

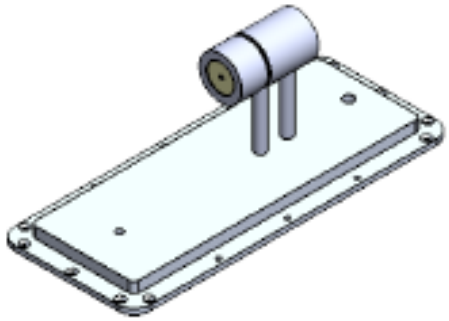

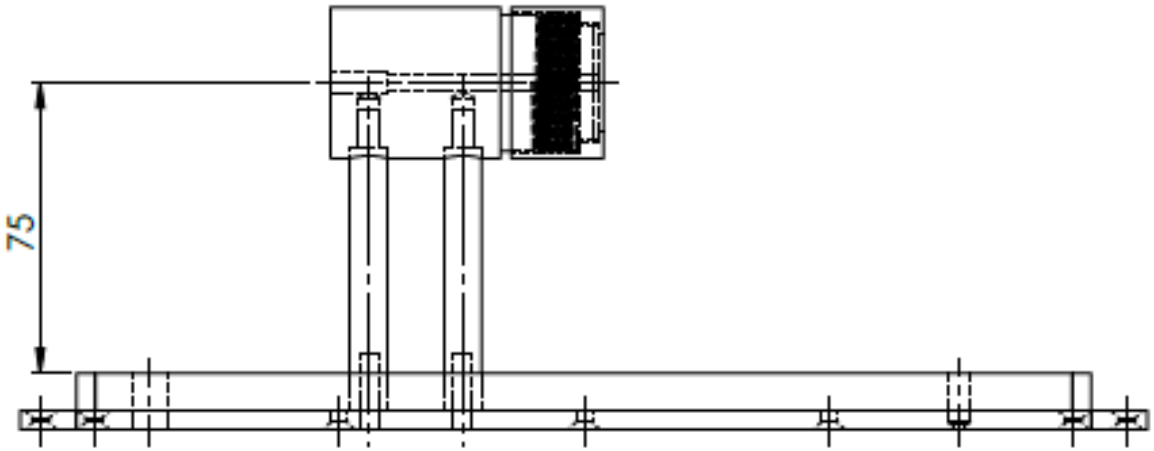

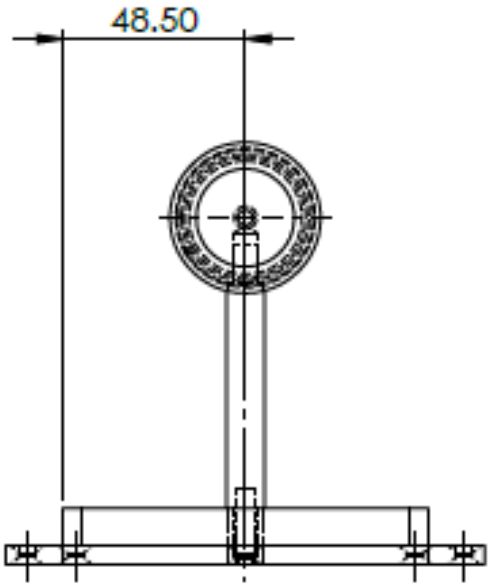

UNLESS OTHERWISE SPECIFIED:		NAME	DATE
DIMENSIONS ARE IN MM TOLERANCES: FRACTIONAL ± ANGULAR: MACH ± BEND ± TWO PLACE DECIMAL ± THREE PLACE DECIMAL ±	DRAWN	GRASSO M.	19/06/18
	CHECKED		
	ENG APPR.		
	MFG APPR.		
INTERPRET GEOMETRIC TOLERANCING PER:	Q.A.		
MATERIAL	COMMENTS:		
FINISH			
DO NOT SCALE DRAWING			

iCORE

TITLE:

MODE I TEST SAMPLE HOLDER

SIZE	DWG. NO.	REV
A	Test Assembly	12

SCALE: 1:2	WEIGHT:	SHEET 2 OF 6

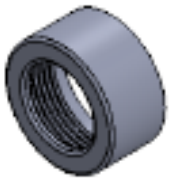

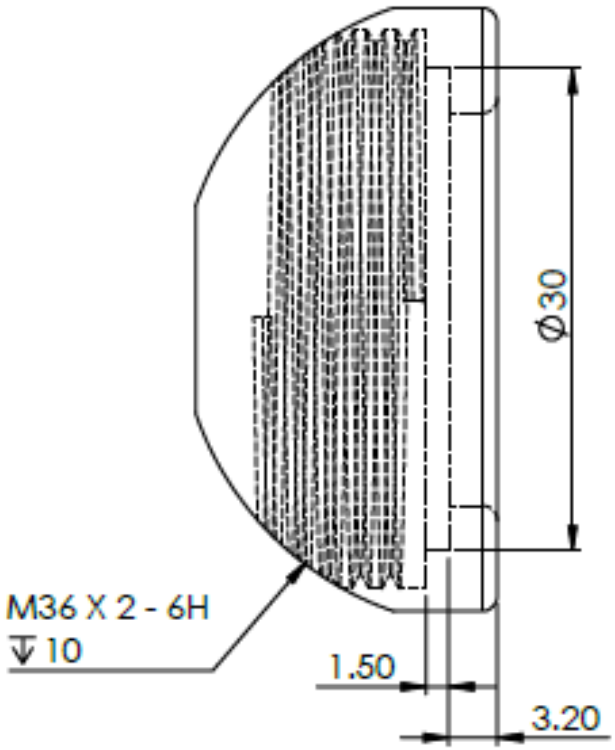

DETAIL A
SCALE 2 : 1

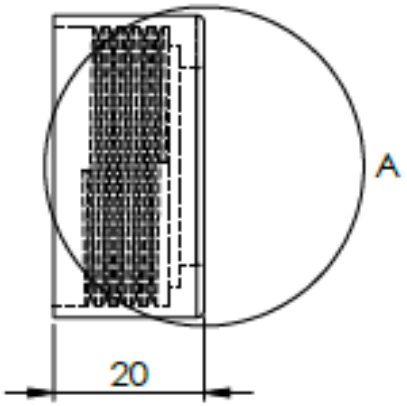

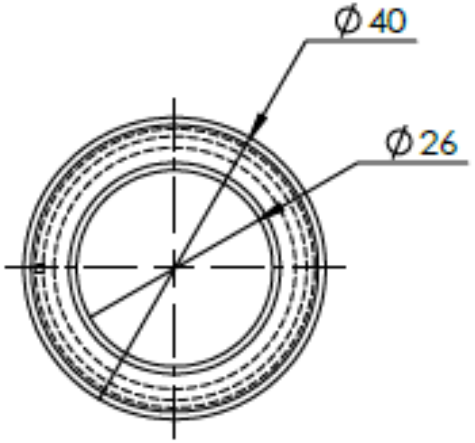

UNLESS OTHERWISE SPECIFIED:		NAME	DATE
DIMENSIONS ARE IN MM TOLERANCES: FRACTIONAL ± ANGULAR: MACH ± BEND ± TWO PLACE DECIMAL ± THREE PLACE DECIMAL ±	DRAWN	GRASSO M.	19/06/18
	CHECKED		
	ENG APPR.		
	MFG APPR.		
INTERPRET GEOMETRIC TOLERANCING PER:	Q.A.		
MATERIAL	COMMENTS:		
FINISH			
DO NOT SCALE DRAWING			

iCORE

TITLE:

MODE I TEST SAMPLE CAP

SIZE	DWG. NO.	REV
A	Cap	12

SCALE: 1:1	WEIGHT:	SHEET 3 OF 6

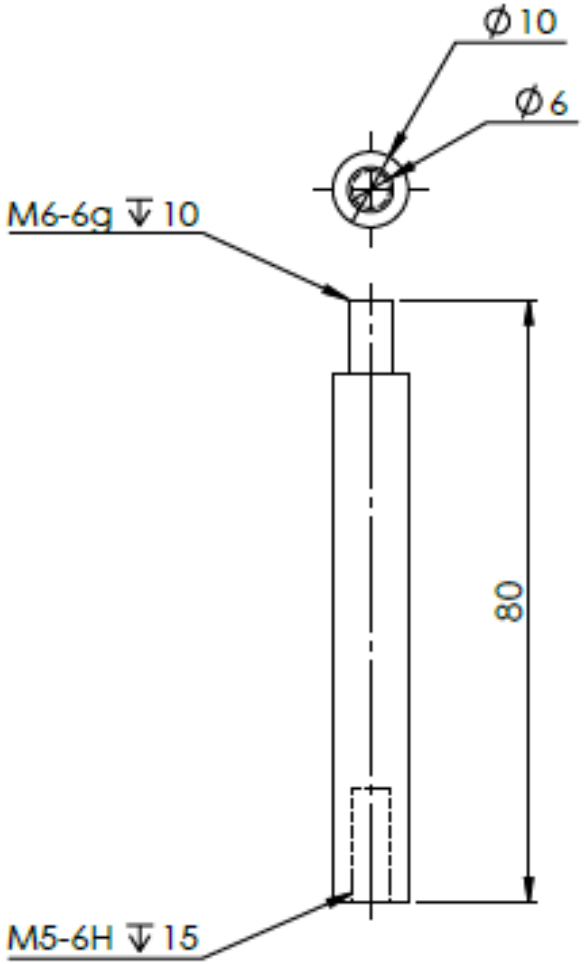

UNLESS OTHERWISE SPECIFIED:		NAME	DATE
DIMENSIONS ARE IN MM TOLERANCES: FRACTIONAL ± ANGULAR: MACH ± BEND ± TWO PLACE DECIMAL ± THREE PLACE DECIMAL ±	DRAWN	GRASSO M.	19/06/18
	CHECKED		
	ENG APPR.		
	MFG APPR.		
	Q.A.		
	COMMENTS:		
INTERPRET GEOMETRIC TOLERANCING PER:			
MATERIAL			
FINISH			
DO NOT SCALE DRAWING			

iCORE

TITLE:

MODE I TEST STAND

SIZE	DWG. NO.	REV
A	Stand	12

SCALE: 1:1	WEIGHT:	SHEET 4 OF 6

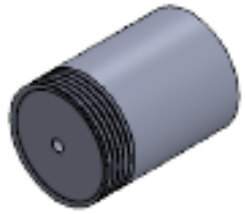

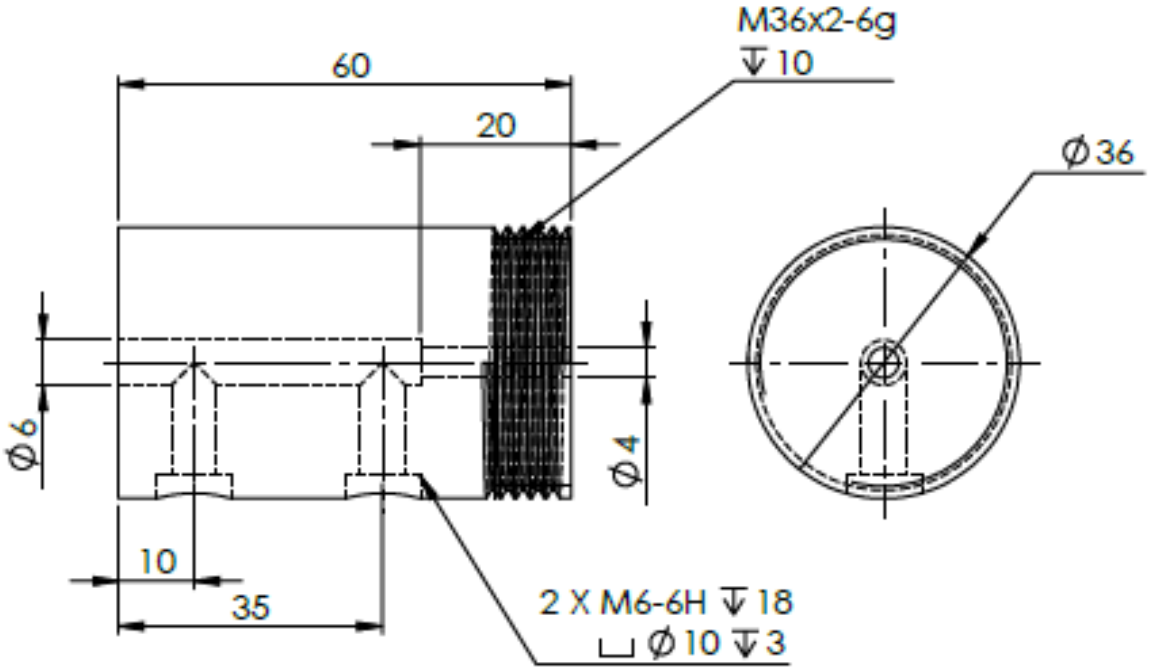

UNLESS OTHERWISE SPECIFIED:		NAME	DATE
DIMENSIONS ARE IN MM TOLERANCES: FRACTIONAL ± ANGULAR: MACH ± BEND ± TWO PLACE DECIMAL ± THREE PLACE DECIMAL ±	DRAWN	GRASSO M.	19/06/18
	CHECKED		
	ENG APPR.		
	MFG APPR.		
INTERPRET GEOMETRIC TOLERANCING PER:	Q.A.		
MATERIAL	COMMENTS:		
FINISH			
DO NOT SCALE DRAWING			

iCORE

TITLE:

MODE I TEST SAMPLE HOLDER

SIZE	DWG. NO.	REV
A	Holder	12

SCALE: 1:1	WEIGHT:	SHEET 5 OF 6

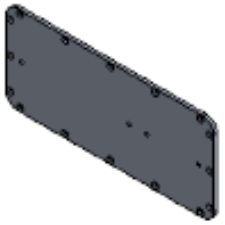

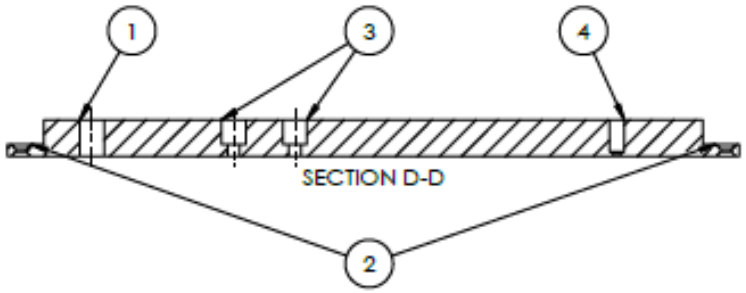

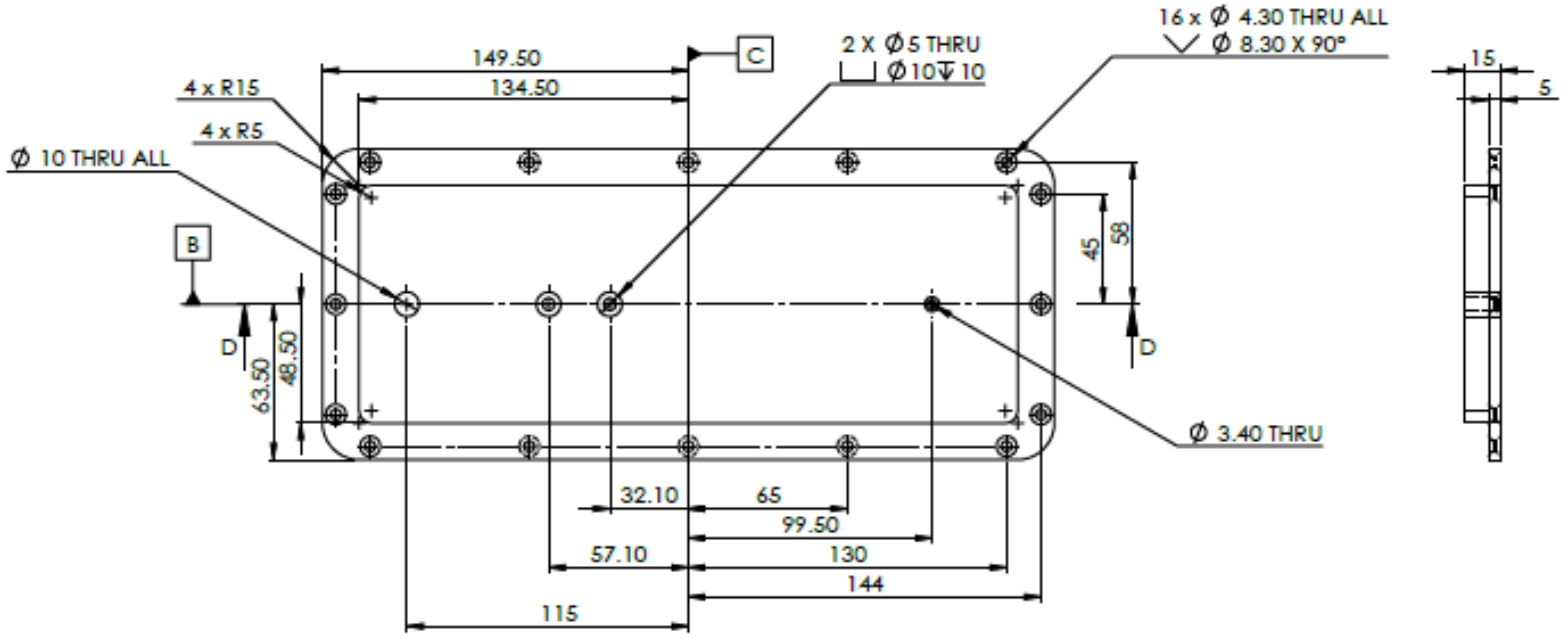

BOTTOM VIEW

1.THROU HOLE FOR CABLES
2.DOUBLE COUNTERSINK
3.COUNTERBORE FROM TOP
4.HOLE FOR PITOT TUBE INSERTION

UNLESS OTHERWISE SPECIFIED:		NAME	DATE
DIMENSIONS ARE IN MM TOLERANCES: FRACTIONAL ± ANGULAR: MACH ± BEND ± TWO PLACE DECIMAL ± THREE PLACE DECIMAL ±	DRAWN	GRASSO M.	19/06/18
	CHECKED		
	ENG APPR.		
	MFG APPR.		
INTERPRET GEOMETRIC TOLERANCING PER:	Q.A.		
	COMMENTS:		
MATERIAL POLYCABORNATE			
FINISH			
DO NOT SCALE DRAWING			

iCORE		
TITLE: MODE I TEST TEST SECTION WALL		
SIZE B	DWG. NO. TS Wall	REV 12
SCALE: 1:2	WEIGHT:	SHEET 6 OF 6

Appendix G Technical Drawing of iCORE Icing Wind Tunnel

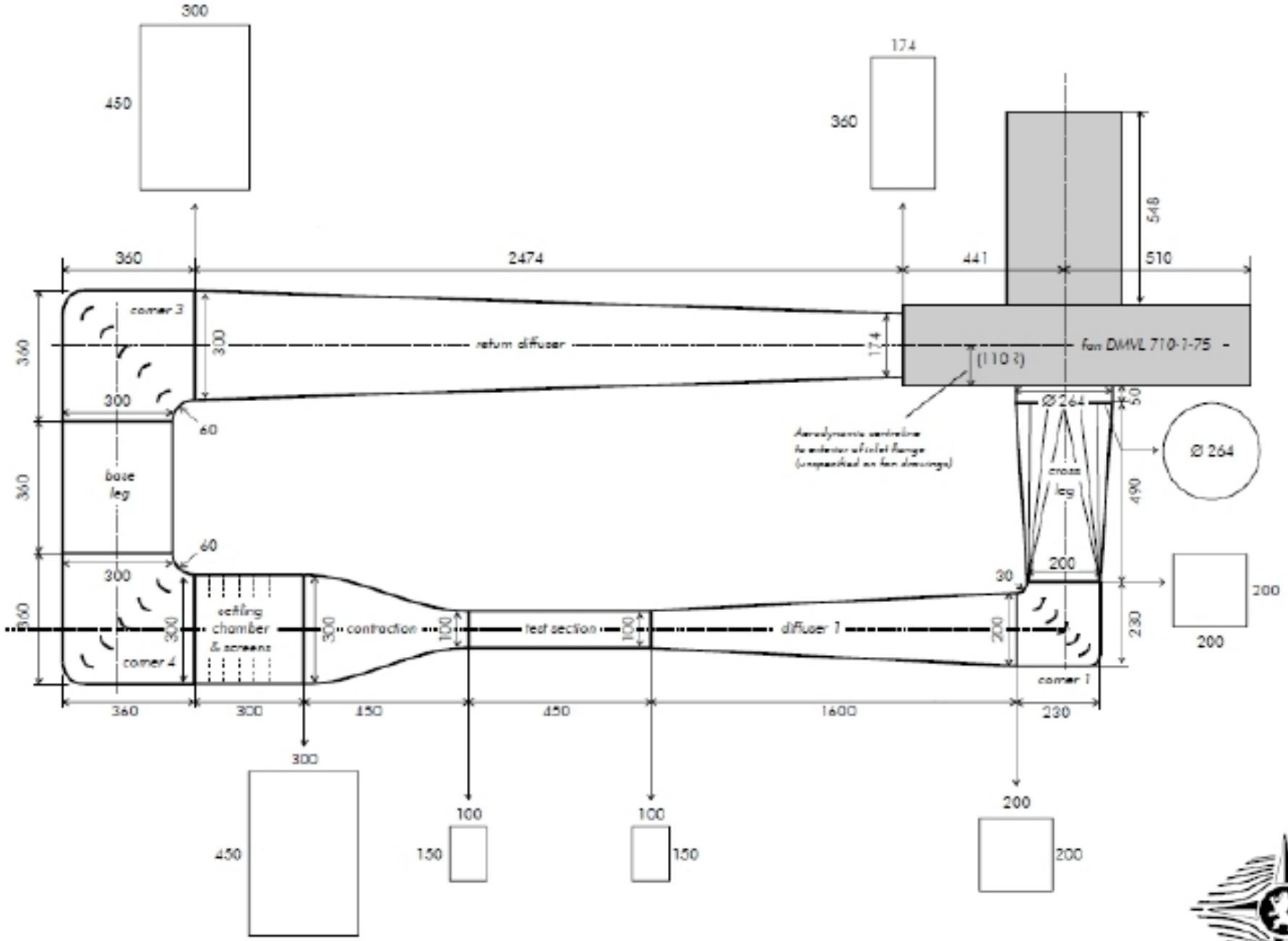

VKI Icing Tunnel for EADS

Aerodynamic layout (top view)

Overall dimensions (excluding insulation)

Excluding fan: 2840 mm x 1080 mm

Including fan: 3250 mm x 1590 mm

VON KARMAN INSTI
FOR FLUID DYNAM

Appendix H Centrifugal Fan MVDL-710-1-75 Specifications

▶ DMVL 710-1-75

MITTELDRUCK Hochleistungsventilator
MIDDLE-PRESSURE High Performance Fan

	DMVL 710-1-75 3-phasig
Volumenstrom / performance of air **Druckdifferenz Δ P_{fa} / pressure Δ P_{fa}**	**max 11800 m³/h** **max 9000 Pa**
Motor-Nennleistung / power out	22 kW
Nennspannung / voltage	Δ 400 V
Nennstrom / current	42 A
Nenndrehzahl / speed	2940 min⁻¹
Frequenz / frequency	50 Hz
Schutzart IP / protection mode IP	55
Schalldruckpegel / noise level	109 dB (A)
Gewicht / weight	ca. 221 kg

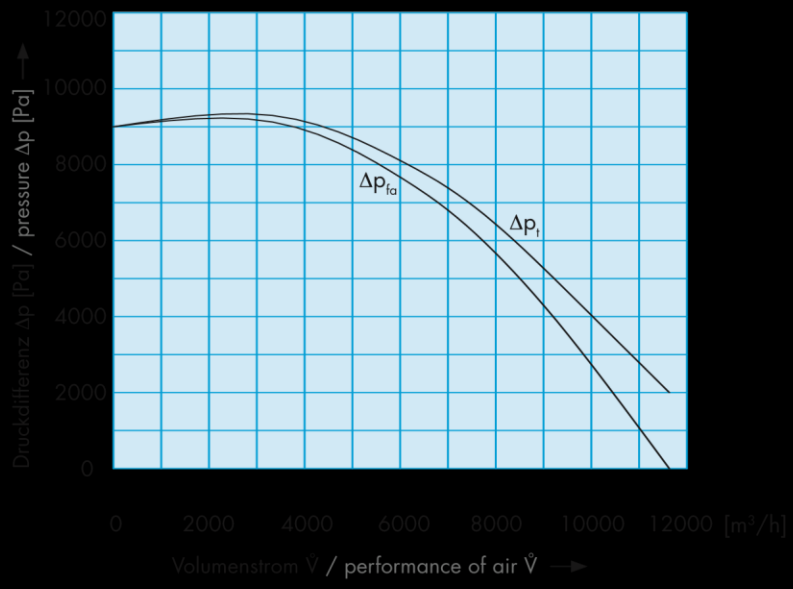

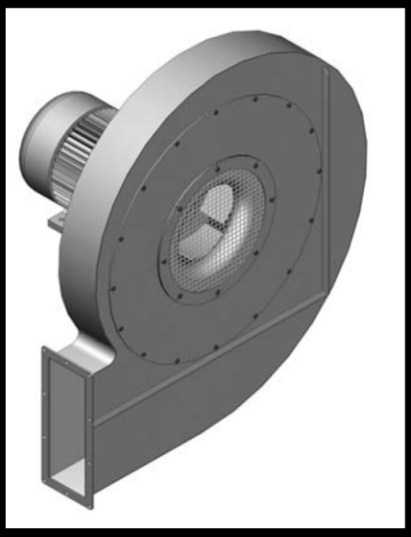

Abmessungen / Measurements

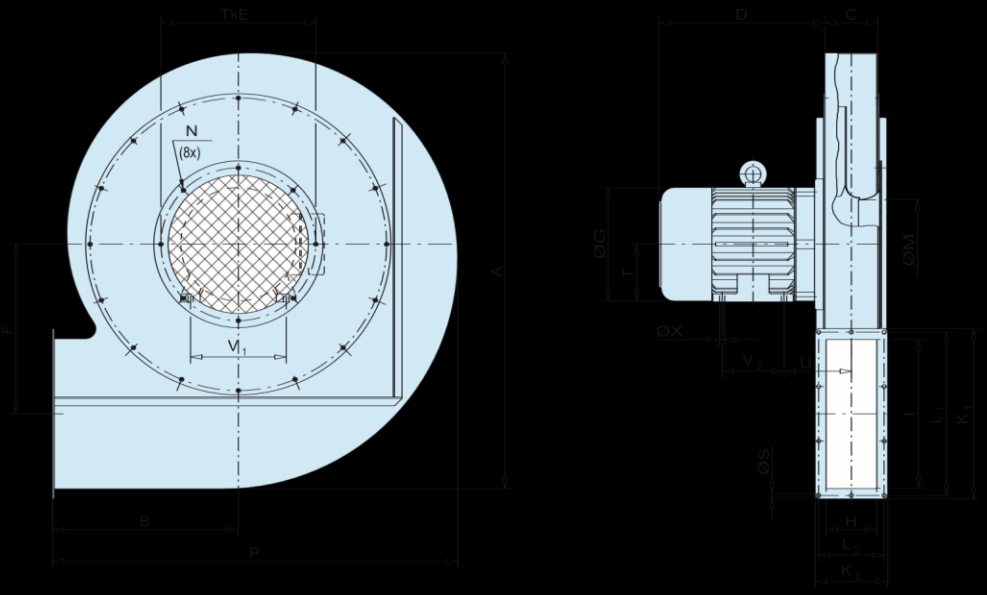

A	1027
B	441
C	180
D	548
E	350
F	387
G	315
H	174
I	360
K1	440
K2	250
L	405/135
L2	220
M	220
N	M6
P	951
S	14
T	160
U	201
V1	254
V2	154
X	14

Appendix I Pitot Static PAA-8-KL

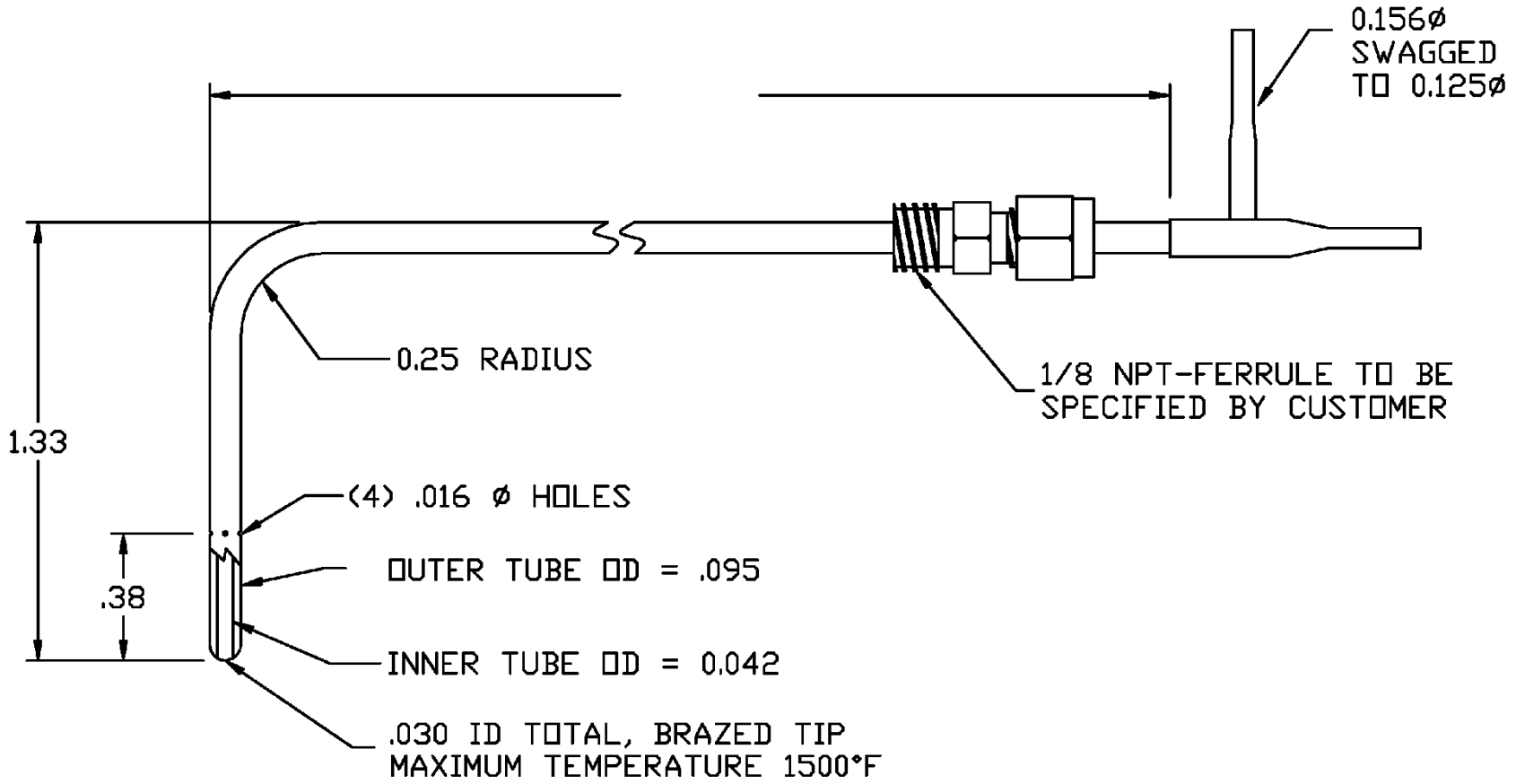

UNLESS OTHERWISE SPECIFIED:
DIMENSIONS ARE IN INCHES
TOLERANCES
DECIMALS ANGULAR
.XX ± .05 ± 0.5°
.XXX ± .010
DO NOT SCALE DRAWING

DRAWN	GD	DATE 022102
CHECKED	CAR	030499
DESIGN		

United Sensor Corp

PAB- -KL

SIZE	DWG NO.	REV
B	PAB- -KL CUST.dwg	

SCALE | SHEET OF

Appendix J Pressure Transmitter

Pressure Transmitter
With Voltage Output (3-wire)
PT160R-2004-U1-H1141

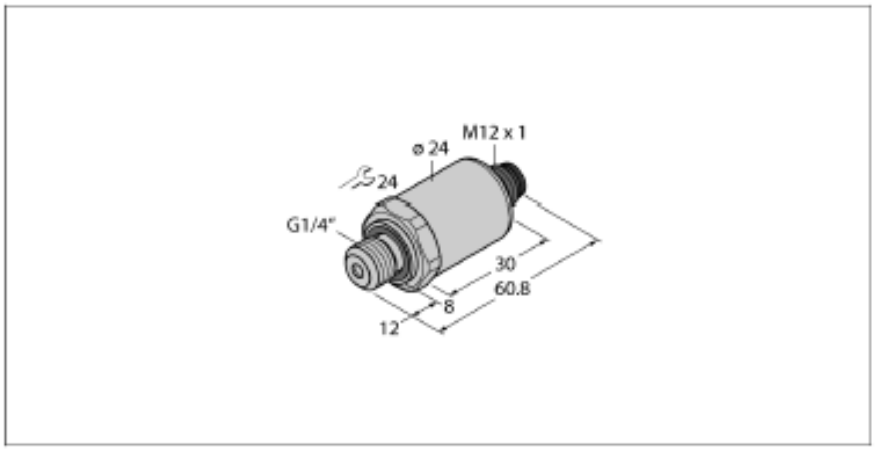

- **Completely welded measuring cell**
- **Compact and robust design**
- **Excellent EMC properties**
- **Pressure range 0...160 bar rel.**

Wiring Diagram

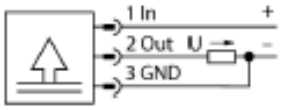

Type designation	PT160R-2004-U1-H1141
Ident no.	6836543
Pressure range	
Relative pressure	0...160 bar rel. 0...2321 psi 0...16 MPa
Admissible overpressure	≤ 480 bar
Burst pressure	≥ 960 bar
Response time	< 2 ms, typ. 1 ms
Long-term stability	0.25% FS, , acc. to EN 60770-1
Power supply	
Operating voltage	12...33 VDC
Current consumption	≤ 7 mA
Short-circuit/reverse polarity protection	yes / yes
Protection type and class	IP67 / III
Insulation voltage	750 VDC
Outputs	
Output 1	Analog output
Analog output	
Voltage output	0...10V
Operating range	0...10 V (3-wire)
Load	≥ 10 kΩ
Accuracy LHR analog output	± 0.3 % FS BSL
Temperature behaviour	
Medium temperature	-40...+135 °C
Temperature coefficient	± 0.2 % of full scale/10 K
Ambient conditions	
Ambient temperature	-30...++85 °C
Storage temperature	-50...+100 °C
Vibration resistance	20 g, 15...2000 Hz, 15...25 Hz with amplitude +/-15 mm acc. to IEC 68-2-6
Shock resistance	100 g, 11 ms, half sinusoidal curve, all 6 directions, free fall from 1 m onto concrete (6x) , according to IEC 61508

Functional principle

The pressure sensors of the PT ...-2000 series operate with a fully welded metal measuring cell. Depending on the sensor type used, the processed signal is available as analog output of either 4...20 mA (2-wire) or 0...10 V (3-wire).

Edition • 2018-05-21T 10:18:40-02:00

Pressure Transmitter
With Voltage Output (3-wire)
PT160R-2004-U1-H1141

Housing	
Housing material	Stainless-steel/Plastic, Stainless steel V4A (1.4404)/ Polyacrylamide 50% GF UL 94 V-0
Pressure connection material	Stainless steel V4A (1.4404)/AISI 316L
Pressure transducer material	Stainless steel 1.4435/AISI 316L
Sealing material	FPM
Process connection	G¼" male thread
Wrench size pressure connection / coupling nut	SW 24
Electrical connection	Connectors, M12 × 1
Max. tightening torque housing nut	20 Nm
Reference conditions acc. to IEC 61298-1	
Temperature	15…+25 °C
Atmospheric pressure	860…1060 hPa abs.
Humidity	45…75 % rel.
Auxiliary power	24 VDC
MTTF	1238 years acc. to SN 29500 (Ed. 99) 40 °C

Edition • 2018-05-21T 10:18:40-02:00

Appendix K Compact Multiprotocol I/O Module for Ethernet

Compact Multiprotocol I/O Module for Ethernet
4 Analog Inputs, Configurable as Voltage, Current, RTD or Thermocouple
TBEN-S2-4AI

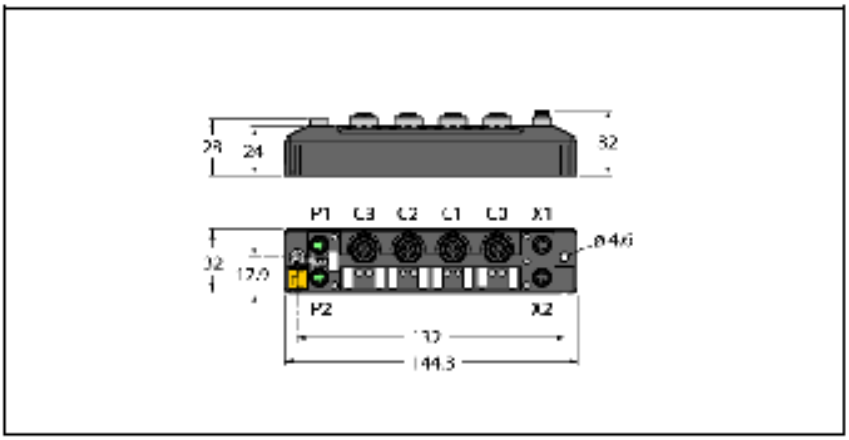

- PROFINET® device, EtherNet/IP™ device or Modbus® TCP slave
- Integrated Ethernet switch
- Supports 10 Mbps/100 Mbps
- 2x M8, 4-pin, Ethernet fieldbus connection
- Glass fiber reinforced housing
- Shock and vibration tested
- Fully potted module electronics
- Protection classes IP65, IP67, IP69K
- Male M8, 4-pin, for power supply
- Each channel can be selected for voltage, current, RTD, resistance or thermocouple
- Ranges:
- Voltage: +/-500 mV, +/-100 mV, +/-50 mV, +/-1 V, 0/1-5 V, +/-10 V, 0/2-10 V
- Current: 0/4 ... 20 mA, +/-20 mA
- RTD: PT100, NI100, PT200, PT500, PT1000, NI1000
- Resistance: 0-100 Ω/200 Ω/400 Ω/1 kΩ/4 kΩ
- Thermocouples: Type B, C, E, G, J, K, N, R, S, T
- Inputs differential or common reference
- FLC/ARGEE programmable

Type designation	TBEN-S2-4AI
Ident no.	6814025
Supply	
Supply voltage	24 VDC
Admissible range	18...30 VDC Total current max. 4 A per voltage group V1
Voltage supply connection	2 x M8, 4-pin
Operating current	V1: min. 100 mA, max. 240 mA mA
Sensor/Actuator supply V_{aux}	supply of ports C0-C3 from V1 short-circuit proof, max. 1 A for group C0-C3
Electrical isolation	galvanic isolation of the voltage groups V1 and V2, voltages up to 500 VAC
System data	
Fieldbus transmission rate	10 Mbps/100 Mbps
Fieldbus connection technology	2 x M8, 4-pin
Protocol detection	automatic
Web server	default: 192.168.1.254
Service interface	Ethernet via P1 or P2
Field Logic Controller (FLC)	
Supported from firmware version	3.1.2.0
Released from ARGEE version	2.0.25.0
Modbus TCP	
Addressing	Static IP, BOOTP, DHCP
Supported function codes	FC1, FC2, FC3, FC4, FC5, FC6, FC15, FC16, FC23
Number of TCP connections	8
Input register start address	0 (0x0000 hex)
Output register start address	2048 (0x0800 hex)
EtherNet/IP™	
Addressing	acc. to EtherNet/IP™ specification
Quick Connect (QC)	< 500 ms
Device Level Ring (DLR)	supported
Class 3 connections	3
Class 1 connections	10
Input Assembly Instance	103
Output Assembly Instance	104
Configuration Assembly Instance	106

Edition • 2018-05-21T07:27:07.+02:00

Compact Multiprotocol I/O Module for Ethernet
4 Analog Inputs, Configurable as Voltage, Current, RTD or Thermocouple
TBEN-S2-4AI

PROFINET	
Addressing	DCP
Conformance class	B (RT)
MinCycleTime	1 ms
Fast Start-Up (FSU)	< 500 ms
Diagnostics	acc. to PROFINET alarm handling
Topology detection	supported
Automatic addressing	supported
Media Redundancy Protocol (MRP)	supported

Analog Inputs	
Number of channels	4
Operating modes	Voltage, current, RTD, resistance, thermocouple
Resolution	16 bit

Operating mode voltage	
Input filter	standard, smooth, fast, off
Max. input voltage	11.85 V
Load resistance	100 KΩ
Input signal types	differential, differential without ground, single ended
Measuring range	0…10 V, +/-10 V, 2…10 V, 0…5 V, 1…5 V, +/-1 V +/-500 mV, +/-100 mV, +/-50 mV
Mains suppression	no, ≤ 50 Hz, 60 Hz
Cycle time	4 ms
Basic error at 25 °C	< 0.1 %
Repeat accuracy	< 0.015 %
Temperature coefficient	< 100 ppm/°C of full scale
Measurement error total (FSR)	≤ 0.75%

Operating mode current	
Input filter	standard, smooth, fast, off
Max. input current	23 mA
Load resistance	50 Ω
Input signal types	differential, differential without ground, single ended
Measuring range	0…20 mA, 4…20 mA, +/-20 mA
Mains suppression	no, ≤ 50 Hz, 60 Hz
Cycle time	4 ms
Basic error at 25 °C	< 0.1 %
Repeat accuracy	< 0.015 %
Temperature coefficient	< 100 ppm/°K of full scale
Measurement error total (FSR)	≤ 0.75 %

Operating Mode RTD/Resistance	
Temperature scale	°Celsius, °Fahrenheit
Measuring range	Pt100 -200 °C…850 °C, Pt100 -200 °C…150 °C *2) Pt200 -200 °C…850 °C*3)*4), Pt200 -200°C…150 °C Pt500 -200 °C…850 °C*1), Pt500 -200°C…150 °C*3)*4) Pt1000 -200 °C…850 °C,Pt1000 -200 °C…150 °C*1) Ni100 -60 °C…250 °C*2), Ni100 -60°C…150 °C*2)*4) Ni1000 -60 °C…250 °C*2)*4), Ni1000 -60 °C…150° C *4) 0…100 Ω *2), 0…400 Ω, 0…2 kΩ, 0…4 kΩ
Connection type	2-wire, 3-wire, 4-wire
Input filter	standard, smooth
Cycle time	400 ms
Basic error at 25 °C	< 0.2 % *1) < 0.3 % 2-wire, *2) < 0.3 %, 3-wire, *3) < 0.3 %, 4-wire, *4) < 0.7 % 2-wire
Repeat accuracy	< 0.015 %
Temperature coefficient	< 100 ppm/°C of full scale
Measurement error total (FSR)	< 0.85 % *1) < 0.95 % 2-wire, *2) < 0.95 %, 3-wire, *3) < 0.95 %, 4-wire, *4) < 1.35 %, 2-wire

Edition • 2018-05-21T07:27:07+02:00

Appendix L Compact Power Supply Module in IP67

Compact power supply module in IP67
24 VDC output voltage - 3.8 A output current
PSU67-11-2440/P

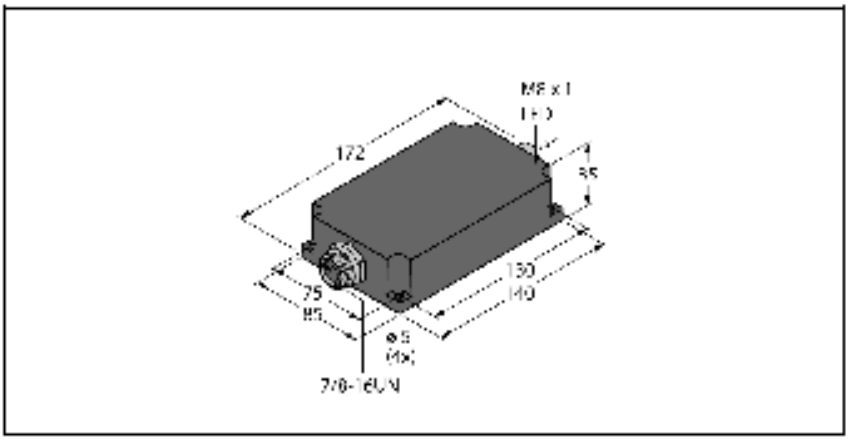

- Broad temperature range
- Status LED
- AC and DC wide-range input
- Mains buffering up to 50 ms
- High efficiency
- No-load and short-circuit proof
- Natural air cooling

7/8" Input Assignment

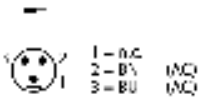

M8 × 1 Output

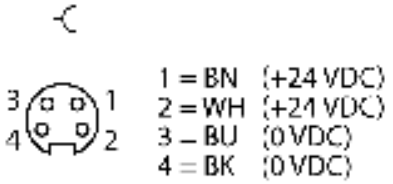

Characteristic

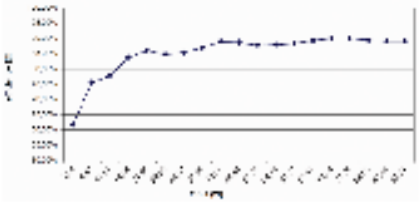

Type designation	PSU67-11-2440/P
Ident no.	6884257
Nominal voltage	Universal voltage supply unit
Operating voltage	100…240 VAC
Frequency	50…60 Hz
Operating voltage range	100…300 VDC
Power consumption	≤ 104 VA
Power dissipation, typ.	≤ 11 W
Mains buffering	UI: 100…240 VAC/ 50 ms
Nominal output voltage	24 V
Nominal current	3.8 A
Overload protection	105-130 %
Parallel mode	no
Ripple	240 mV
Short-circuit behaviour	Current limiting
Approval	CE-compliant UL-certified RoHS-compliant Safety extra low voltage (SELV) according to IEC/ EN 60950-1: 2016 + A11: 2009 + A1: 2010 + A12: 2011 + A2: 2013 (safety of information technology equipment) EN 61000-6-2: 2005 (interference immunity) EN 61000-6-3: 2007 + A1: 2011 (emitted interference) EN 61000-3-2: 2006 + A1: 2009 + A2: 2009 (harmonic)
Operational readiness	LED green
Protection class	IP67
Ambient temperature	-25…+60 °C
Storage temperature	-40…+85 °C
Derating	2 % / K (50 °C)
Dimensions	85 x 172 x 35 mm
Weight	840 g
Housing material	Glass fiber reinforced polyamide (PA6-GF25)
Electrical connection	Connectors
MTTF	87 years
MTTF note	acc. to SN 29500 (Ed. 99) 40 °C

Edition • 2018-05-21T12:38:52+02:00

Appendix M Calculation of Nitrogen Leaks

Under normal conditions, nitrogen air is a colorless, odorless, tasteless, non-irritating, non-inflammatory and an inert (non-reactive) gas, which means that it generally does not react with other substances. Even though nitrogen gas accounts for 78% of the air we breathe, it can be a life-threatening since there is no a way to smell, see, or hear the gas. People working with this gas are not warned of the presence of the acceptable nitrogen molecules. The potential hazard of working with nitrogen is that it can decrease the oxygen level below the required amount of oxygen that a human brain needs to remain active. When the brain has insufficient oxygen supply, it does not function properly and shuts down. The safety risks are suffocation, hyperthermia and the hazards associated with handling high pressure containers.

AIRBUS

Statement

Wind tunnel experiment with nitrogen

Date: 05.06.2018

Building 77 E, XRXG Surface Engineering

Nicola Tabertshofer (HAHTG4)

Question

For experiments in the wind tunnel, pressurized nitrogen is needed. It is provided in a gas cylinder by Linde (Genie® bottle, volume: 20 L, pressure: 300 bar). The experiment takes place in a wind tunnel (closed system). No parts, that are blown off, can escape from the wind tunnel.

Guidelines from EHS

- The supplier, Linde, shoud connect the gas cylinder with the experimental setup and check the functionality. This should be documented.
- Before working with the experimental setup, the employee(s) has to be instructed about the dangers and countermeasures.
- No oxygen warning device is needed. Even in the worst case scenario (all nitrogen is released at once) the level of oxygen is sufficient (see calculations).
- The gas cylinder doesn't have to be secured with chains (TRGS 510). Nervetheless it should not block any emergency exits or narrow down walkways.
- The risk assessment has to be updated by the responsible manager

AIRBUS

The calculation of percentage of oxygen in the air after release of cylinder gas

In the event of catastrophic failure of the cylinder tank where the total volume of Nitrogen is released in the room in a very short time, the oxygen concentration in the room can be calculated by:

$$\%O_2 = \frac{V_o}{V_r} x100\%$$

Where, for nitrogen air:

$V_g = Maximum\ volume\ of\ gas\ released\ (m^3)$

$V_o = Volume\ of\ oxygen\ (m^3)$

$V_r = Volume\ of\ room\ (m^3)$

$V_r = area\ x\ height$

$V_r = 48.10\ m^2\ x\ 4\ m$

$V_r = 192.40\ m^3$

$$V_g = volume\ of\ gas\ cylinder\ (L)\ x\ \frac{1\ m^3}{1000\ L}$$

$$V_g = 20.00\ L * 300\ bar * \frac{1\ m^3}{1000\ L} = 6\ m^3$$

$V_o = fraction\ of\ oxygen\ in\ air\ (volume\ of\ the\ room - volume\ of\ nitrogen\ liberated)$

$V_o = 0.2095(V_r - V_g)$

$V_o = 0.2095(192.40\ m^3 - 6\ m^3)$

$V_o = 39.05\ m^3$

$$\%\ \boldsymbol{O_2} = \frac{\boldsymbol{39.05\ m^3}}{\boldsymbol{192.40\ m^3}} * \boldsymbol{100}\ \% = \boldsymbol{20,3}\ \%$$

Appendix N Tartaric Sulphuric Acid (TSA) Anodizing Procedure

1 Introduction

REACH compatible sealing steps for Al alloys that enhance the corrosion resistance of TSA layers by closing the oxides is subject of this report. Today standard Cr-IV-containing chemical surface treatment processes need to be substituted by environmental friendly alternatives. The two-step sealing of TSA using SurTec 650 (Cr-III) as sealing agent and posttreatment with hot water have already shown sufficient corrosion protection. Based on the satisfying results modified parameter sets as well as the alternative sealing product Lanthane (Cr-III) are in the focus of this work.
After the different sealing treatment procedures, the corrosion resistances have been tested by SST and SEM analysis.

2 Anodizing and sealing

The anodization, surface preparation and sealing procedures was carried out as follows and is described more in detail in [1].

Pre-treatment: according to 80-T-35-2010 / AIPI 02-01-003

1. Alkaline degreasing/cleaning with Metaclean T2001 for 15 min at 65 °C (acc. to 80-T-35-0020)
2. Intermediate rinsing in deionized water for 3 min
3. Alkaline etching with P3 Almeco 51 for 5 min at 35 °C (acc. to 80-T-35-0110)
4. Intermediate rinsing in deionized water for 3 min
5. Acidic pickling with Turco Liquid Smutgo for 3 min at 40 °C (acc. to 80-T-35-0100)
6. Intermediate rinsing in deionized water for 3 min

TSA-treatment: according to AIPS 02-02-003 (37 °C, 25 min in TSA-bath at 14 V (5 min ramp-up). During the anodizing process, due to the rectifier, the Voltage only raises until a value of 13.2 V and not as expected (and set up) to 14 V.
Afterwards: Rinsing in deionized water for 15 min.

Sealing:
SurTec ChromitAl 650

1. 34 °C for 6 min
2. 34 °C for 10 min
3. 30 °C for 6 min

} + 30 min hot water sealing at 98 °C

Lanthane

1. 20 °C for 3 min
2. 30 °C for 6 min
3. 35 °C for 10 min

} + 30 min hot water sealing at 98 °C

Appendix O MecaSurf/EpiSurf® Procedure

AIRBUS

MecaSurf/EpiSurf® Procedure

The French company, Surfactics, have developed commercially available coatings that when applied reduces the surface tension of the material; thus, it can make a surface more hydro-/oil-phobic. Prior applying a coating of MecaSurf/EpiSurf®, the surface must be activated using plasma technology. Plasma is defined as a state of matter which is not found in natural conditions as the other states (solid, liquid, and gas). It can be forced to exist by heating or exposing a gas in an electromagnetic field; consequently the gas becomes electrically conductive.

Sample Cleaning

1. Clean samples in ultrasonic bath
   a. 15min in Acetone
   b. Dry with nitrogen (N_2) flow
   c. 15min in Ethanol
   d. Dry with nitrogen (N_2) flow
   e. 15min in Water
   f. Dry with nitrogen (N_2) flow

Figure 1: SONOREX UltraSonic Bath.

Surface Activation

1. Turn on power supply (modules under PC cabinet)
2. Log in to EADS account (no password is required)
3. Turn on pressurized air source (valve on wall near corner opposite entrance door of the lab) for the air suction and pressurized lever situated at the left of the plasma allowing air flowing through the nozzle
4. Turn on power supplies of the robotic arms (green switch and green 'power' button on the two modules at the bottom of the PC tower)

Figure 2: Power Suply Modules.

AIRBUS

5. Open software ProNC
6. Install samples
   a. Can use spacers to insure a 1cm height distance between top surface of sample and nozzle tip (if the sample is a metallic)
   b. In the case of a polymer sample, the distance should be higher
7. Switch on module of plasma (red knob on cabinet to left of PC)
8. After closing door of plasma cabinet, push green button 'ein' of plasma module
9. Use the program to move the nozzle
10. Turn on nozzle with switch on black box
11. To remove samples, push red button of the plasma module and wait until the voltage decreases to zero
12. Turn off:
    a. all modules under PC cabinet
    b. power supply for vacuum system
    c. pressurized air source
    d. plasma module
    e. PC

Figure 3: Plasma Control Unit.

Figure 4: Plasma Generator in the Chamber.

Application

1. *(Ideal for EpiSurf)* Dip samples in a recipient with MecaSurf for 5min and shake the sample regularly to insure a proper adhesion of the coating to the surface

or

2. *(Ideal for MecaSurf)* Spray samples with MecaSurf bottle

Appendix P Ti02 Nanotubes Procedure

AIRBUS

TiO2 – Nanotubes for Ti6Al4V or Cp Ti

MANUAL DEGREASING (IPA)

↓

ALKALINE DEGREASING
(P3-Almeco-18) 65°C, 15min, stirring

↓

Intermediate rinsing
(Class A AIMS09-00-003) RT, 5min

↓

ACIDIC ETCHING (HF/HNO_3)
RT, 1min, stirring (optional)

↓

1st intermediate rinsing
(Class A AIMS09-00-003) RT, 3min

↓

2nd intermediate* rinsing
(Class A AIMS09-00-003) RT, 5min

**To be done, especially if 1st rinsing bath is not completely fresh*

ALKALINE ETCHING (Turco 5578)
95°C, 5min, stirring

↓

1st intermediate** rinsing
(Class A AIMS09-00-003) RT, 5min

↓

ULTRASONIC CLEANING (Class A AIMS09-00-003) RT, 3 times, 1min

***To be done in an extra bucket, not to pollute the ultrasonic bath water*

↓

ANODISING (TiO2-Nanotubes)
30°C, 20V, 35min (1min ramp-up, 1min ramp-down), current self-adjusting

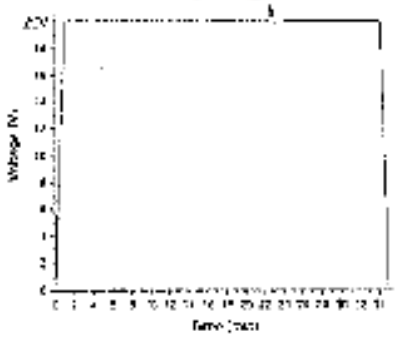

↓

Final rinsing
(Class A AIMS09-00-003) RT, 5min

↓

ULTRASONIC CLEANING (Class A AIMS09-00-003) RT, 3 times, 1min

To be done In order to open the tubes, otherwise, there will be Titanium blocking them

↓

DRYING
Heat flow, 60°C, 20-30min

Appendix Q Surface Roughness Parameters

Roughness measuring systems from Jenoptik – Surface parameters in practice

Selection of the cut-off (profile filter) according to ISO 4288:1998 and ISO 3274:1998

The cut-off is selected depending on the workpiece surface either according to the valley spacing or the expected roughness values. At the same time the total evaluation length and the corresponding traverse length are defined according to the standards. Deviations are necessary if the workpiece does not allow the required traverse length. See drawing entries.

Periodic profiles
e.g. turning, milling

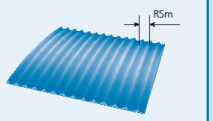

Measuring conditions

lr	sampling length
ln	evaluation length
lt	traverse length
λc	cut-off
λs	shortwave profile filter
r_{tip}	stylus tip radius
ΔX	digitization distance [1]

1) The digitization distance is also standardized. This is set automatically by most roughness measuring instruments.

Aperiodic profiles
e.g. grinding, eroding

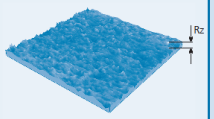

RSm (mm)	λc = lr (mm)	ln (mm)	lt (mm)	r_{tip} (µm)	λs (µm)	Ra (µm)	Rz (µm)
> 0.013 ...0.04	0.08	0.4	0.48	2	2.5	> (0.006) ...0.02	> (0.025) ...0.1
> 0.04 ...0.13	0.25	1.25	1.5	2	2.5	> 0.02 ...0.1	> 0.1 ...0.5
> 0.13 ...0.4	0.8	4	4.8	2 or 5 *	2.5	> 0.1 ...2	> 0.5 ...10
> 0.4 ...1.3	2.5	12.5	15	5	8	> 2 ...10	> 10 ...50
> 1.3 ...4	8	40	48	10	25	> 10 ...80	> 50 ...200

Application example

In a periodic profile the mean width of the profile elements RSm is used. With an RSm between 0.4 and 1.3 mm the following measuring conditions result:
λc = 2.5 mm / ln = 12.5 mm / lt = 15 mm / r_{tip} = 5 µm / λs = 8 µm.

Shortened standard evaluation length

If the actual possible traverse length on the workpiece surface is not enough for lt, the number of sampling lengths is reduced accordingly and specified in the drawing.
If the actually available traverse length is less than a sampling length, the total height of profile Pt of the primary profile is evaluated instead of Rt or Rz.

Division of a surface

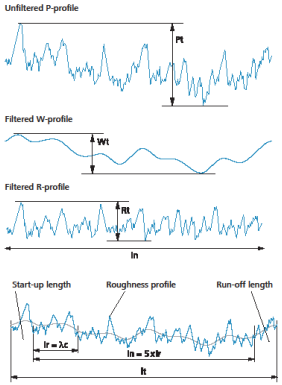

Surface profiles – total height of the profile

The surface profile is measured two-dimensionally using the tracing system.

The unfiltered primary profile (P-profile) is the actual measured surface profile. Filtering it in accordance with ISO 11562/ISO 16610-21 produces the waviness profile (W-profile) and the roughness profile (R-profile). The variable for determining the limit between waviness and roughness is the cut-off λc.

Following ISO 4287, all parameter definitions are valid for both the roughness profile as well as for the primary and waviness profiles. The profile type is identified by the capital letters P, R or W.

The total height Pt, Wt or Rt of the respective profile type is the maximum height between the highest peak and the deepest valley of the evaluation length profile.

Evaluation lengths – cut-off

The traverse length (lt) is the total length of the probe movement during the scanning process. It must be greater than the evaluation length in order to be able to form the roughness profile with the profile filter. With the exception of Rt and Rmr(c), the roughness parameters are defined within an evaluation length ln, which is determined using an average of five sampling lengths lr.

The sampling length lr corresponds to the cut-off λc.

Evaluation of measurement results

According to ISO 4288 the surface measurement should be made where the highest values are to be expected (visual determination).

Maximum value rule

The surface is considered good when the measured values of a parameter do not exceed the fixed maximum value. In this case, the parameter is identified by the suffix „max", e.g. Rz1max.

16 % rule

If the suffix „max" is not specified, the 16 % rule applies, which states that the surface is considered "good" if not more than 16 % of the measured parameter values exceed the fixed maximum value. You will find further information about this rule in the standard ISO 4288:1997.

Special rule VDA

The 16 % rule is not used. VDA 2006 assumes that the dispersion of the parameters is taken into account in the definition of the limit values. The maximum value rule applies generally even without the „max" index in the designation.

The use of the λs filter is prohibited.

* At Rz ≤ 2 µm the stylus tip radius is 2 µm, at Rz > 2 µm it is 5 µm. The distance between two measuring points is ≤ 0.5 µm.

The most important roughness parameters according to ISO 4287, ISO 13565 and EN 10049

Ra – parameter according to ISO 4287

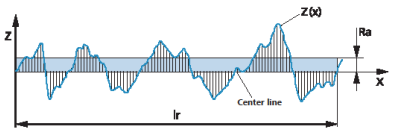

Ra – arithmetical mean deviation of the assessed profile

Ra is the arithmetic mean roughness value from the amounts of all profile values.

Ra does not differentiate between peaks and valleys and has therefore a relatively weak information character.

Rz, Rz1max, Rt – parameters according to ISO 4287

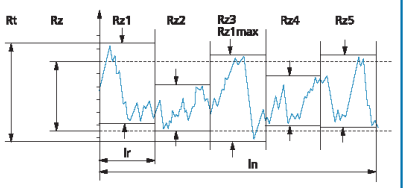

Rz/Rz1max – maximum height of profile: Average value of the five Rz values/greatest Rz value from the five sampling lengths lr.

Rt – total height of profile: Rt is the distance between the highest peak and the deepest valley of the profile of the total evaluation length ln.

RSm – parameter according to ISO 4287

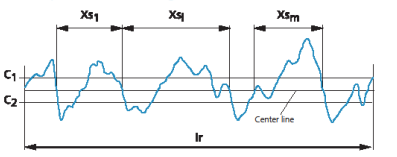

RSm – mean width of the profile elements

RSm is the arithmetic mean value of the width of the roughness profile elements within the sampling length and requires the definition of height discriminations (c1, c2) matching the function of the surface.

RPc – parameter according to EN 10049

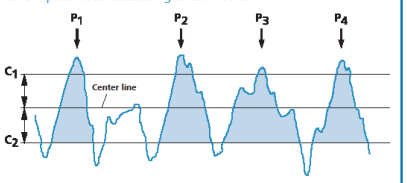

RPc – standardized number of peaks

RPc corresponds to the number of local peaks, which successively exceed an upper section line c1 and a lower section line c2. The number of peaks is related to a length of 10 mm irrespective of the evaluation length selected.

Rmr(c) – parameter according to ISO 4287

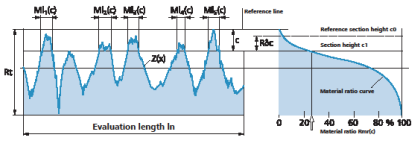

Rmr(c) – material ratio of the profile

Rmr indicates what ratio the totalled length in the material has assumed relative to the evaluation length (in %). The comparison is made in the specified section height c and the total evaluation length ln. The material ratio curve indicates the material ratio as a function of the section height.

Rk, Rpk, Rvk, Mr1, Mr2 – parameters according to ISO 13565

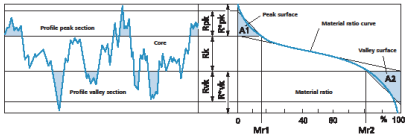

Parameters of the material ratio curve

Rk – core roughness depth
Depth of the roughness core profile.

Rpk – reduced peak height
Mean height of the peaks protruding from the roughness profile.

Rvk – reduced valley depth
The mean depth of the valleys reaching into the material from the core.

Mr1, Mr2 – material ratio
Smallest and greatest material ratio (in %) at the limits of the roughness core area.

Drawing entries according to ISO 1302:2002

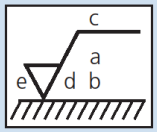

Specifications for requirements

a surface parameter with numeric value in µm
b second requirement (surface parameter in µm)
c production method
d specification of valley direction
e machining allowance in mm

Rz 4	L Rz 2.5	U Ra 4 L Ra 1	Rzmax 4	2/Pt 4	0.008-2.5/Rz1	
Material removing machining; Rz = max. 4 µm	Material removing machining; lower limit value for Rz demanded; Rz = min. 2.5 µm	Material removing machining; upper and lower limit value for Ra demanded; Ra = min. 1 µm and max. 4 µm	Material removing machining; Rz = max. 4 µm; the maximum value rule applies	Material removing machining; P-profile, traverse length = 2 mm; Pt = max. 4 µm	Material removing machining; transmission characteristic does not comply with standard case (cf. table); Rz = max. 1 µm; filter selection λs = 0.008 mm and λc = 2.5 mm	

Drawing entries according to VDA 2007 – dominant waviness

WDc 0	2.5x5/WDt 2.5	0.8x16/Rz 3 0.2-2.5x5/WDc 1.5
Material removing machining; WDcO or WDt 0: no dominant waviness allowed	Material removing machining; in the period range up to 2.5 mm, WDt = max. 2.5 µm applies	Material removing machining; the evaluation length is 12.5 mm and λc = 0.8 mm; Rz = max. 3 µm; in the period range of 0.2 to 2.5 mm, WDc = max. 1.5 µm applies

info.im@jenoptik.com

DAkkS

www.jenoptik.com/metrology

Appendix R Acoustic Sensor Tests

The ice adhesion result obtained represents the complete fracture and detachment of ice from the surface. However, it is unknown of what is happening before complete failure and there is currently no measuring of the early crack initiation and propagation. An acoustic sensor installed inside the test section of IWT can continuously monitor such a parameter as long as the background noises from the air wind can be filtered out. After a crack is initiated, which propagates through the ice by breaking molecular bonds which releases small amounts of energy that spreads as strain waves. The monitoring system is composed of the acoustic emission sensor; an amplifier to amplify the collected signals; a data acquisition system and software that will allow to visualize the data and later on be able to manipulate it. The topics of sound, microphones, sampling and Fast Fourier transform (FFT) will be introduced briefly to understand how the system works.

Sound is a type of energy represented by vibrations that travel through a medium as a waveform. It is defined by the speed at which vibrations are occurring (frequency), by how loud the sound is (intensity), and by its quality (timbre). The sound frequencies that a human ear can detect ranges from 20 to 20 000 Hz. The intensity (dB) is the measure of the amount of energy:

$$dB = 10\log_{10}(\frac{l}{l_0}) \qquad \text{Equation 1.3}$$

Where I is the measure intensity and I_0 represents the sound threshold (10^{-12} W/m^2). A sound signal (Figure 1-8) is characterized by the counts, hits, duration, MARSE energy, rise time and threshold.

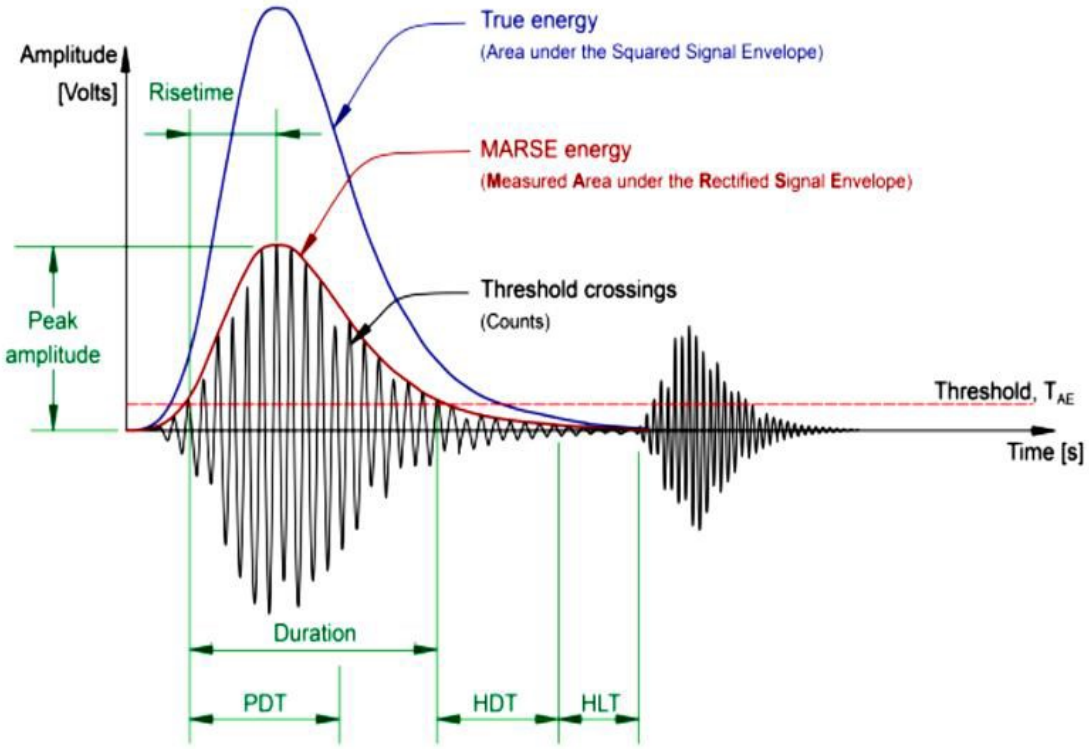

Figure 1-8: Parameters of acoustic emission response.

An acoustic sensor is a measuring device composed of a microphone. A microphone is a type of pressure transducer which converts acoustic energy (sounds waves) into electrical energy (audio signal). The diaphragm is a thin material located inside the microphone and vibrates as a result from the impact of sound. The oscillating movement of the diaphragm induces vibrations to the coil which is attached to it. Due to the permanent magnet that is inside the coil, a magnetic field is produced by the movement of the coil and electric current flows through it. An amplifier is used to amplify the electric current into a stronger signal as a mean to manipulate it.

The process of measuring sound is called sampling since only a finite number of times per time period are recorded, also called discrete signal. Arduino is a commercially available microcontroller and can converts the signal from the connected sensor (which typically varies from 0-5V) to 10-bit signal (values varying from 0-1024) as shown in Figure 1-9. For this project the microcontroller ELEGOO Mega2560 R3 was used with the KY-

038 microphone sound sensor which the wiring diagram is shown in Figure 1-10.

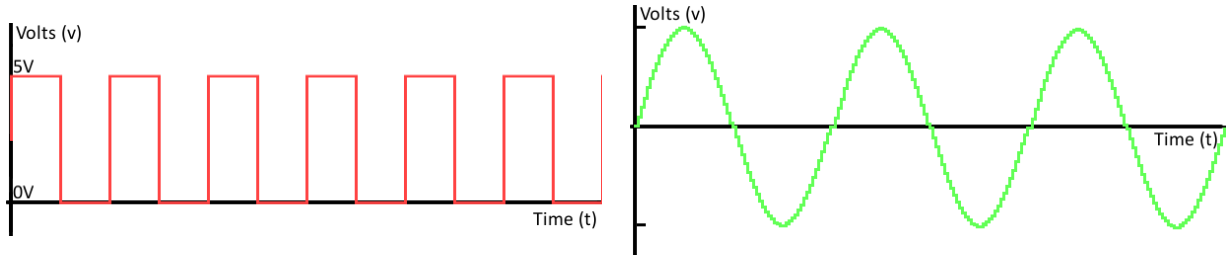

Figure 1-9: Digital signal to analog waveform.

The sound signal is converted from time domain to frequency through the FTT which decomposes the signal into harmonic waves of different frequencies. From the frequency domain waveform, the parameters that can be extracted are peak frequency, dominant frequency band, frequency centroid, and energy (which is defined by the area under the energy density spectrum).

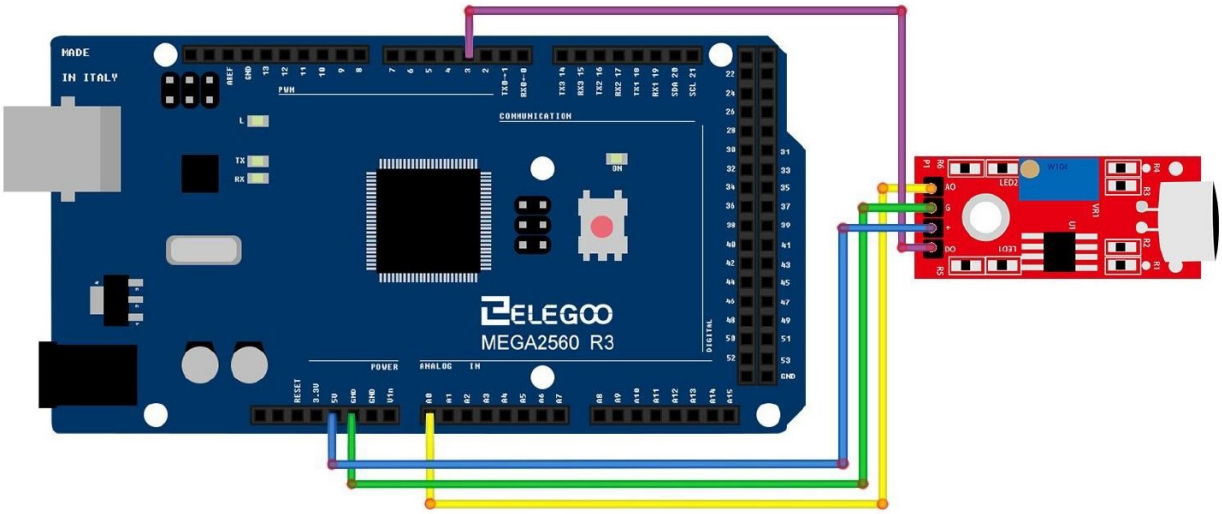

Figure 1-10: Wiring diragram of Elegoo Mega2560 with KY-038 microphone sound sensor.